

SMART CABLE-DRIVEN SOFT MANIPULATION SYSTEM FOR SAFE HUMAN-  
MACHINE-ENVIRONMENT INTERACTIONS

By

Shoue Chen

A DISSERTATION

Submitted to  
Michigan State University  
in partial fulfillment of the requirements  
for the degree of

Packaging – Doctor of Philosophy

2023

## ABSTRACT

Robotics made of soft materials have attracted great attentions in the recent years owing to their superior flexibility and adaptability for completing a wide range of tasks through only concise controls, and most importantly, inherent safety for interactions with humans and the environment. However, the limited power outputs of soft robots (especially manipulators), due to their actuation methods (e.g., via liquid crystal elastomer and shape memory alloy), incompatibility with sensors designed through traditional technologies (e.g., piezoresistive and capacitive mechanism), and the instability arising from their inherent softness, will inevitably hinder robust and reliable real-world applications of soft robotics. For instance, a flexible gripper would be too weak to pick off an apple without enough force exertion or break a blueberry without reliable sensors for feedback controls, or even could not complete a grasp under gravity in certain orientations due to its inherent softness.

Hence, in this dissertation, the actuation mechanisms for soft robotic applications were first investigated mainly in the aspects of actuation easiness, deformation/motion mode, response time, and force exertion. Based on the overall comparison of these driving mechanisms, the cable-driven approach was chosen for the soft robot application for this study due to its wide range of selections in force and speed outputs, and easiness in realizing desired deformations and motions. To develop a high-efficiency and smart soft manipulator for the safe human-machine-environment interactions, great efforts were put into improving the dexterity of soft gripper & arm and integrating compliant sensing units based on triboelectric nanogenerator (TENG) technology with the soft robot structure. To be specific, a soft cable-driven finger actuator was designed with triangular notches to facilitate its inward bending and form a conformal enveloping profile during grasping. And two cables were embedded in the soft robot body, close to its inner and outer surfaces, respectively, to realize both inward and outward bending motions. Nonlinear finite element analysis (FEA) was utilized for the

prediction of its deformation and the corresponding strain & stress distributions at different loading conditions, especially taking the cable-pulling effect into consideration. Then, another smart finger actuator was proposed based on the previous design but incorporated flexible TENG sensing units (tribo-skins on phalanges to detect contact pressures while TENG strips embedded inside the robot body to sense curvature). The assembled smart gripper could subtly perceive the environment and the induced electrical signals could be further utilized for feedback control and machine learning.

Finally, a comprehensive soft robotic manipulator capable of shape morphing and stiffness variation was built. This manipulation system contained a soft omnidirectional arm, a bidirectional gripper, and a human-machine-interface (HMI) through TENG technology in the form of wearable finger patch for programmable remote control. For the soft robot parts, the bellow-shaped arm was actuated by three evenly distributed cables and equipped with stiffness tuning tubes which were filled with low-melting-point alloys (LMPAs). By applying Joule heating, the tubes would become flexible enough for the arm to deform while would get stiff to maintain the shape of the arm after cooling to room temperature. The finger actuator was enhanced through multi-material and flexible hinge designs, so as to perform bidirectional bending in a more stable and safer way. Also, to study an alternative solution for faster stiffness adjustment, a spine-inspired hybrid rod embedded in the central hole of the soft arm was proposed. Finite element analysis was mainly conducted to validate its effects on varying stiffness of the arm. This dissertation research, including designing dexterous soft cable-driven finger actuator and robotic arm, soft and self-powered TENG sensors for tactile and curvature perceptions, stiffness adjustment solutions for extending real-world application, and wearable human-machine interface for programmable remote controls of soft robotics, would help in establishing robust soft manipulation system for safer human-machine-environment interactions.

Copyright by  
SHOUE CHEN  
2023

Dedicated to my parents and my wife.  
Thank you for always believing in me.

## TABLE OF CONTENTS

CHAPTER 1: INTRODUCTION AND LITERATURE REVIEW .....	1
CHAPTER 2: SOFT CABLE-DRIVEN FINGER ACTUATOR.....	33
CHAPTER 3: INTELLIGENT SOFT FINGER ACTUATOR .....	47
CHAPTER 4: INTELLIGENT SOFT MANIPULATOR .....	71
CHAPTER 5: CABLE-DRIVEN STIFFNESS MODULATION .....	94
CHAPTER 6: CONCLUSION AND FUTURE RESEARCH .....	104
BIBLIOGRAPHY.....	108
APPENDIX A: SIMULATION OF SOFT FINGER ACTUATOR WITH SOFA .....	115
APPENDIX B: PROGRAM FOR SOFT MANIPULATOR TELEOPERATION .....	118

## CHAPTER 1: INTRODUCTION AND LITERATURE REVIEW

### 1.1 Background

*The content on actuation methods and mechanisms for soft robotics of this chapter was published in Advanced Materials Technologies 5.2 (2020): 1900837. <https://doi.org/10.1002/admt.201900837>.*

The chapter aimed to investigate the advantages and actuation mechanisms of soft robotics, and the potential sensing and stiffness modulation technologies compatible with them. In addition, the goal of this dissertation would be determined and described in detail.

#### ***1.1.1 Advantages of Soft Robot over Traditional Robot***

Traditional rigid robots are designed based on discrete mechanisms, where functional rigid components are connected to each other via rigid link structures. These links often possess a single degree of freedom (DOF). Based on whether the robot systems have extra DOFs, they are classified into the non-redundant or redundant robot (Figure 1).<sup>[1]</sup> In order to improve the motion flexibilities of rigid robotics for a broader application range, a large deal of links and joints with independent control elements are integrated, such as hyper-redundant manipulators or invertebrate-like robotic topologies. However, control cost is usually high for such method by utilizing complex algorithms. Generally speaking, the traditional stiff robot is capable of performing a precise and faster position operation, but most of them are heavy, bulky, costly, and unsafe for human/environment-machine interactions. As a result, great efforts have been taken to develop soft robotics, which are designed via discrete mechanisms without rigid linkages but rather with elastic materials. Materials for soft robotics could be silicone rubbers, dielectric elastomers, and hydrogels etc., and impart robots with unique features, like light weight, mechanical compliance, infinite DOFs, continuous deformation, low cost, and easy fabrication. Table 1 summarized the features and merits for both rigid and soft robotics.

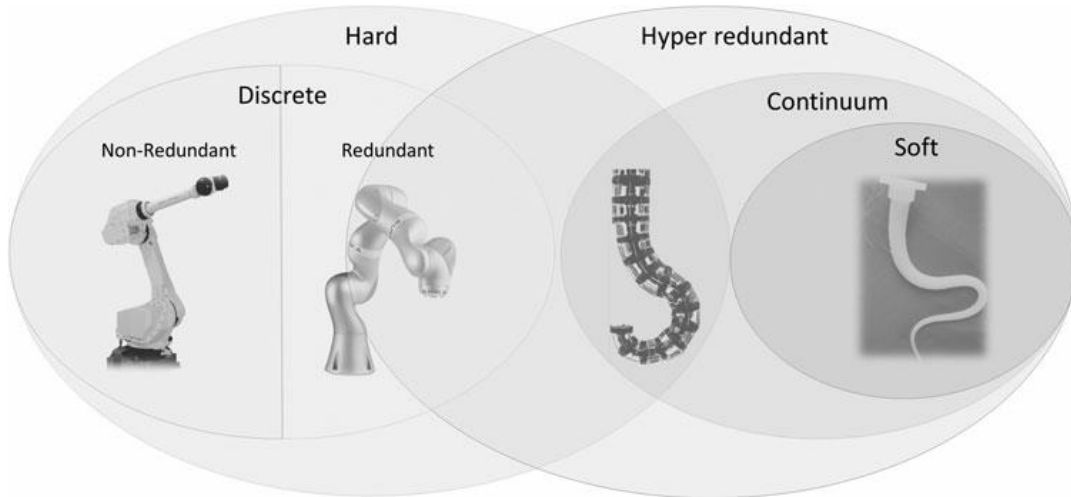


Figure 1. Evolution of traditional rigid discrete robots to continuum soft robots.

Table 1. Comparison of soft and rigid robotic systems.

Soft Robotic Systems	Rigid Robotic Systems
Made of compliant and stretchable materials	Made of hard materials
Inherently safe and adaptive for usages in unknown environments and human-machine-interactions	Dangerous and intolerant with limited adaptability to operate in unknown environments
Infinite DOF for continuous deformation	Discrete topology with a finite DOF
High level of behavioral diversity	Low level of behavioral diversity
Simple and concise control strategy	Complicated control strategy
Low weight and cost	High weight and cost
Low accuracy can be tolerated	High accuracy is required
Low speed and force output	High speed and force output

### 1.1.2 Actuation Methods and Mechanisms for Soft Robotics

Different actuation methods have been explored and adopted to drive soft robotics, mainly including pneumatic pressure actuation, cable-driven actuation, and actuations based on the stimuli responses of smart soft matters, like dielectric elastomer (DE), piezoelectric material (PEM), shape memory alloy (SMA), magnetoactive elastomer (MAE), liquid-crystalline elastomer (LCE), ionic polymer-metal composite (IPMC), and twisted and coiled polymer (TCP). In this part, the working

principle and performance of soft actuators based on different driven mechanisms were discussed in detail. And the primary motion and deformation modes for some representative robotic designs were studied to better understand the actuation technologies mentioned, as well as the advantages and drawbacks of each prototype.

Pneumatic pressure (positive and negative), as one of the most popular driving mechanisms, has been extensively used in soft robot applications. A common feature of soft pneumatic actuators is the existence of designed channel structures enabling the pressure to deform the structural walls, generating desired motions or deformations (e.g., bending, extension, and twisting). One universal prototype named pneumatic artificial muscle (PAM) is formed by inserting an elastomer tube into a fiber sleeve. By doing so, the PAM can only induce linear elongation or shrinkage deformation.<sup>[2]</sup> Due to the large actuation pressure, such design would suffer from easy rupture. Also, the relatively low efficiency in changing the pressure level in the tubing structure would lead to a slow actuation speed. To solve this, a pneumatic network (PN) method has been proposed for highspeed actuation. The easily fabricated and low-cost PN actuator can realize sophisticated motions via simple inputs. In detail, smaller chamber networks will be embedded in a soft body bonded with an unextendible bottom layer to form a PN actuator (Figure 2a).<sup>[3]</sup> There are a variety of parameters to adjust a PN actuator, such as the dimensions and shapes of chamber, soft material properties, and inflation rate. Here, a tetrapod soft robot with 5 PN elastomeric actuators was proposed by Shepherd et al. on the basis of PNs (Figure 2b-c): one PN unit mimicked the spine to lift off the body, and the other four units functioned as legs.<sup>[4]</sup> This robot could crawl forward via anisotropic frictions, by sequentially inflating and then deflating the PNs corresponding to its rear legs, body and front legs. Branyan et al. developed a snake-like robot capable of slithering locomotion (Figure 2d).<sup>[5]</sup> A pair of parallel chamber structures was designed along the tube to achieve the bidirectional bending, and a double-

helical thread wrapping was applied to prevent the twisting of actuator upon inflation (Figure 2e). Similarly, soft snake robot were also developed via friction-based locomotion [6-9] and engineered tribological surface features.[10-13] For example, Rafsanjani et al. proposed a soft crawler comprised of a soft prism-shaped pneumatic actuator coated with kirigami-skins (Figure 2f).[14] The buckling induced by the elongation of the fiber-reinforcement actuator upon would deform the kirigami skin, realizing locomotion based on anisotropic friction for the robot. Efficiency of this kirigami-skinned crawler can be further improved by optimizing the cut geometry and actuation protocol to balance the frictional properties and the stretchability of the skin.[15-18] As for soft gripper designs, Hao et al. designed a soft pneumatic finger capable of bidirectional bending via the wedge-shaped channel structures and adjusting the effective length (Figure 2g).[19] Object with different profiles had its own preferred effective operation length for soft fingers. Under such gripping length, the gripper could work most efficiently and provide the maximum holding force. Here, the variable effective length for the soft finger was realized by selectively placing nylon tendon that acts to mechanically alter the stiffness of the finger area for inflation & deflation. Also, the bidirectional bending of the finger could expand the grasping scope for the gripper. To be specific, the soft fingers are deflated to bend outwards at first, enlarging the grasping scope (the ability to work with larger objects) and achieving better enveloping profile for the subsequent contacts.

Negative pneumatic pressure (i.e., vacuum) instead of positive one is also utilized to drive soft robots. For instance, Robertson et al. proposed a vacuum-based soft actuator named as V-SPA, and combined into a robot structure with high DOFs (Figure 2h).[20] The V-SPA unit was consisted of three evenly distributed pneumatic channels in a cylindrical configuration, and a central vacuum supply was linked to each channel. A polyurethane foam core and rigid paper dividers were utilized to prevent the potential buckling of the structure, and a rubber layer was uniformly coated onto the

outer surface of the actuator unit to prevent air leakage (Figure 2i). The angular deformation of the soft robot was realized through the shrinks of different pneumatic chambers.

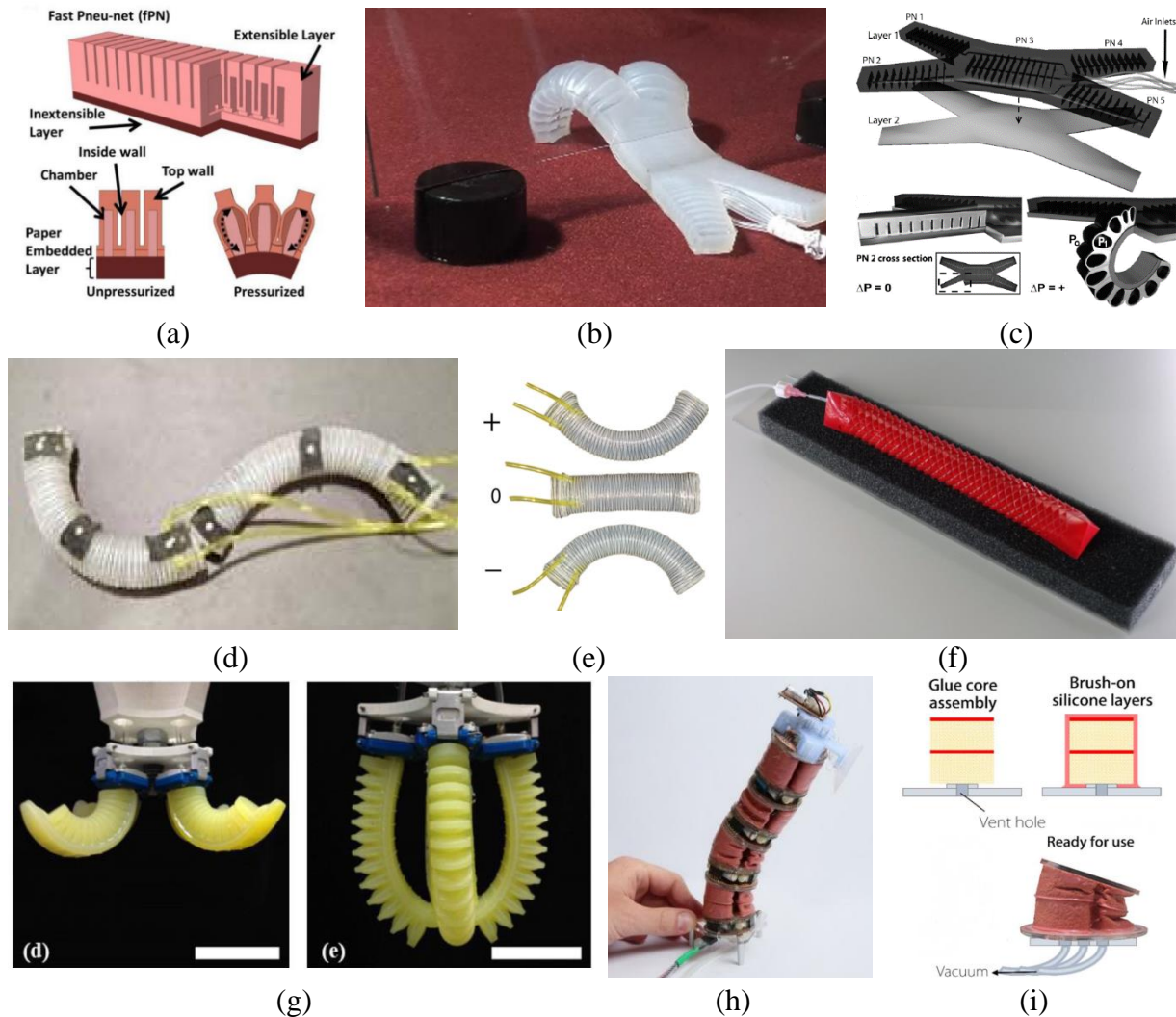


Figure 2. Soft robots via pneumatic actuation. (a) Schematic of a normal PN actuator design. (b) A crawling robot with (c) the cross-section views of its PN actuator under various pressures. (d) A snake-like robot with (e) its bidirectionally bendable actuator. (f) A prism-shaped pneumatic actuator coated with kirigami-skin. (g) A bidirectional soft gripper with wedge-shaped channels. (h) A multi-segmental vacuum robot and (i) the structure of its pneumatic actuator.

Another widely employed actuation mechanism for soft robots is the cable-driven actuation. The deformation and locomotion of the soft robots are realized by retracting or releasing the cables which are embedded throughout the soft bodies and anchored at some specific points (end fixators), as illustrated in Figure 3a.<sup>[21]</sup> The arrangement and orientation of cable units as well as profiles of

the robotic body structures (both external and internal ones) are the major factors for designing the soft robots via cable-driven approach as those will determine trajectory of force transmission from the end fixators. Although there are challenges to guide and deploy cables, and place motor, pulley, and cable fixators, in general, cable-driven approach exhibits features of light weight, fast response, and large force output, which is determined by the motor parameters, and cables have high tensile strength but zero bending stiffness. Moreover, the actuation force can be delivered along the whole soft body from a target point (end fixator) to minimize the inertia.

Mutlu et al. focused on the structure design of flexure hinges for fabricating soft monolithic prosthetic fingers actuated via cables and mimicking human finger very well (Figure 3b).<sup>[22]</sup> After systematically studying the input-output performance of various flexure hinges, the nonsymmetric elliptical-type hinge structure was selected and optimized to resemble joints of human index finger, as it could induce the highest bending displacement compared with other hinge structures. The soft 3D-printed finger was actuated by a cable passing through the designated hinge channels to induce desired grasping motions (Figure 3c). Ito et al. proposed a soft octopus-like robot (TAOYAKA-S II). This robot was able to grasp different objects with unknown profiles and could climb different columnar objects by inching its trunk (Figure 3d).<sup>[23]</sup> The trunk and leg structures were described in Figure 3e. By dragging the embedded cable in a special manner, the trunk composed of bilateral notches structure could realize a large-scale inching motion. The original shape of the soft leg was designed into a spiral profile in order to make the bending motion of soft segments occur gradually from the root to the tip, mimicking the behaviors of octopus. In addition, a cable-driven quadruped robot casted from flexible foam material was built by Bern et al., with optimized motion trajectory (Figure 3f).<sup>[24]</sup> Each of the four legs of the robot (Puppy) was controlled by two motors with cables deployed through 3D-printed eyelets attached onto the soft body. Heavy weight of motor assembly

made the Puppy unstable and top-heavy, requiring complicated control strategy to make it capable of walking straightly on the flat surface (figure 3g). On the other hand, the crawling robot was able to turn with one of its legs as a pivot.

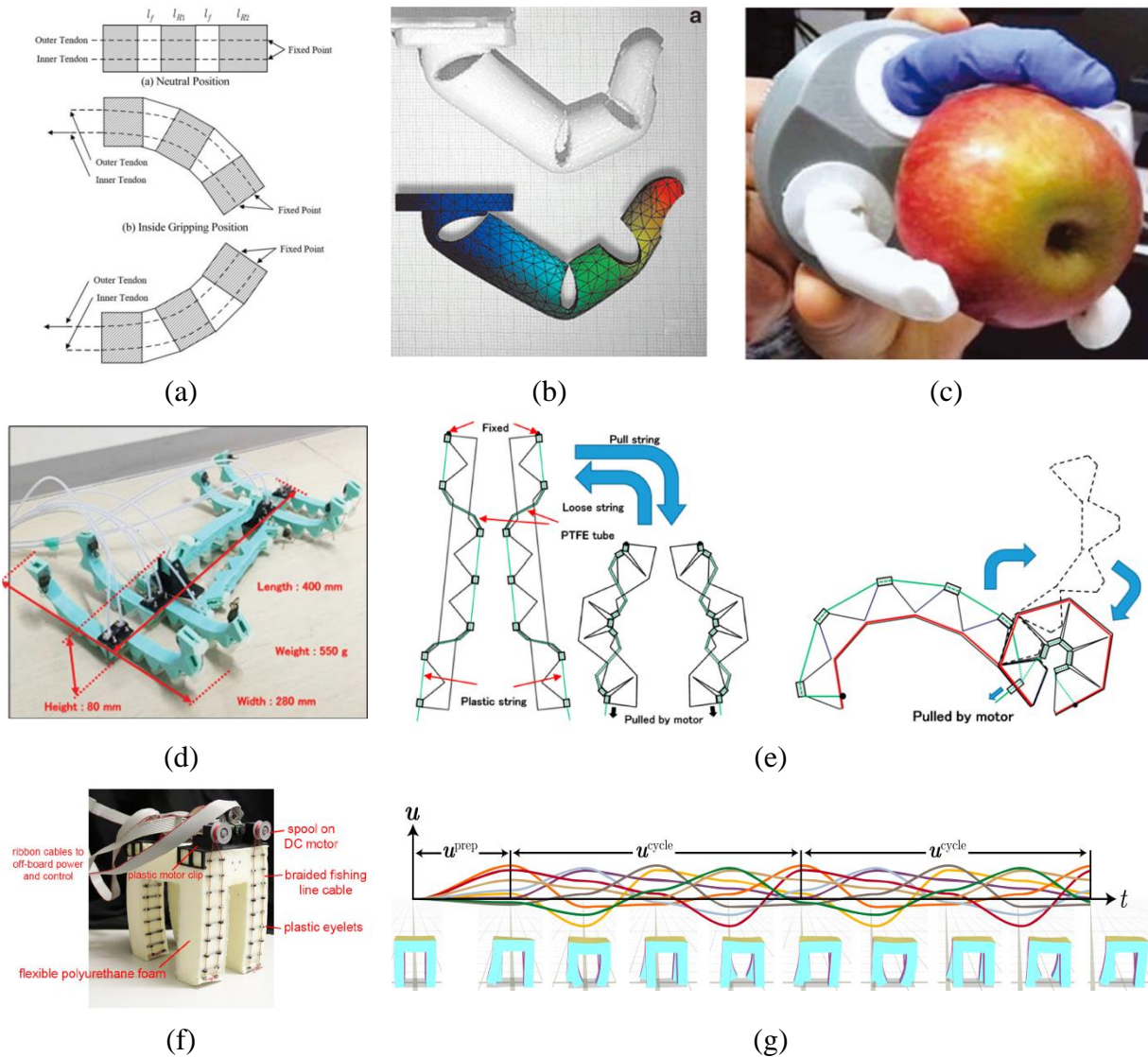


Figure 3. Soft robots actuated by cables. (a) Principle of the cable-driven mechanism. (b) Flexure hinge designs for a finger actuator and (c) the assembled gripper. (d) An octopus-like robot with (e) its cable-driven structures for flexible leg & trunk. (f) A quadruped robot made of soft foam, and (g) the walking gait through cyclic control trajectory.

Dielectric elastomers (DEs) have been widely adopted in fabricating soft actuators due to their large actuation strain, high compliance, and high energy density. DEs are able to respond to

electrical stimuli to induce large deformations and/or shape changes. A typical dielectric elastomer actuator (DEA) is made of a thin DE film with soft electrodes coated on both surfaces, forming a parallel plate capacitor. When a voltage is applied to electrodes, opposite charges will be generated on both sides of the film, inducing a Maxwell stress to compress the film and let it shrink along its thickness direction while expand in-plane, as described in Figure 4a.<sup>[25]</sup> Based on such mechanism, different types of DEAs have been proposed, including stack, bimorph and unimorph, diaphragms, bulged membrane, and spring-roll designs.<sup>[26]</sup> An entirely soft crawling robot enabled by DEA was reported by Henke et al. (Figure 4b).<sup>[27]</sup> In brief, the pre-stretched DE film was bonded to a silicon structure with an anisotropic bending stiffness to retain the strain of the DE film (Figure 4c). Then, the force arising from the pre-strain bent the whole-body along its softer axis. Under a high voltage (~ 3 kV), its curvature would vary, leading to the crawling motion of the soft robot through friction.

For improved the environmental adaptabilities, novel structures without rigid part, like gear, linkage and wheel, have been developed for soft rolling robots. As described in Figure 4d, a rolling soft robot (RSR) was developed by connecting the multi-segmental dielectric elastomer minimum energy structures (DEMES) to form a ring-like configuration.<sup>[28]</sup> This rolling robot was in a stable shape when the pre-strain in DEMES was released, where the resilience of the frame was balanced by the contraction force arising from DE films. As a high voltage was applied to either active area, the induced Maxwell stress bent the DEMES correspondingly and altered its configuration (Figure 4e), resulting in a rotational momentum due to the deviations of the gravity center of this robot.<sup>[29-31]</sup> When the DEs in the opposite direction were actuated by an applied voltage of 3.2 kV, the RSR could immediately transfer its profile from a circle into an ellipse within 50 ms. This high response frequency and the lightweight facture (0.88 g) enabled it to achieve a high speed-mass ratio of ~41 mm/(s.g). Li et al. further proposed a variant based on an annular body made by multisegmented

DEMES and six electro-adhesive actuator (EAA) feet (Figure 4f).<sup>[32]</sup> Locomotion of this creeping robot (OCSR) was realized through changing the shape of the annular DEA via activating different DE elements on the circular body, in combination with supporting adhesion provided by EAA feet in the creeping process (Figure 4g). One significant advantage of the design was the ease of control in multi-directional movement.<sup>[33, 34]</sup> DEMES could also be assembled into a gripper configuration. In the research of Araromi et al., they proposed a DEMES-based soft gripper targeting active debris removal for spacecraft applications (Figure 4h).<sup>[35]</sup> Their fabricated DE-based gripper possessed a really low weight of 0.65 g, and could induce a change in tip angle of ~60 degrees with a maximum grasping force of 2.2 mN.

For the purpose of improving the motion flexibility, antagonistic multi-DOF actuators have been investigated and exhibit a better performance than folded DEAs due to its simpler shape and higher DOFs, yet still suffer from large weight, bulky size, sophisticated assembling process, and relatively low speed. Nguyen et al. improved the previous robotic designs, and developed the new version, S-Hex II, with a smaller size but more than 12 times the walking speed (52 mm/s) (Figure 4i).<sup>[36]</sup> The improvement was attributed to the enhancement of a 5-DOF soft actuator (Figure 4j),<sup>[37, 38]</sup> in which the electrode coated on each DE film was divided into four separate regions, increasing the structural DOF. Different from the fabrication steps for S-Hex I, the initial synthetic elastomer utilized was modified to improve its tearing strength for allowing a large pre-strain on the DE film with a higher electromechanical strain. It was demonstrated that the improved 5-DOF DE actuator (~4 g) could generate a higher stroke (2.58 mm), larger rotation (16.4°) and higher force (0.124 N) output and torque (1.08 N.mm).

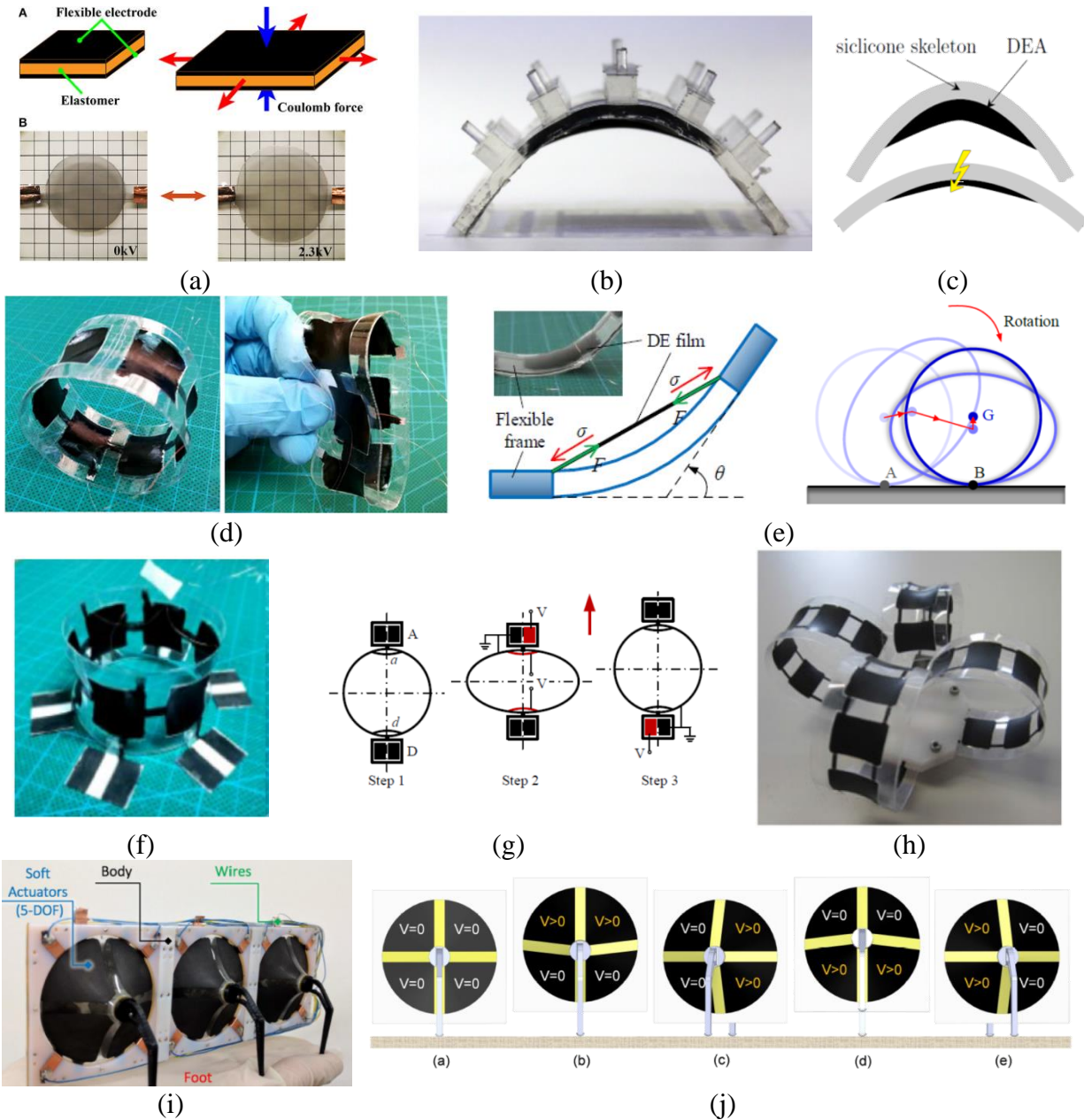


Figure 4. Soft robots actuated through dielectric elastomers. (a) Basic working principle of DEA. (b) An entirely soft robot, and (c) its crawling motion realized by a pre-stretched DE film. (d) A rolling robot (RSR) based on multi-segment DEMES. (e) Force diagram of the DEMES and the rolling process. (f) An omnidirectional creeping soft robot (OSCR) consisting of DEA body and six EAA feet, and (g) its locomotion mechanism. (h) A light-weight DEMES-based soft gripper. (i) A hexapod robot with (j) its leg postures during a walking cycle.

Piezoelectric materials (PEMs) are able to function as actuators when converting electricity into mechanical deformation via converse piezoelectric effect. Polyvinylidene fluoride (PVDF) is

one of the most promising piezoelectric materials for soft robotic applications, as it has superiority in thickness, weight, and flexibility, yet needs high driving voltage. For instance, a catapult origami with multilayered PVDF film could generate a  $19^\circ$  angular displacement under a voltage of 3 kV,<sup>[39]</sup> and the space antennas can be controlled in the shape by applying a voltage of 0.8 kV.<sup>[40]</sup> Recently, Wu et al. designed a self-curved unimorph actuator by coating a thin layer of PVDF ( $d_{31}=-27\text{pC/N}$ ) film onto a pre-stretched polyimide (PI) tape with a thickness ratio of PVDF:PI=2.5 (Figure 5a). Compared with the flat unimorph (i), this curved structure (ii) could induce a larger deformation by a much lower driving voltage (200 V, peak to peak), and could alter its curvature based on the voltage applied (Figure 5b).<sup>[41]</sup> The pre-curved unimorph soft robot could crawl like an inchworm. When a voltage (+100 V) was applied, the structure shrunk to its minimum curvature, having legs attached to the surface and the tail sliding forward (displacement of  $a_1$ ). When the power decreased to zero, the tail served as an anchor while the legs moved forward. When the voltage was reversed (-100 V), the soft body elongated to its smallest curvature and the tail attached to the surface, after which the leg moved forward (displacement of  $a_2$ ). As the voltage was off again, the robot returned to its initial shape with the total displacement of  $a_1+a_2$ . The as-fabricated inchworm robot achieved a speed of 0.3 mm/s on the paper surface, or 1.9 mm/s on a ratchet surface.

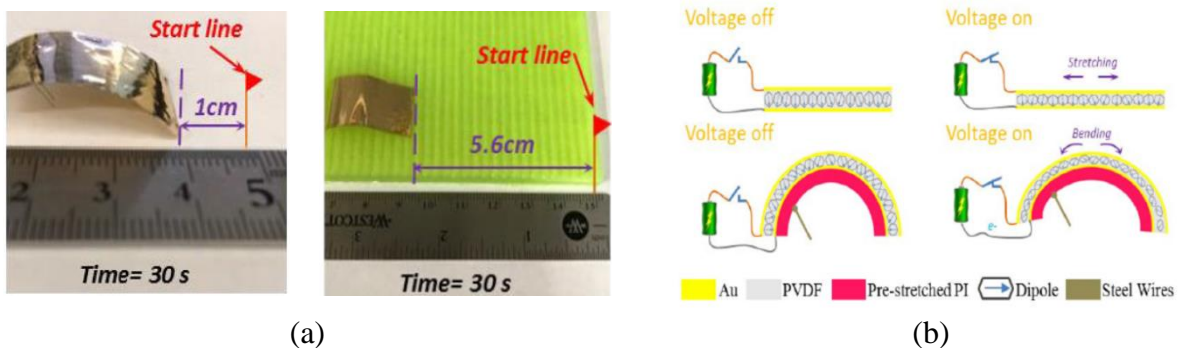


Figure 5. Soft robot actuated by piezoelectric material. (a) The compliant robot based on PVDF. (b) Crawling motion realized by the pre-curved robotic structure.

Shape memory alloy (SMA) has been widely explored and studied to fabricate soft robotics

due to its high work density, large recovery stress & strain, silent operation, low actuation voltage, corrosion resistance, and biocompatibility. A deformed SMA structure can restore its initial shape when heated to its transition temperature due to the reversible diffusion-less conversion between states of starting austenite and post-deformation martensite phases (Figure 6a).<sup>[42]</sup> SMA actuators are able to provide both actuation and structural functionalities but typically require high current, exhibit limited bandwidth, and have wide time windows to be cooled down. Umedachi et al. built a caterpillar-like robot by using multi-material 3D printing (Figure 6b).<sup>[43]</sup> Two coiled SMAs were tactfully embedded in robot's body and could be driven electrically (Figure 6c). By arranging the two SMA actuators side-by-side and in an overlapping manner, a retrograde wave could be induced by contracting one of the SMA coils and the elastomeric body would transfer the induced force to the other part of the robot body. The two SMA coils in such arrangement were able to stir up waves with various frequencies, wavelengths, phases, and amplitudes, inducing multiple locomotion gaits based on interfacing of waves through the robot body. Also, the variable frictional legs allowed it to produce enough frictional forces through deforming the body to get the appropriate locomotion. A similar robot (GoQBot) was made of two SMA springs embedded into the elastomeric material, resembling a caterpillar and mimicking its movement (ballistic rolling and crawling).<sup>[44]</sup> Possessing a domed cross-section, solid material on dorsa, and small wedge-shaped leg, it was able to perform ventralward bending. In addition, the laterally elongated hammer head and the softer layer of sticky rubber enhanced its surface contact. Inspired by starfishes, a multi-rayed silicone-based robot was built with SMAs (Figure 6d).<sup>[45]</sup> When the SMA springs were heated, the induced forward friction shifted the gravity center of robot to form a stable shape, and the opposite group of rays deformed to store elastic potential energy and further push the robot ahead when releasing the energy (Figure 6e). Through repeated deformation of the rays induced by SMA actuator, continuous motion could

be achieved even in different terrain conditions. Kim et al. designed a turtle-like robot with SMA-based smart soft composite (SSC) (Figure 6f).<sup>[46]</sup> The SSC structure consisted of a series of active parts (SMA wires) generating actuation forces, with the passive units (stiffen anisotropic materials) controlling angles for twisting and bending, and a polymeric matrix for combination and stiffness adjustment. Based on the classic laminate theory and chain algorithm,<sup>[46]</sup> the forces and momenta generated by SSC structures were solved under different arrangements (angle-ply or cross-ply) to generate targeted locomotion. For instance, a positive ply-angles scaffold was utilized for posterior positive and interior negative twisting angles of the turtle flippers during upstroke and downstroke, respectively (Figure 6g).

Remarkably, Cho et al. fabricated an omega-shaped inchworm-inspired crawling soft robot (Omegabot) adopting SMA coil-spring actuators (Figure 6h).<sup>[47]</sup> This soft Omegabot was made of a single piece of a composite, including two four-bar linkages functioning as bending components, one spherical six-bar linkage as a steering controller, and two pads made of soft materials providing anisotropic friction. A large pitch-angle range SMA coil spring was designed to have a large spring index (11) and a pitch angle ( $29^\circ$ ) as well as an enhanced cooling performance (0.3 s) due to more surrounding air compared to the traditional SMA springs. To crawl, the upper/lower SMA springs were activated alternately. The upper actuator extended the body, while the lower actuator dragged it, leading to an omega robotic shape. For steering, the spherical six-bar linkage could induce both pitch-axis and yaw-axis motions via actuating the left and right SMA alternatively. However, this robot could not move at a high frequency as the actuation frequency of the SMA spring was limited by the inherent slow cooling down process.

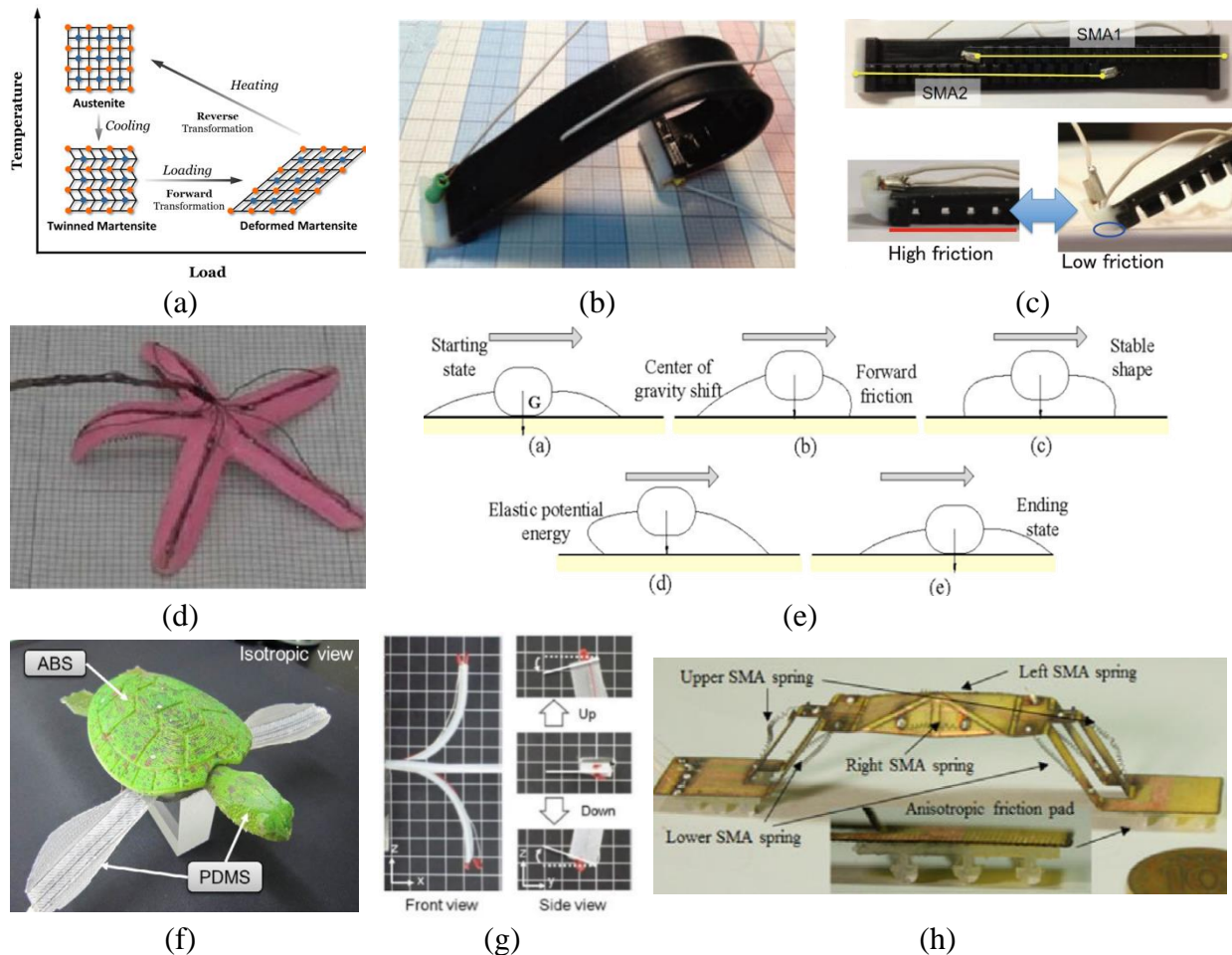


Figure 6. Soft robots actuated by shape memory alloy. (a) Mechanism for SMA. (b) A multi-material crawling robot and (c) its SMA arrangement and anisotropic friction design for efficient locomotion. (d) A starfish robot, and (e) its locomotion mode. (f) A turtle-like robot realized by SMA-based actuator, and (g) its swimming postures. (h) Omegabot prototype with SMA springs and anisotropic friction pads.

Magnetoactive elastomers (MAEs) are fabricated by dispersing magnetic fillers into a soft elastomer matrix. In the presence of magnetic fields, soft MAEs are capable of inducing elongation, contraction, bending, or other types of complex deformations. The magnetization profile, actuating signal and overall shape of filler materials, are the major factors affecting the deformation patterns of such materials.<sup>[48-50]</sup> MAEs are ideal materials for soft robots targeting applications in enclosed and confined spaces (e.g., microscale biological robots).<sup>[51]</sup> Figure 7a shows a soft magnetic active robot capable of realizing desired time-varying shape change and multimodal locomotion exposure

to magnetic field.<sup>[52]</sup> Magnetic microparticles (neodymium-iron-boron, NdFeB) were dispersed in a silicon substrate, and high remnant magnetization and large coercivity of NdFeB microparticles ensured the generation of effective magnetic actuation and the stability of magnetization profile during actuation. A uniform time-varying magnetic field could generate various locomotion modes (e.g., climbing, swimming, rolling, walking, and jumping), and control the robot morphology and steer its locomotion in a specific direction. Moreover, the as-fabricated robot could switch between locomotive modes, transit reversibly between liquid and solid terrains, and execute pick-and-place and cargo-release tasks.<sup>[52]</sup>

Remarkably, Lu et al. built a soft multi-legged millirobot via a modified magnetic particle-assisted molding method (Figure 7b).<sup>[53, 54]</sup> Such tapered feet structure was formed with a mixture comprised of polydimethylsiloxane (PDMS), hexane, and magnetic particles under magnetic fields. The magnetic field with distinct trajectory was applied for combined discontinuous and continuous locomotion. Under a controlled magnetic field, the pulling force and magnetic torque were induced to deform the tapered feet align with the direction of magnetic flux, then to drive the robot crawling forward.<sup>[55, 56]</sup> Also, the storing and releasing of energy with flexible legs during motion decreased the total energy consumption while increased the stability and obstacle-traversal ability of the soft robot. The millirobot made of MAEs showed superior functionalities like shape-changing, efficient locomotion, and load carrying. In another study, Zhao and coworkers proposed the untethered fast-transforming soft robotics through direct 3D printing with programmed ferromagnetic domains.<sup>[57]</sup> The ink was made by mixing magnetizable microparticles, silicon nanoparticles, and silicon rubber. Upon printing, a magnetic field was applied by an electromagnetic coil to dispensing nozzle, which reoriented ferromagnetic particles to impart patterned magnetic polarities to the extruded ink flows (Figure 7c). The capabilities of building complex shapes and programmed ferromagnetic domains

provided a variety of functions, like fast deformation, stopping, and capturing a fast-moving object, as well as the ability to grasp and to release objects with arbitrary shapes, demonstrating promising potentials in the applications of flexible electronics, biomedical devices, and soft robotics (Figure 7d).

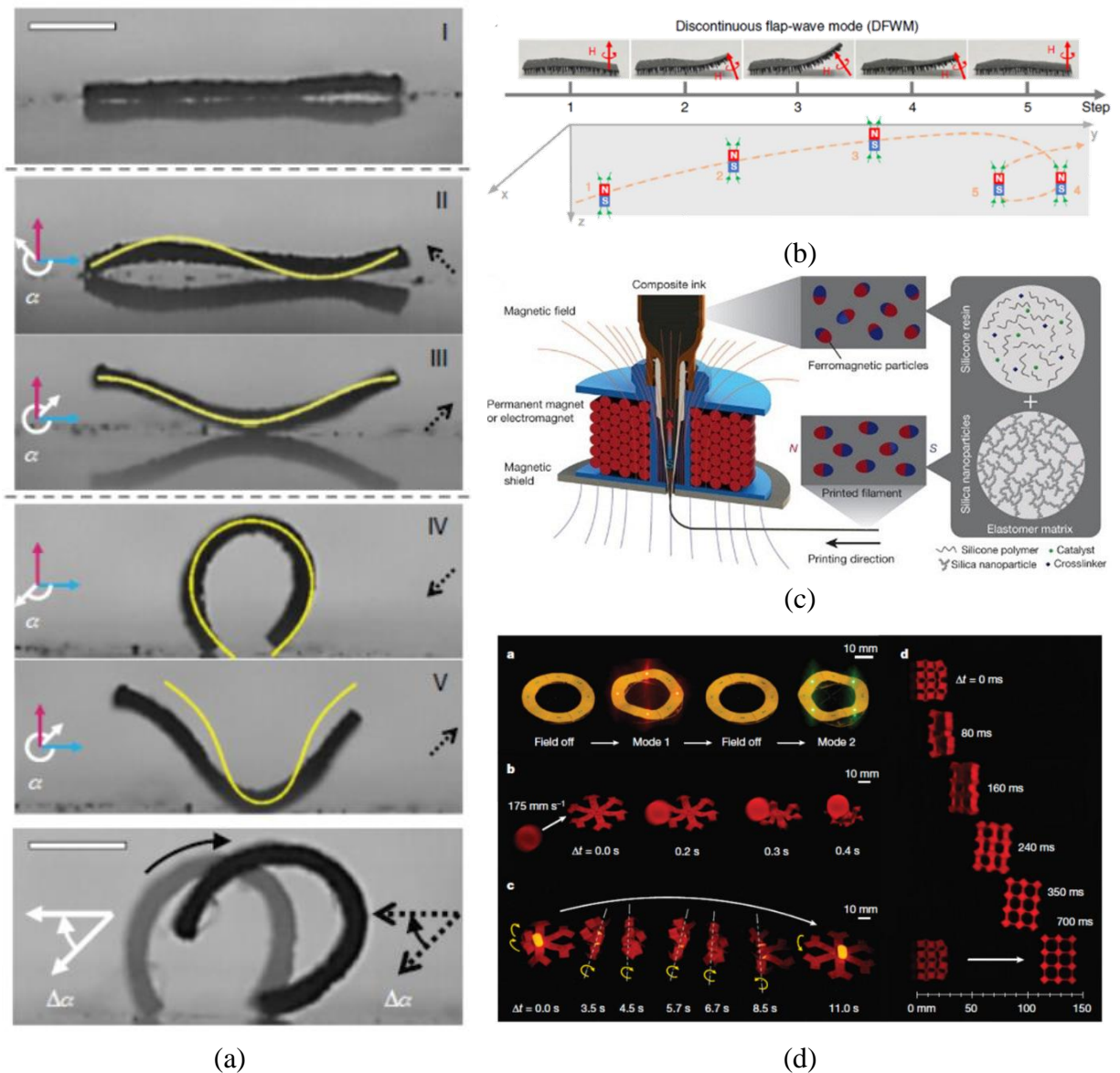


Figure 7. Soft robots based on magnetoactive elastomer. (a) A tiny robot capable of multimodal locomotion. (b) A multilegged robot with different locomotion modes. (c) Schematic of material composition and printing stage for an untethered fast-transforming robot and (d) its diversified functionalities.

Soft actuators made of liquid crystal elastomers (LCEs) are popular due to their outstanding

flexibility and self-organization functionality. Via incorporating anisotropic mesogens (i.e., liquid crystal molecules) into polymer chains, the LCE actuator can be fabricated. Under a stimulus, like ultraviolet (UV), irradiation, or heat, the crosslinked liquid crystalline polymer (CLCP) transforms between isotropic and liquid-crystal phases.<sup>[58]</sup> In general, LCEs can only exhibit reversible shape changes after receiving mechanical programming. Such limitation was countered by the two-stage crosslinking method proposed by Kupfer and Finkelmann,<sup>[59]</sup> where a flexible network was formed during the 1st stage crosslinking, and the mechanical stretching could be applied to align mesogens. And the macroscopic mesogen alignment was fixed during the 2nd stage (i.e., curing). By changing temperature above/below its nematic to isotropic transition point, LCE could alter between its non-aligned (isotropic) and aligned (anisotropic) phases, resulting in a large and reversible deformation. The mechanical behavior of the LCE actuator was mainly determined by factors like the crosslink density, the liquid crystal molecule, and the connectivity of liquid crystal molecules to the polymer chains.

Yamada et al. prepared a laminated film comprised of a CLCP layer containing azobenzene moieties which help in producing large deformation, and a low-density polyethylene (PE) sheet to generate different locomotion modes via photoirradiation (Figure 8a).<sup>[60]</sup> In the smectic phase, the CLCP film exhibited a higher order of azobenzene mesogens along rubbing direction of polyimide layer and could induce a large force. In addition, the film was able to work at room temperature as with a similar glass-transition temperature. Owing to the mismatched thermal expansion properties of the laminated layers, the CLCP membrane would curve. The initially curved laminated film was flat when exposed to the UV light and restored its original curved shape when triggered by a visible light irradiation, functioning as a “hinge joint” for locomotion. Roach et al. presented a novel main-chain LCE ink which allowed LCE to be printed at room temperature (transition point  $\sim 42^{\circ}\text{C}$ ) with

a maximum actuation temperature of 75°C, and they also designed a 3D printed soft robotic gripper consisting of four LCE hinges (Figure 8b). When an electric current of 1.5 A was applied, an object could be picked up by the gripping force induced by LCE hinges.<sup>[61]</sup>

Rogóz et al. designed a caterpillar robot on the basis of a light sensitive stripe made of LCE (Figure 8c).<sup>[62]</sup> A monomer mixture was laminated by two polyimide coated plates rubbed with a pattern of strips. This pattern was preserved by curing with UV irradiation, and the molecules were aligned along the rubbing direction in the rubbed regions, but randomly oriented in the non-rubbed regions. So, the film was flat when the temperature was lower than the phase transition temperature ( $T_{pt}$ ), while changing into a curved shape when heated above  $T_{pt}$ . By scanning a laser beam from tail to head, the robot was able to crawl forward (Figure 8e). The as-fabricated robot could squeeze through a narrow slit, walk up on a slope, or even push objects under light excitation with a moving speed of 0.1~0.5 mm s<sup>-1</sup>. More recently, Wang et al. used a thermally responsive artificial muscle made of carbon-black-doped LCE (CB-LCE) nanocomposite to drive an inchworm robot (Figure 8f).<sup>[63]</sup> In the design, a bimorph structure was built by sandwiching a heater between CB-LCE layer and Kapton film to mimic the “wavy” configuration of an inchworm. A flexion could be triggered in the film when it was heated. As shown in Figure 8g, the robot with two programmable bimorphs could move forward by alternatively turning the two heaters on and off with the front leg acting as a grip leading to an anchor-pulling.

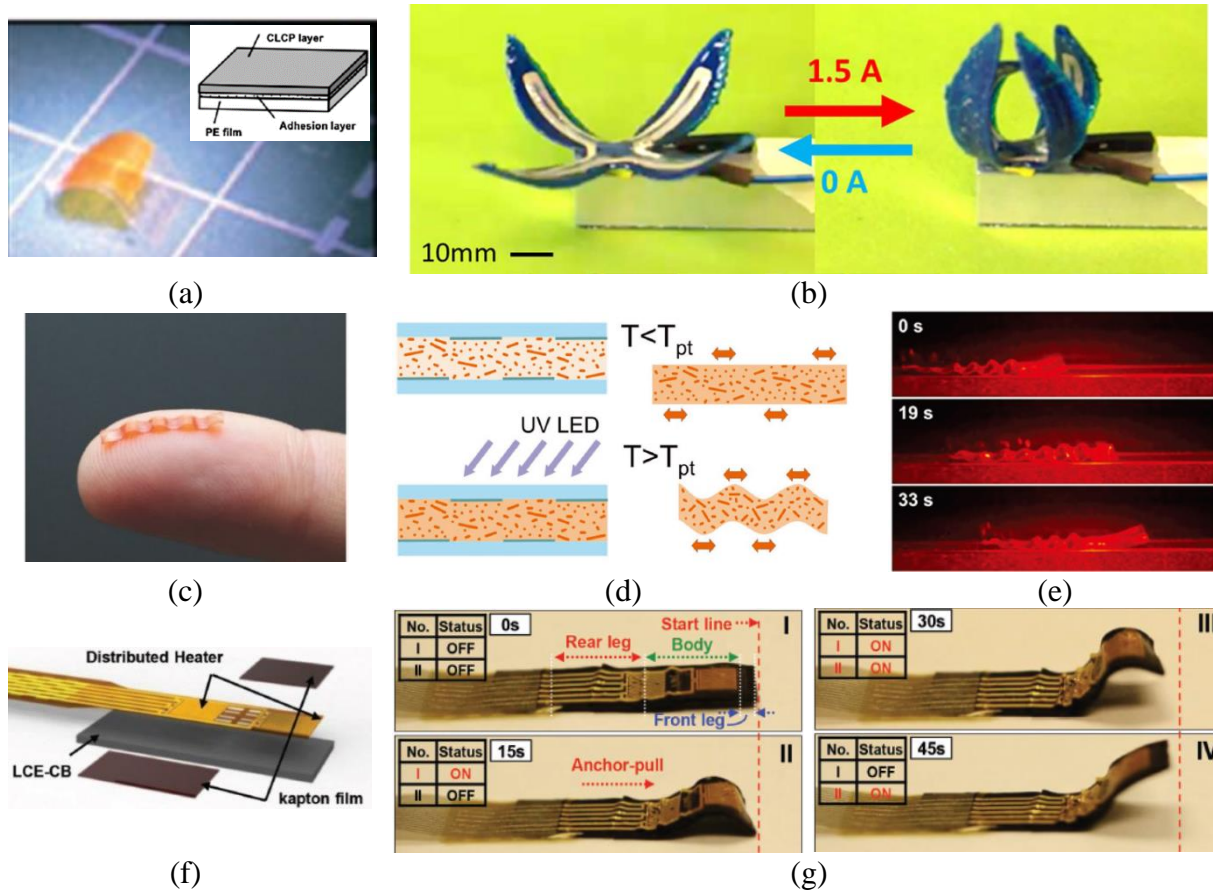


Figure 8. Soft robots based on liquid crystal elastomer. (a) A soft crawling robot actuated via a laminated CLCP film. (b) A 3D printed gripper with 4 LCE hinges. (c) A light-driven caterpillar robot, (d) its fabrication with patterned molecular orientation, and (e) its motion mechanism. (f) Structure of the crawling inchworm robot with CB-LCE, and (g) its sequential locomotion.

The compliant actuator called ionic polymer-metal composite (IPMC) is usually comprised of an ion-exchange membrane with metal electrodes physically or chemically coated on its surface. Actuators based on IPMCs have features such as low driving voltage, high flexibility, lightweight, silent operation, and aquatic adaptability. By applying voltage to a hydrated IPMC unit, the charge redistribution will affect its hydrophilic regions, inducing a swift bending motion toward the anode side.<sup>[64]</sup> A modular IPMC robot mimicking caterpillar was developed by Carrico et al. by using 3D printing technology for IPMCs (Figure 9a).<sup>[65]</sup> The robot was assembled by modular ring-like legs (acting as grippers) and body segments (acting as extensors). The IPMC actuator in elliptical shape with four electrodes on both interior and exterior surfaces functioned as the body unit for the robot.

The body unit would expand when a voltage was applied to the anode located at its exterior surface, while reversing the voltage polarity would contract the body unit (Figure 9b). Through alternative expansion and contraction of the body units along with gripping and opening of robot legs, a wave-like locomotion of the robot could be achieved. In addition, a novel composition for fabrication of high-performance IPMC actuator was proposed.<sup>[66]</sup> To be specific, the IPMC membrane was based on SGO (sulfonated graphene oxide) and PVDF, coated with polypyrrole (PPy) and platinum metal (Pt), exhibiting high ion exchange capacity, proton conductivity and water uptake, along with high current density and larger tensile stiffness. Deformation of an as-fabricated IPMC membrane under different DC voltages (0~5 V) was shown in Figure 9c. A maximum tip deflection of 14 mm along with a loading capacity of 0.41 g could be attained under a voltage of 5 V. A manipulator developed by the novel IPMC actuators was illustrated in Figure 9d.

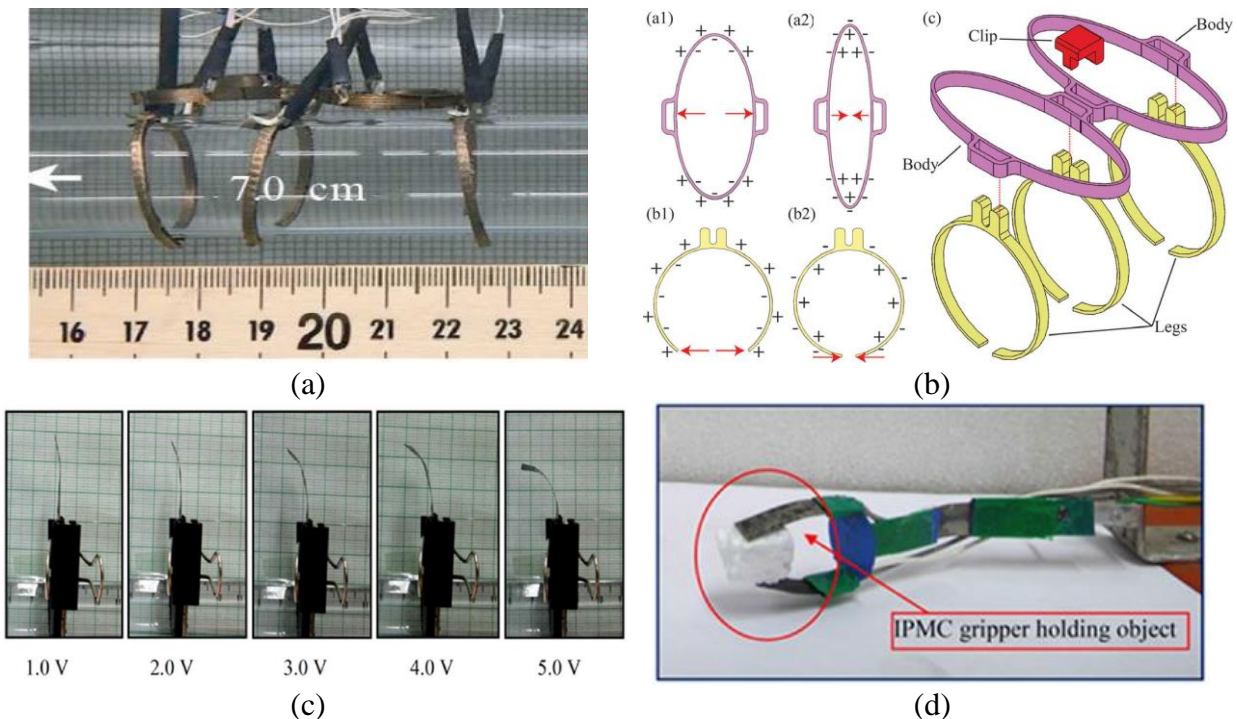


Figure 9. Soft robots through ionic polymer-metal composite. (a) A 3D-printed IPMC robot with ring-like body and legs and (b) their deformation mechanisms. (c) Deformation of the improved IPMC actuator under different voltages, and (d) a soft manipulator developed by the new IPMC actuator.

Twisted and coiled polymer (TCP), given the name by its fabrication process, was reported recently. This kind of smart actuator is formed by twisting nylon threads into a coil configuration, and is thermally actuated (contract on heating) to generate evident strains and stresses (Figure 10a).<sup>[67]</sup> Due to its features, like excellent flexibility, low material cost, lightweight, high energy-density, and small hysteresis, such actuator is promising for developing soft robots. In addition, it possesses two major advantages over traditional ones. First, the TCP actuator made of conductive nylon fiber can be electrically activated by Joule/resistive heating, one of the most efficient ways for actuation. Also, it can be fabricated to complete either contraction or extension and easily embedded into soft matters for efficiently distributing actuations. Second, TCP actuator can detect its own deformation through the variation of electrical resistance, allowing feedback control through current sensors.<sup>[68]</sup> Pawlowski, et al. embedded TCPs into soft cylindrical finger to successfully grasp low-weight (2 g) objects when heating TCPs to 120°C. Applying heating would let the TCP extend due to internal untwisting torques, arising from radial thermal expansion (Figure 10b).<sup>[69]</sup> A supercoiled polymer artificial muscle (SCPAM) was developed by Yang et al. for a soft crawling robot (Figure 10c).<sup>[70]</sup> Silicone rubber was adopted to form the robotic body, while resin was selected to form the slippery part around its edge with a smaller friction coefficient, contributing to a variable-friction leg. The contraction of SCPAM upon heating would bend the robot body over the threshold angle and lead to contact of its slippery part with the floor, making the soft crawling robot move forward, and the high friction area would prevent the robot from moving backward when SCPAM was cooled down (Figure 10d).

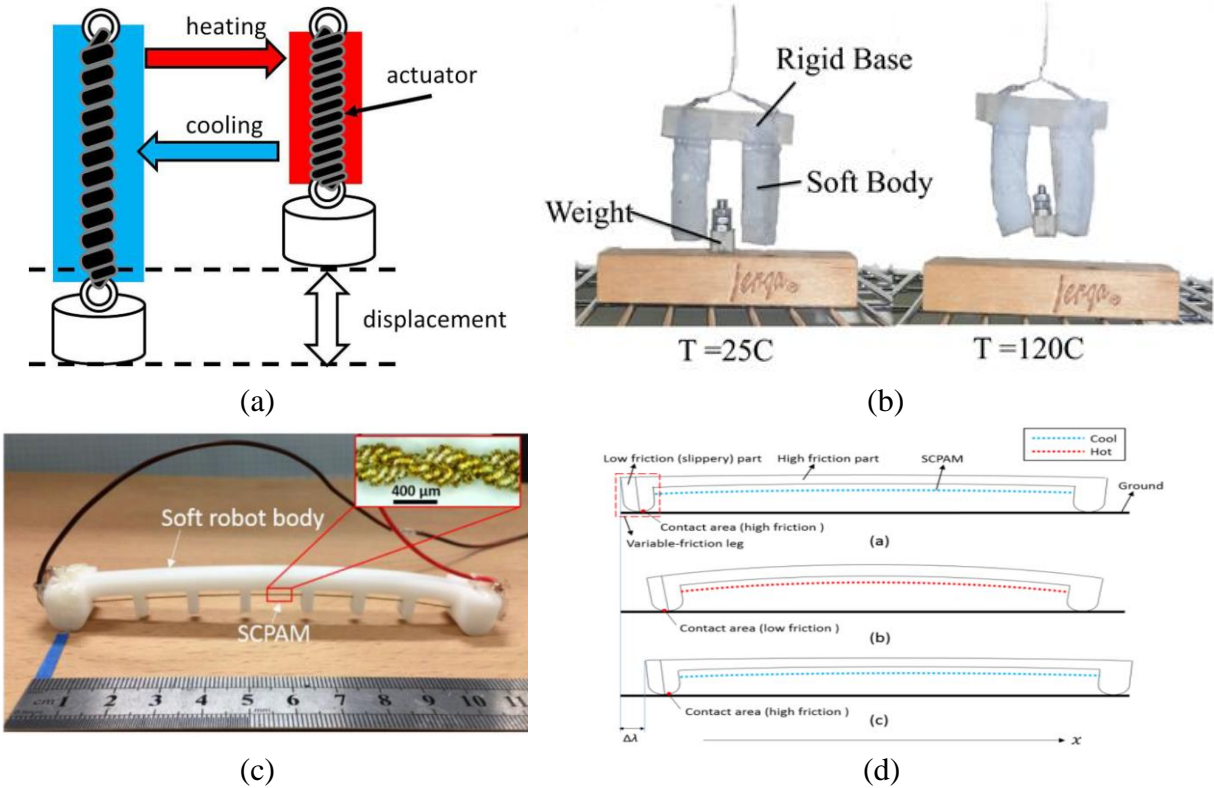


Figure 10. Soft robots driven by twisted and coiled polymer. (a) Actuation principle of TCP. (b) A soft gripper with TCPs embedded for grasping. (c) A crawling robot actuated by TCP and (d) its locomotion mechanism through anisotropy friction.

In summary, pneumatic actuation is able to achieve excellent adaptability, good compliance, and large grasping force. However, this method requires additional equipment for supplying air or hydraulic pressure, hindering the dexterity and miniaturization of the whole system. Soft robotics designed on SMAs tend to have relatively slow response due to the heating and cooling processes, and thus are not competent for applications requiring fast responsive speeds. Although DEA shows great promise in developing compact and fast actuators, it requires very high voltages (typically in the range of kilovolts) to produce enough strains/stresses for actuation, posing safety risks. On the other hand, cables possess high tensile strength but low or zero bending stiffness (highly flexible), and cable-driven actuation exhibits great advantages in fast speed and simple control. In addition, the actuation force, generated by a motor and applied through the cable, can be delivered along the

whole robotic body to minimize inertia. Moreover, based on the performance of the motor selected, the force output and responsive speed of soft robot can be easily adjusted. Table 2 summarizes the major pros and cons of these actuation approaches for soft robotics.

Table 2. Actuation Methods for Soft Robotics.

<b>Actuation</b>	<b>Advantages</b>	<b>Drawbacks</b>
<b>Cable-driven Actuation</b>	High tensile strength and flexibility. Large force output and fast response.	Noisy operation. Straightforward deformation,
<b>Pneumatic Actuation</b>	Fast speed and moderate force output. Versatile deformation.	Easy rupture of thin wall. Air hose/pump needed;
<b>Dielectric Elastomer (DE)</b>	Large actuation strain. Fast responsive time. High energy density.	Pre-stretch of film required. High driven voltage (kV~). Stack needed for large stress.
<b>Shape Memory Alloy (SMA)</b>	Provide both the actuation and structural functionalities.	High actuation current. Slow cooling down process.
<b>Magnetoactive Elastomer (MAE)</b>	Ideal for applications in enclosed and confined spaces.	High control cost for special magnetic field applied.
<b>Liquid Crystalline Elastomer (LCE)</b>	Ideal for remote control via UV illuminating.	Low force output. High demand for control environment;
<b>Piezoelectric Material (PEM)</b>	High energy density.	Pre-stretch of film required. High driven voltage (kV~).
<b>Twisted &amp; Coiled Polymer (TCP)</b>	Long cycle life. Small hysteresis.	Limited stress and Strain (than cable-driven).

### ***1.1.3 Purpose and Applications for Soft Manipulators***

The primary purpose for designing robotic hands and manipulators is to make them capable of real-world tasks like doing housework and picking and grasping objects. However, traditional manipulators are limited in capabilities of elastically deforming and adaptive conforming to targets with various sizes and profiles due to those rigid components. Adding links and joints would help improve the dexterity of robotic system but will make the structures and controls more complicated.

Hence, one of the major challenges faced by researchers is to simplify robotics structures, but still maintaining the good levels of dexterity and robustness. Thanks to the development of soft robotics, they have exhibited great superiority in grasping objects with irregular shape/fragility and showed versatile continuum deformations and locomotion for flexible manipulation. Soft manipulators are spreading in diversified fields (Figure 11). For example, a soft robotic endoscope for safer surgery due to its softness and great navigating ability (Figure 11a),<sup>[71]</sup> a locomotive robot equipped with soft arm for search and rescue in limited space (Figure 11d),<sup>[72]</sup> various soft grippers for packaging lines (Figure 11b),<sup>[73]</sup> fruit harvest (Figure 11c),<sup>[74]</sup> and deep sea research (Figure 11e) owing to their high adaptiveness and moderate force exertion.<sup>[75]</sup> Also, a soft pneumatic actuator for disabled people as life assistance (Figure 11f).<sup>[76]</sup>



(a) Medical endoscope



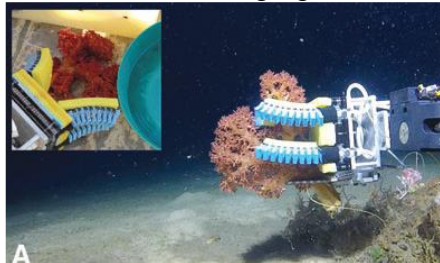
(b) Packaging line



(c) Field harvesting



(d) Search and rescue



(e) Harsh environment



(f) Life assistance

Figure 11. Potential applications for soft manipulators.

#### ***1.1.4 Significance and Methods of Realizing Variable Stiffness of Soft Manipulators***

The inherent compliant feature of soft robotics poses critical challenges for achieving high structural stability and high loading capacity for some specific applications. For instance, inherent softness allows the soft gripper to operate with irregular and fragile objects with only low weights.

Similarly, soft surgery manipulators featuring high DOFs are used to reduce patient's trauma by actively bypassing the biological structures. However, they are not stiff enough to exert enough force on the target or prevent unwanted deformations under weights of organs.<sup>[77]</sup> To overcome this, one potential solution is to modulate stiffnesses of soft robotics so that they are able to sustain external loads (including self-weight) and exert large forces for robust interactions when needed. A variety of methodologies and materials have been investigated to adjust the stiffness, including electrorheological (ER) and magnetorheological (MR) fluids,<sup>[78]</sup> pneumatic jamming,<sup>[79]</sup> shape memory polymers (SMPs),<sup>[80]</sup> and low melting point alloys (LMPAs).<sup>[81]</sup> ER/MR fluids can change their rheological properties under electric/magnetic field. However, their stiffness variation range is limited, and the requirement of external electromagnets/super-capacitors as well as leak-proof packaging would hinder further applications.<sup>[82]</sup> SMPs can alter their elasticities by heating them above the glass transition temperatures and have been adopted for selective stiffness change and DOFs locking.<sup>[83]</sup> Similarly, LMPAs can switch between solid and liquid states for providing necessary stiffening effect when needed and their melting temperatures are usually low (42°C-70°C). In addition, self-healing can be intrinsically realized by the recrystallization of LMPAs.<sup>[81, 84]</sup> Hao et al. embedded channel shaped LMPAs into a pneumatic soft actuator to attain a bending stiffness enhancement of 3.5 times (Figure 12a-b).<sup>[84]</sup> Zhang et al. integrated SMP layer into a fully printed pneumatic soft actuator to increase its stiffness by 120 times without sacrificing flexibility (Figure 12c-d).<sup>[85]</sup> SMPs and LMPAs have presented great potential in soft robot applications because they can be stimulated by direct Joule heating, and their stiffness variant ranges are large. Nevertheless, their slow response speed, especially long cooling time for them to transform from soft state back to stiffer state, has greatly restricted the practicability of these phase changing solutions.

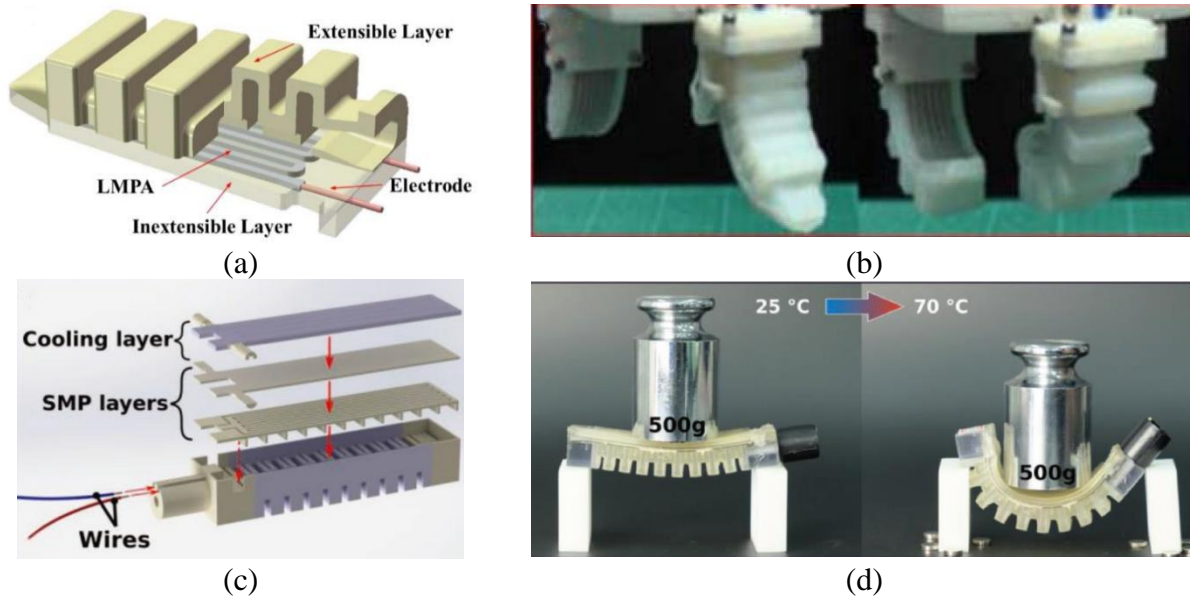


Figure 12. Variable stiffness via low-melting-point alloy and shape memory polymer. (a) Design of a soft finger embedded with LMPAs. (b) Bidirectional bending of the soft gripper with molten LMPAs. (c) Schematic of a SMP-based actuator. (d) Demonstration its stiff-soft duality.

Other than the sluggish responses of phase-changing methods, jamming mechanism, which takes advantage of the natural phenomenon of transitioning a low-density set of packaged matters into a rigid and high-density packing through applying external stress, can achieve faster response (in seconds) and higher stiffness variation. Applying vacuum is the most efficient way but requires the system to connect with tube and vacuum pump, an addition payload.<sup>[86]</sup> Besides the commonly utilized particles, planar layers and fiber bundles can also serve as packing matters and can achieve different DOF restricting purposes, as depicted in Figure 13a. Pei et al. integrated particle jamming mechanism into a gripper and enhanced its loading capacity by more than 3 times (Figure 13b).<sup>[87]</sup> Xie et al. applied jamming layer structures into a soft finger actuator to increase its initial stiffness from 16 to 44 N/m by 30 kPa vacuum pressure (Figure 13c).<sup>[88]</sup> And a fiber jamming based module was designed by Jadhav et al. and achieved a stiffness improvement by ~8 times (Figure 13d).<sup>[89]</sup> In general, particle jamming is vulnerable to bending load and cannot resist large tensile stress but exhibits the highest flexibility when unjammed. And bending of layer jamming system is confined

to a single plane. While fiber jamming usually exhibits better tunable bending stiffness compared to particle jamming and more versatility compared to layer jamming.

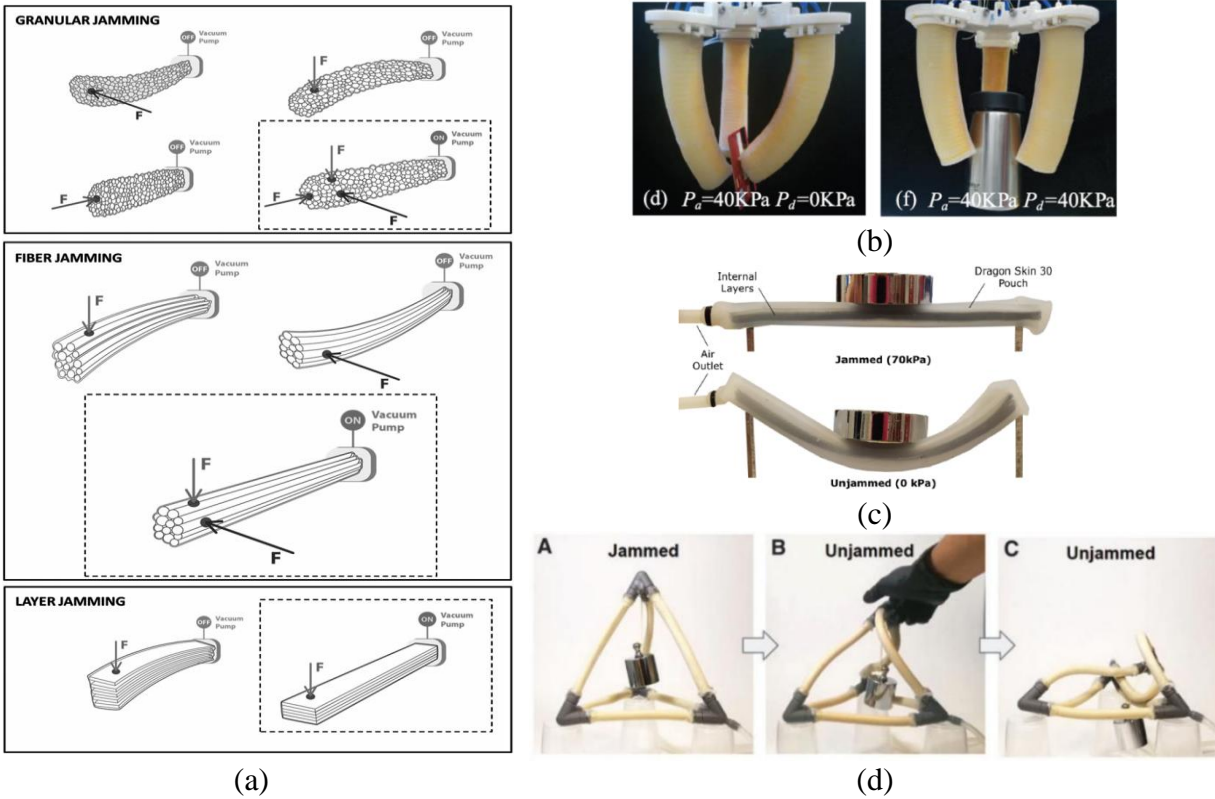


Figure 13. Variable stiffness through particle/layer/fiber jamming. (a) Jamming actuation based on different matters packed. (b) A particle jamming gripper with improved loading capacity, (c) a layer jamming strip with improved bending stiffness, and (d) a fiber jamming tube structure.

### 1.1.5 Compliant Tactile Sensors for Soft Robots and Human-Machine Interface

As for robot manipulation systems, sensing units are one of the most essential components, which can be briefly classified into motion, biological, chemical, and tactile sensors. Among these sensor types, tactile sensors are of great significance for robotic application, as they impart robotics with the capacity of probing the environment and enabling feedback controls. For example, making a robotic gripper capable of more precise grasping. Tactile sensors can convert mechanical energy in diversified forms, such as force, strain, and friction, into electrical signals for decoding. Previous tactile sensors are mainly taking advantage of piezoresistive, capacitive, piezoelectric, and optical

mechanism (Figure 14).<sup>[90]</sup> For piezoresistive and capacitive sensors which require external powers, their resistivity/capacitance would vary with mechanical deformation. Although piezoresistive one is free of electrical noise, it just responds within low frequency domain. The situation for capacitive sensor is opposite (high frequency domain). Piezoelectric sensor can achieve self-powered sensing via direct piezoelectric effect and exhibits high frequency response but suffers from limited strain range. Sensor using optical technology is accurate and sensitive but needs cameras. As a result, for better integration of tactile sensors with soft robots, there is a great need for developing soft sensors with high sensitivity, reliability, flexibility, large measurement range, ease of use and maintenance, and moderate cost.

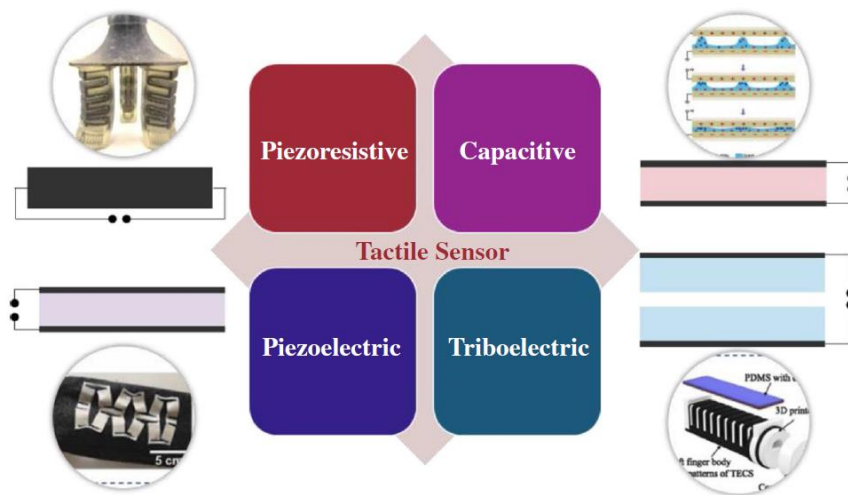


Figure 14. Schematic of major types of tactile sensing for soft robotics.

Triboelectric nanogenerators (TENGs) based on the contact electrification and electrostatic induction have emerged recently as a promising technology for generating electricity by exploiting almost every type of mechanical motions, like touching, sliding, rotation, and vibration.<sup>[91]</sup> Besides energy harvesting, the induced electrical energy from TENGs can also be used as a response signal to identify change in motion or deformation of structures without the requirement of any additional power source (i.e., self-powered). The technology (both energy harvesting and sensing) has proven

its great potentials in numerous fields, from daily usage as health monitors and energy harvesters during exercises to advanced sensors for industries, as shown in Figure 15a.<sup>[92]</sup> TENG devices also have exhibited other desirable merits, like low weight, high sensitivity, excellent design versatility, and environment-friendliness. Most importantly, owing to the wide material choices for fabrication, TENGs can possess high flexibility and stretchability, making them promising candidates for soft robotics applications.<sup>[93-95]</sup>

Besides functioning as sensing units for soft robotics, TENGs can be also used as advanced interfaces for communication usages with human and device, which is known as human-machine interface, HMI (Figure 15b).<sup>[96]</sup> Like conventional keyboard and mouse associated with computers, they function as channels to let us convey our command and purpose to electronic devices or others. In the recent years, wearable devices for capturing human motions have drawn great attention due to their broad spectrum of applications, such as healthcare, biomedical diagnostics, entertainment, VR/AR, and HMIs.<sup>[96]</sup> And plentiful mechanical energy can be taken advantage of throughout the human body like motions of foot, ankle, knee, waist, arm and hand regions, depending on the types of application. Owing to the flexibility in design (converting almost any type of mechanical energy) and wide material selections, many HMI devices have been developed, e.g., He et al. designed an all-textile TENG wearable glove for teleoperated human-machine interactions, making operations of robotics with better immersive experience.<sup>[97]</sup>

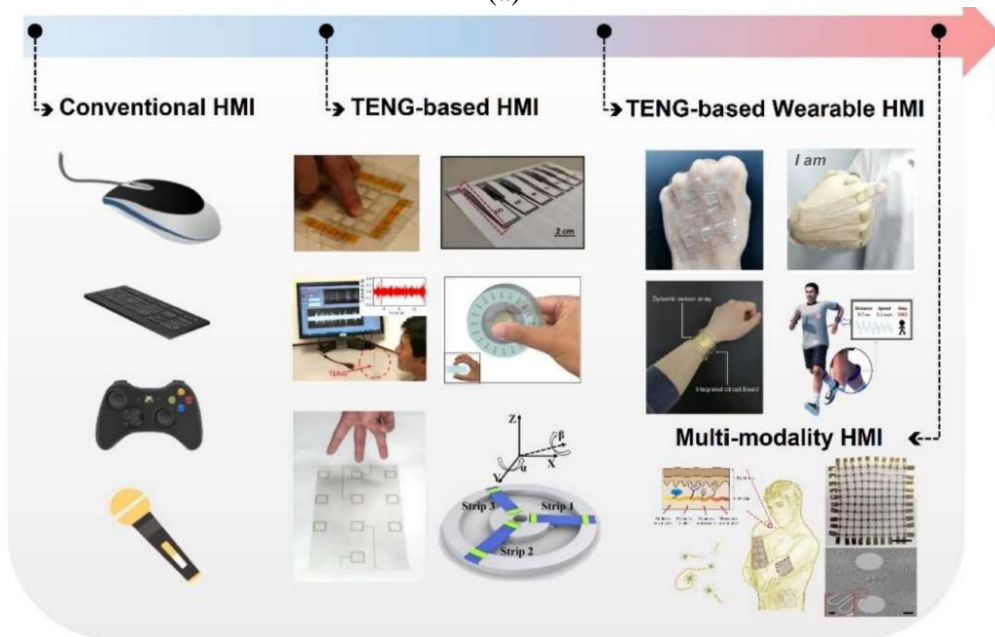
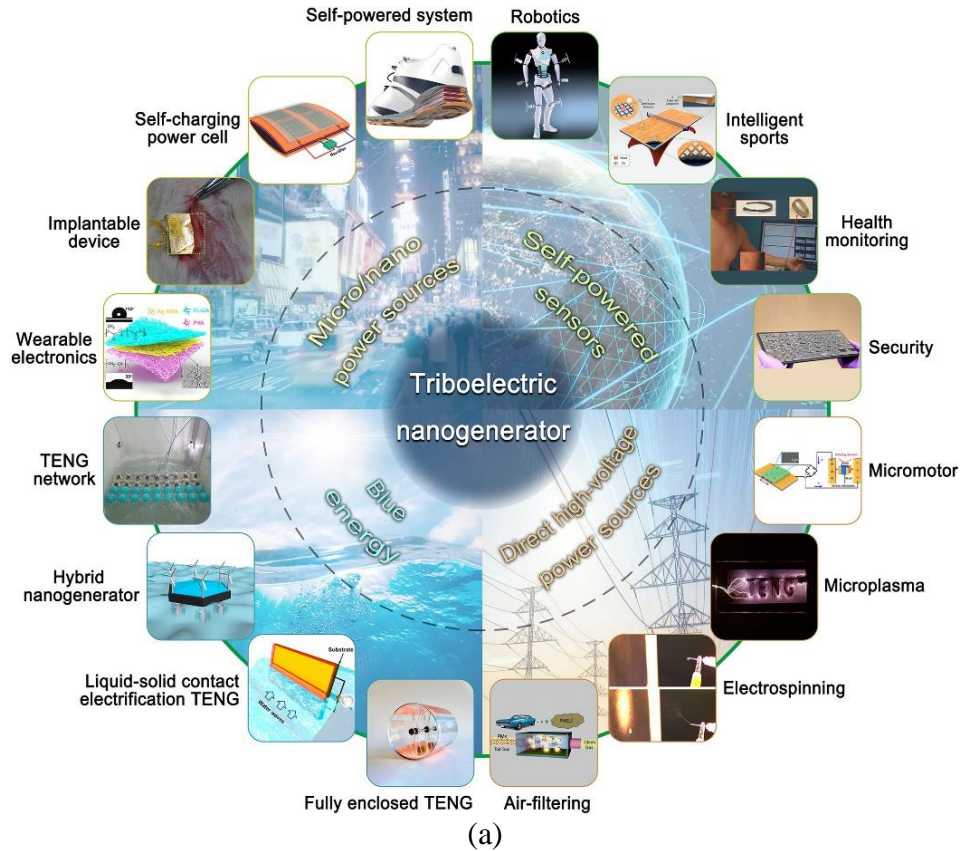


Figure 15. Wide applications of TENG harvester/sensor and its potentials in HMI.

## 1.2 Research Goal

In view of background investigations for soft robotics (especially for manipulators), great effort should be put into discovering effective actuation methods and matching behaviors of robots with specific application requirements, for example, making a soft gripper apparatus able to handle products with considerable force exertion and speed during field harvesting. Also, because of the inherent softness and continuity in deformation of soft robots, flexible sensors, and other features such as self-healing and variable stiffness, are in high demand for integration to make soft robotics more competitive in efficient and safer human/environment-machine interactions.

The overarching goal of this dissertation is to help establish a highly integrated and entirely soft manipulator consisting of both arm segment and end effectors with features like high dexterity via only concise control, adjustable driving speed, force output, and stiffness, self-powered contact and bending perceptions, and teleoperability by wearable HMI. Cable-driven actuation was chosen as the driving mechanism for robots due to its wide range of selections in force and speed outputs, and TENG technology was utilized to develop soft tactile sensors and wearable interface. By integrating the as-mentioned features into a soft robotic system, we aimed to pave the way for robust real-world applications of soft manipulators. And the entire work was divided into several sub-tasks as follows:

In Chapter 2, initial attempt to develop a versatile cable-driven soft gripper was made here, including designs of fundamental cable-driven robotic structures (such as notch and cable through-hole), finite element analysis for the mechanical behaviors (considering cable-driven effects), and fabrication of the actuator. The designed cable-driven finger actuator was capable of bidirectional bending through the actuation of a miniature DC motor and thus the assembled gripper apparatus could handle objects with different profiles and sizes.

And for Chapter 3, efforts were put to make the soft cable-driven finger actuator intelligent. A similar robotic structure as that in Chapter 2 was adopted and integrated with two types of TENG sensors, including soft tactile sensors bonded on the phalanges of the actuator to perceive contact pressure or grasping force, and a compliant curvature sensor embedded inside the robotic body to predict the shape and size of grasped objects. In this part, the mechanisms and output behaviors of different kinds of TENG units were studied through numerical methods and finite element analysis, and the calibrations of fabricated TENGs were conducted. With the combination of self-powered TENG technology, this smart soft actuator driven by cable could effectively sense the environment and pave the way for safer human-machine-environment interactions.

An entirely soft cable-driven manipulator was designed in Chapter 4. Detailly the structures of the cable-driven finger actuators were improved via multi-material designs for better safety and dexterity, and a soft omnidirectional arm was designed for navigation of the gripper apparatus. In addition, variable stiffness for the soft arm was realized by embedding LMPA tubes into the robotic body, so as to achieve a robust operation for the manipulator. On the other hand, a wearable TENG finger patch was designed for robot teleoperation. Triggered by the flexion and extension of human finger, the soft manipulator could be remotely operated for better human-machine interaction.

Finally in Chapter 5, another method to realize variable stiffness for the robot arm proposed before was investigated, as the LMPA method adopted in Chapter 4 took a relatively long time to alter the stiffness of the robotic system. In detail, a spine-inspired hybrid structure, driven by cables, was designed to achieve fast stiffness modification, and its stiffness variation behavior was studied through both numerical and finite element analysis.

## CHAPTER 2: SOFT CABLE-DRIVEN FINGER ACTUATOR

### 2.1 Objective

In this chapter, we aimed to dig into the cable-driven mechanism and develop a soft finger-like actuator that was capable of bidirectional bending through minimum amount of power sources (i.e., DC motor). This finger actuator with the capacity for both extension and flexion could greatly extend the grasping range (i.e., object with a larger size/more complicated shape) for an assembled gripper device. To attain this initial goal and accumulate experience for developing an entirely soft cable-driven manipulator, the following sub-objectives were realized sequentially:

- The body of the soft finger actuator was designed with appropriate notch and cable hole features to realize the bidirectional bending function and form a conformal contact with objects of diversified shapes and sizes.
- A gripper device with a 3-finger configuration was established with a minimum number of motors required for simultaneously extending and bending the finger actuators.
- Finite element analysis for mechanical performance of the actuator was conducted with cable-pulling effect to predict its locomotion and strain/stress distribution, which would greatly improve the efficiency and accuracy in simulation of cable-driven soft robotics.
- The fabrication processes for the soft cable-driven robot were investigated and verified to achieve a robust soft finger actuator, and its overall performances were validated via simple tests.

### 2.2 Method

#### 2.2.1 Design of Bidirectional Bending Gripper

Inspired by the configuration of human fingers, the soft cable-driven actuator was designed with three phalanx structures which were separated by triangular cuts with an angle of  $45^\circ$ . Hence,

each phalanx induced a 90° angular displacement with respect to the previous one. The length of the phalanx was kept the same except for the bottom one which had fillet feature to function as the curved tip mimicking the human finger. Figure 16a illustrated the geometrical features of the soft actuator with its specific dimensions demonstrated in Figure 16b. There were two parallel holes in the soft finger body to deploy nylon cables. One end of the cable would be fixed at the soft fingertip, forming a fixture point to delivery cable-pulling forces and the other end would be twined around the spindle of a miniature DC motor. By dragging the cable, the actuator containing phalanx feature would deform in either convex or concave status, making the corresponding gripper device capable of expanding its gripping range and perform effective grasp. In order to reduce the friction between the cables and soft materials, the cables were inserted through plastic tubes which were embedded and bonded inside the phalanges (inner side of the finger body), and both ends of the backside hole. When the actuator was fully bent by rotating DC motors, a stable enveloping grasping profile could be achieved for the soft finger body. In addition, the soft finger body would be formed via silicone rubber (Ecoflex 30, smooth-on Inc., USA) which could impart the gripper with passive adaptability. This material appears a water white translucent color, and its mechanical behavior can be adjusted by varying mixing ratios between its bi-component Part A and B (1:1 utilized in this study, with a 100% modulus of 10 psi).

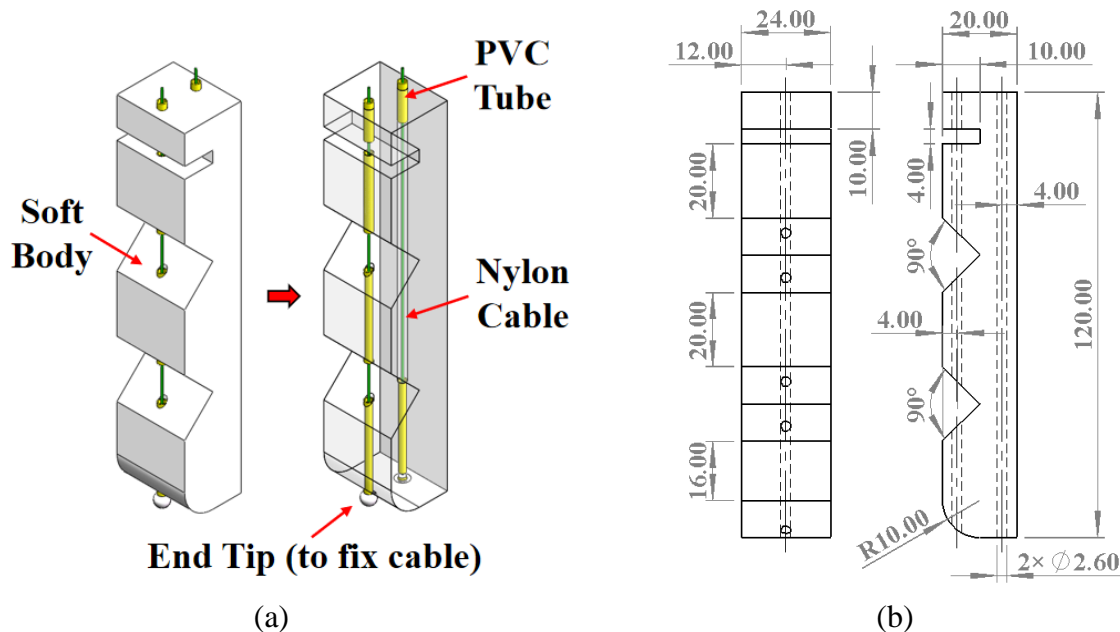


Figure 16. Structure of the soft cable-driven finger actuator capable of bidirectional bending. (a) Major components of the soft actuator. (b) Dimensions of the soft finger body.

Then a cable-driven soft gripper was comprised of four parts: 1) three identical soft finger actuators as mentioned before, 2) a support structure with its accessories, which were 3D printed from poly lactic acid (PLA) material, 3) three small DC motors providing power to pull the cable and 4) a gripper holder to demonstrate grasping processes (Figures 17a and b). As discussed before, each soft finger actuator could be driven by two opposite cables embedded in the body. However, if each cable was controlled by an individual motor, this soft gripper needed six motors in total on the holder, which would make the gripper apparatus bulky and lead to a complicated control system. A spindle for the shaft of motor was designed which consisted of two identical grooves for twining the two cables in the opposite directions, as described in Figure 17c. When the motor was actuated clockwise, the cable close to the inner side of the soft actuator would be pulled up (inward bending of the soft finger actuator) and the other cable would release its pre-rotated coils. However, during this release process, this cable would jump out of its original pathway and cause unstable behaviors of the control system. To solve this, a spindle cover was made to restrict the unexpected “jumping”

of cables. The inner arch surface of the cover was of the same dimension as the largest outer profile of the spindle. The allowable space for the cables was labeled in Figure 17c. After integrating the soft finger actuators with the 3D-printed holder, rotating the cables around the spindle in different directions, covering the spindle and motor to restrict their movements, and connecting the motors to the control circuit, this soft gripper apparatus could begin its gripping operations.

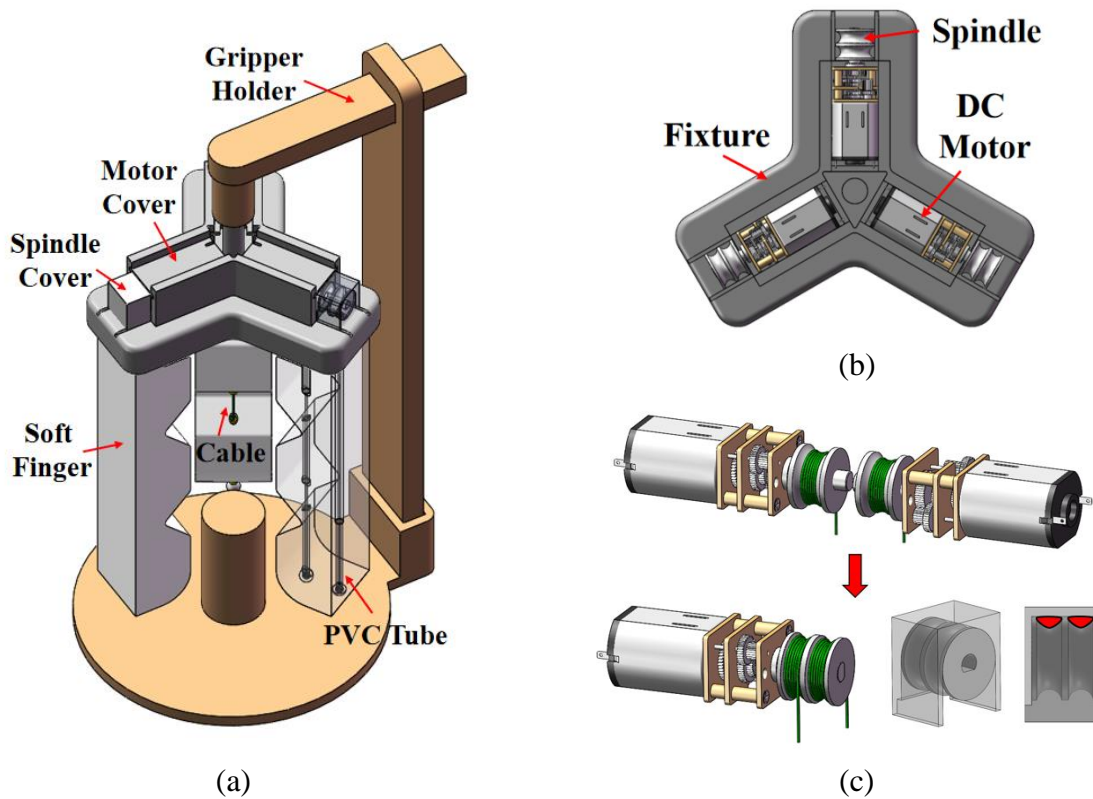


Figure 17. Structure of the soft bidirectionally bendable gripper. (a) Components and assembly of the gripper. (b) Holder for the soft finger actuator and motor installation. (c) Spindle to control two cables with a cover structure.

### 2.2.2 Finite Element Analysis for Soft Finger Actuator

Before fabricating the soft finger actuator, its mechanical performances were investigated through finite element method (FEM), including its deformation responses upon cable pulling and the corresponding strain and stress distributions. Nonlinear finite element analysis was used to take large deformation of soft material into consideration, and the modelling of cable and its integration

with soft robot were significant for accurate prediction of robot deformations. However, simulating cables in a virtual environment was challenging because they cannot bear axial pressure and shear force, not to mention the interactions with robotic body. Here, we first turned to SOFA framework which had been widely used for surgical and biomedical soft robot applications.<sup>[98]</sup> The algorithm utilizes an iterative method to figure out ordinary differential equations and transfers the boundary conditions via Lagrangian multipliers, and the most important thing is that cable module has been included. The simulation/coding process and its results were shown in APPENDIX A. The method for modeling a cable-driven robot was efficient but suffered from inaccuracy at large deformations.

Then, the modelling of cables and their integrations with the finger actuator was performed in the Abaqus 6.14 environment. Solid element was used to discrete the cable and a softer material property was applied to the structure so as to decrease its bending stiffness. Such modification was made because we only cared about the deformation and strain & stress of the soft finger structure. To prepare the simulation model, fillet features were removed from the finger actuator, and a cable structure with an enlarged diameter (for the purpose of facilitating convergence) was tied to a disk-like structure functioning as the cable fixture. The tie constraint was applied to the surfaces of the cable tip and cable fixture (Figure 18a), so as to transfer the motions of cables to the soft fingertip. In addition, self-contacts of the notches and surface-to-surface contacts between the hole and cable, and the cable fixture and fingertip, were set (Figure 18b). In detail, the tangential contact behavior was modeled by penalty method with a friction coefficient of 0.6, and the normal contact behavior was simulated as hard contact. As for the boundary conditions, the end of the soft finger body was restricted in all DOFs to simulate the real situation, and a displacement load was applied to the end of the cable instead of a concentrated force (Figure 18c). In the end, all components were meshed by 4-node tetrahedral elements (Figure 18d), and a 3-term Ogden model was used with the factors

( $\mu_1=0.001887$ ;  $\alpha_1=-3.848$ ;  $\mu_2=0.02225$ ;  $\alpha_2=0.663$ ;  $\mu_3=0.003574$ ;  $\alpha_3=4.225$ ;  $D_1=2.93$ ;  $D_2=0$ ;  $D_3=0$ .), to model Ecoflex 00-30. Static/General analysis was performed to predict the deformation and the corresponding strain and stress distributions of the soft robots.

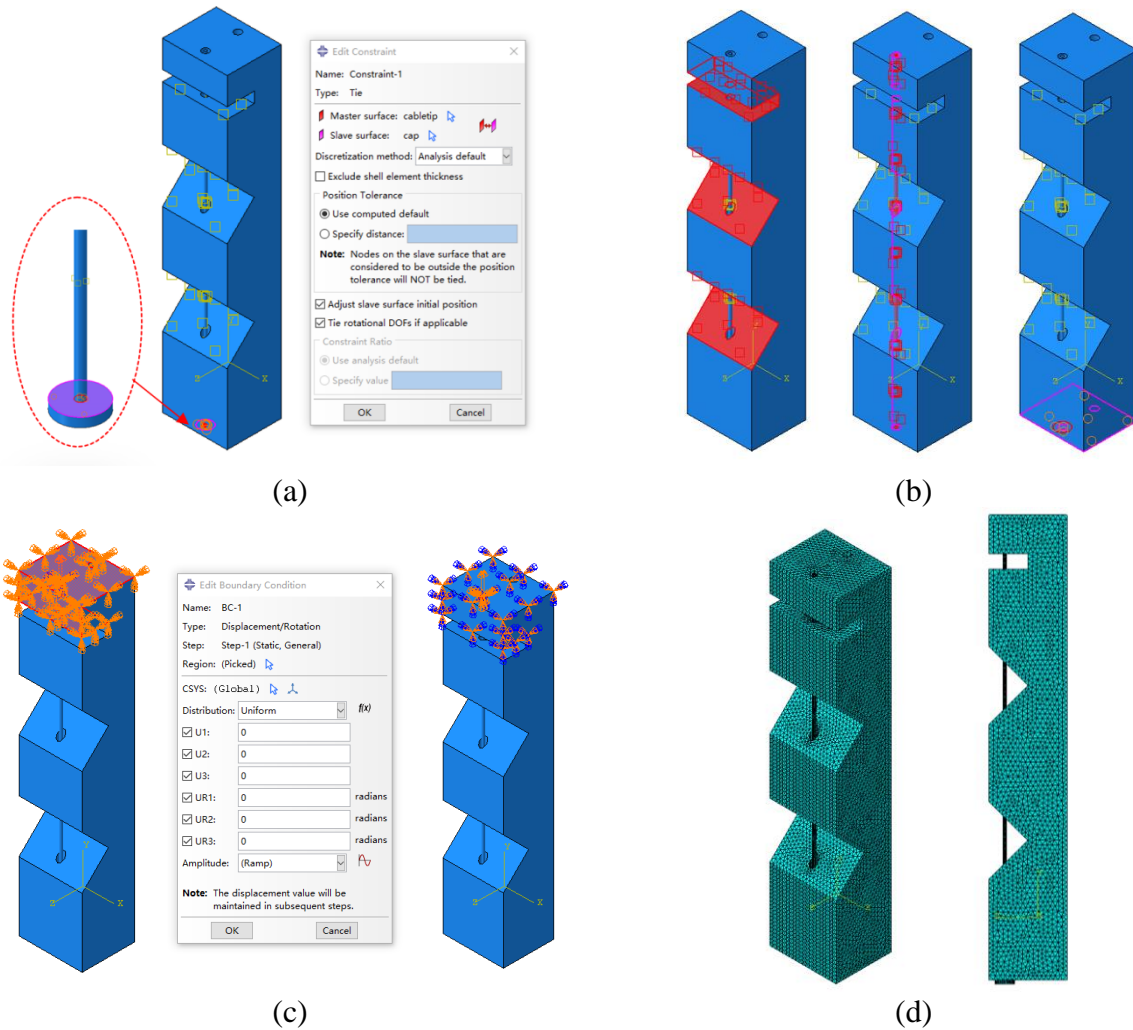


Figure 18. Simulation model for predicting mechanical behaviors of the actuator. (a) Constraint (tie) setup for the cable and cable fixture. (b) Surface contact setup for the actuator. (c) Boundary condition setup. (d) Meshing for the soft finger actuator.

As the top region of the soft finger actuator was fixed in all DOFs, an upward displacement load would be applied to the top surface of either cable to induce inward or outward deformation. We set a cable pulling displacement of 30 mm to predict the deformation tendency of the actuator, and the simulation results were illustrated in Figure 19. At first, the displacement load was applied

to the cable embedded in the inner side of the soft finger, and it was seen that the notches squeezed themselves and the soft finger would bend inward in an easy manner. As could be indicated by its stress distribution (Figure 19a) under fully bent status (30 mm cable pulling displacement), stresses around the cable holes (especially the entrance and exit of phalanx structures) were relatively high, followed by the stresses near structural notches. As plastic tubes would be inserted in the phalanges, the actual stresses induced nearby would be much lower. As a result, this soft finger actuator would be safe enough to deform through cable pulling (as the tensile strength of Ecoflex 00-30 is around 1.38 MPa).

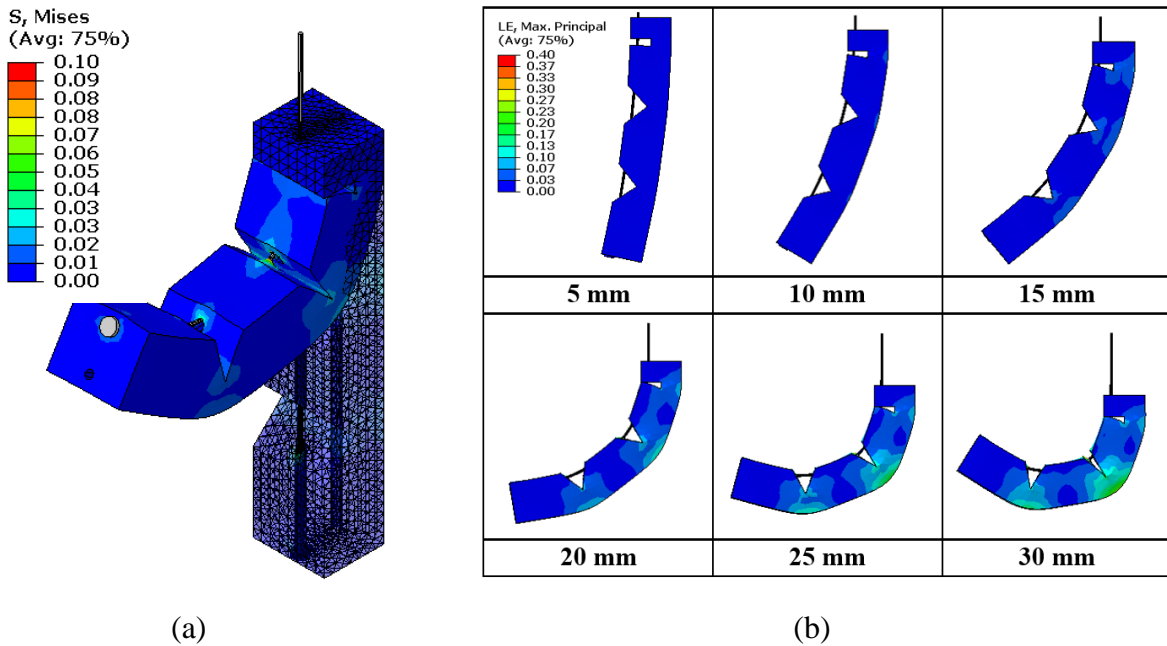


Figure 19. Simulation result for inward bending of the soft finger actuator. (a) Stress distribution of the actuator at a cable pulling displacement of 30 mm. (b) Strain distributions and deformation of the finger under different cable pulling displacements.

Figure 19b illustrated the inward bending deformations of the soft actuator under different cable pulling displacements, as well as the corresponding strain distributions. It was found that the strains around the backsides of the notch structures were relatively high, the highest of 0.27 when the soft finger was fully bent via cable pulling. All these results showed that this soft finger actuator

could function well under moderate cable pulling. Differ from the previous research on simulating cable-driven soft robotics which only applied an equivalent force on the specific node in the FEM model (near the cable fixture), this simulation model fully considered the interactions between the cable and the soft body and offered a more precise prediction for soft robotics. Figure 20 illustrated the simulation results without consideration of cable-pulling effect. It could be easily noticed that, without the interactions with cable, the notch structures distributed along the soft finger body could not be effectively squeezed and the tip end of the soft finger would be less bent.

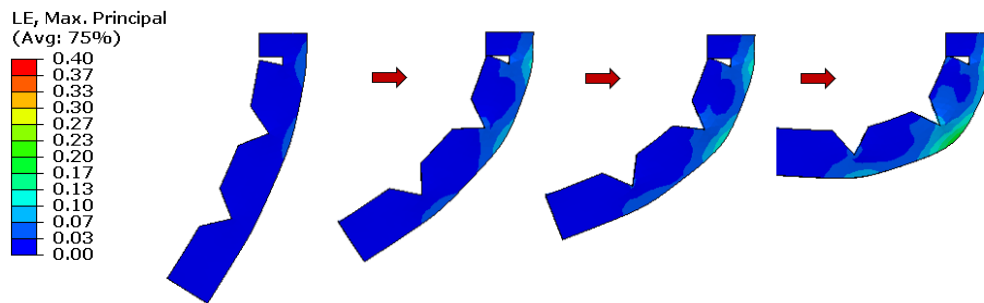


Figure 20. Simulation results for the soft finger actuator without considering cable pulling effect.

In Figure 21, the same loading condition was applied to the cable embedded in the backside of the actuator and the soft finger actuator would extend outward accordingly. However, due to no existence of notch structures on that side, the soft actuator would get harder to deform in that way, which meant a larger force/torque was required to pull the cable to induce such outward extension. Large stresses were found near the areas where the cable was inserted from and fixed, which could be largely reduced through embedding plastic tubes as discussed before (Figure 21a). In addition, the outward bending deformations of the soft actuator under different cable pulling displacements were illustrated in Figure 21b, along with its strain distributions. As could be observed, the rubber materials along the backside of the soft finger suffered from higher strains under outward bending than under inward bending.

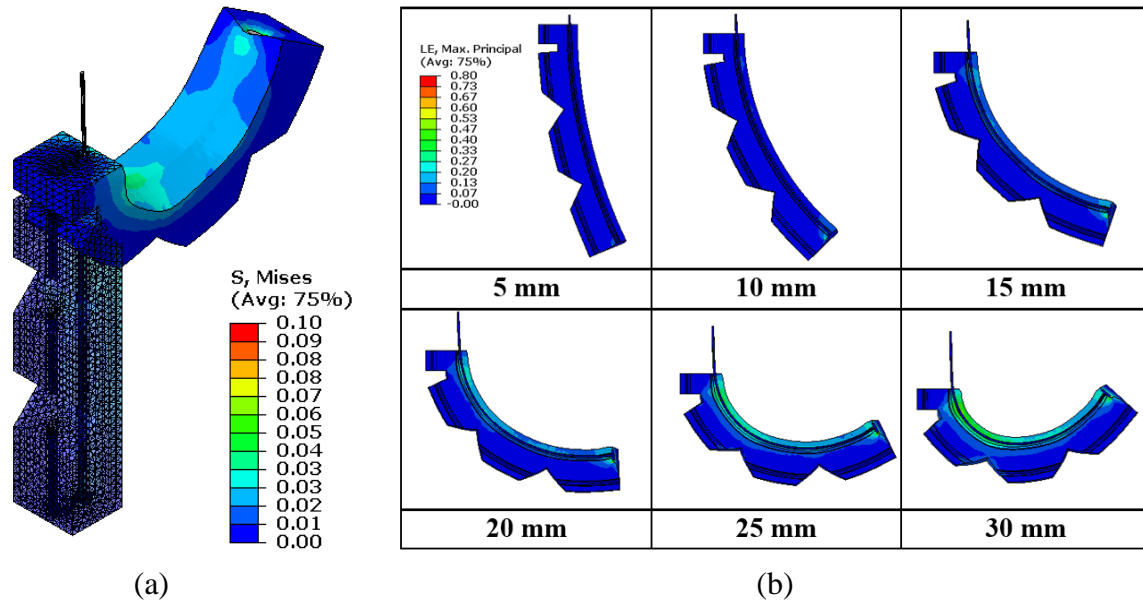


Figure 21. Modeling result for outward bending of the soft finger actuator. (a) Stress distribution of the actuator at a cable pulling displacement of 30 mm. (b) Strain distribution and deformation of the finger under different cable pulling displacements.

### 2.2.3 Fabrication of Soft Finger Actuator

The fabrication procedure of the soft cable-driven finger was shown in Figure 22 including the casting and assembling phases. The mold for casting rubber finger body was fabricated via 3D printing technology, using poly lactic acid (PLA), with considerable stiffness and heat resistance, and two polyvinyl chloride (PVC) plastic tubes were inserted into the parallel channels in order to form holes inside the soft finger. For the purpose of preventing the leakage of material, knots were tied and tightened on both ends of tubes. After preparation of the mold, the fluidic silicone rubber was poured into it. Then the mold was placed in an oven for degassing and heated to 80°C for 2h to ensure the curing quality for the materials. Finally, the tubes were removed before the soft robot body could be demolded, creating pathways for cables. In this research, the silicone rubber material, Ecoflex 00-30, was frequently employed owing to its low shore hardness, i.e., high flexibility and stretchability. So, the soft finger body could be easily actuated through miniature DC motors. Also, tensile strength and elongation at break of Ecoflex 00-30 are higher than Ecoflex 00-20, i.e., safer

upon large deformations. Ecoflex 00-35 possessing the same mechanical properties as Ecoflex 00-30 was abandoned because of its short cure time, posing difficulties in preparing the liquid mixture of silicone rubber and pouring into the mold. The major material properties for Ecoflex series were described in detail, in Table 3.

Table 3. Material properties for Ecoflex series

<b>Ecoflex Series</b>	<b>00-10</b>	<b>00-20</b>	<b>00-30</b>	<b>00-40</b>	<b>00-50</b>
<b><i>Density</i></b>	1070 kg/m <sup>3</sup>				
<b><i>Cure Time</i></b>	4 h	4 h	4 h	5 min	3 h
<b><i>Tensile Strength</i></b>	827 kPa	1103 kPa	1379 kPa	1379 kPa	2172 kPa
<b><i>100% Modulus</i></b>	55 kPa	55 kPa	69 kPa	69 kPa	83 kPa
<b><i>Max. Elongation</i></b>	900%	845%	900%	900%	980%
<b><i>Shrinkage</i></b>	<0.1%	<0.1%	<0.1%	<0.1%	<0.1%

The next stage was to integrate nylon cables into the soft finger. As for the holes inside the silicone body, the tubes were cut into segments with approximately the same lengths as the phalanx structures of the soft finger, while for the hole in the backside, only tube segments put on the ends were required with suitable length. By doing so, deformations of the soft finger actuator would be less constrained, and its stability could be maintained through reducing the potential friction during cable-actuation. In addition, the stress and strain concentrations of the soft silicone material around the hole regions, where cables entered from and existed, could be reduced, or removed, as indicated from the simulation results. Then, the segments of PVC tubes with a thin layer of fluidic silicone rubber applied around were inserted and embedded in the corresponding hole channels. In the end, two nylon cables (fishing line) were guided through the tubes with one end connected to the spindle on the DC motor and the other fixed to the soft fingertip by utilizing a glue gun, functioning as the cable fixture points.

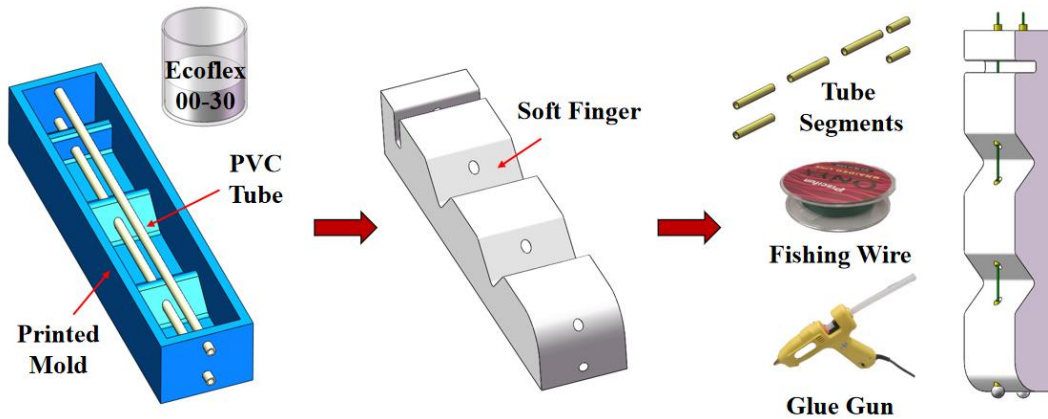


Figure 22. Fabrication process for the soft bidirectional cable-driven actuator.

## 2.3 Result

### 2.3.1 Illustration of Bidirectional Bending

Then a simple bending experiment was conducted with the single soft finger attached to a 3D printed holder and driven by a miniature DC motor. The bending deformations of the soft finger were demonstrated under different motor rotation angles (both clockwise and anti-clockwise). For inward bending of the actuator, it could be easily deformed via squeezing the notches between the phalanges. All the two notches would be fully made use of when the motor rotated a degree of  $540^\circ$  and such enveloping profile of finger could offer enough support to the lower surface of the object. As for the outward extension, the soft finger actuator deformed with the curvature of its outer layer decreasing uniformly and such large deformation would increase the tip-to-tip displacement of the gripper (i.e., grasp objects with larger cross-sections). Compared with the simulation results, it was found both the inward and outward bending of the finger could be predicted (the perimeter of the spindle groove where the cable rotated around was 24 mm). However, the result was less accurate for the inward bending of the actuator than the outward situation due to surface contact interactions of the notch structures and the cable structure with an enlarged cross-section for better convergence (i.e., enlarged bending stiffness).

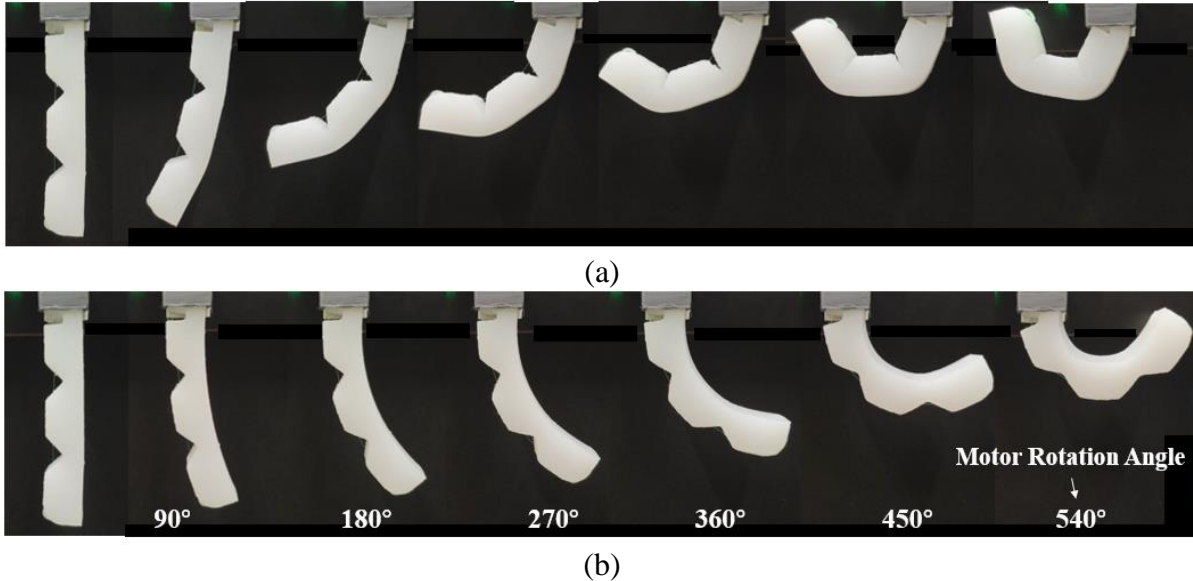


Figure 23. Bidirectional bending of the soft finger actuator under different motor rotation angles. (a) Inward and (b) outward bending of the finger actuator with an increment of  $\frac{1}{4}$  motor rotation (clockwise/counterclockwise).

### 2.3.2 Grasping Process of Soft Gripper

The process for grasping an orange using an assembled cable-driven gripper was shown in Figure 24. At first the gripper could not grab the orange due to its relatively small opening. So, the motors would need to rotate counterclockwise to expand the opening of the soft gripper, and then an orange was placed on the top of a small column installed on the platform. After that, the motors began to rotate clockwise, and the soft fingers would turn to their original position and bend inward gradually to get in contact with the object. The bottom phalanx of the fingers would lift the orange and provide increasing gripping forces to it along with the supports from other phalanges. Keeping rotating motors in that way would make the soft gripper grasp the orange more tightly and almost fully cover the object. The process of grasping indicated that the bidirectional bending capacity of the soft gripper could greatly improve its operation quality (i.e., better gripping position and force exertion, and less interference with the targeted objects).

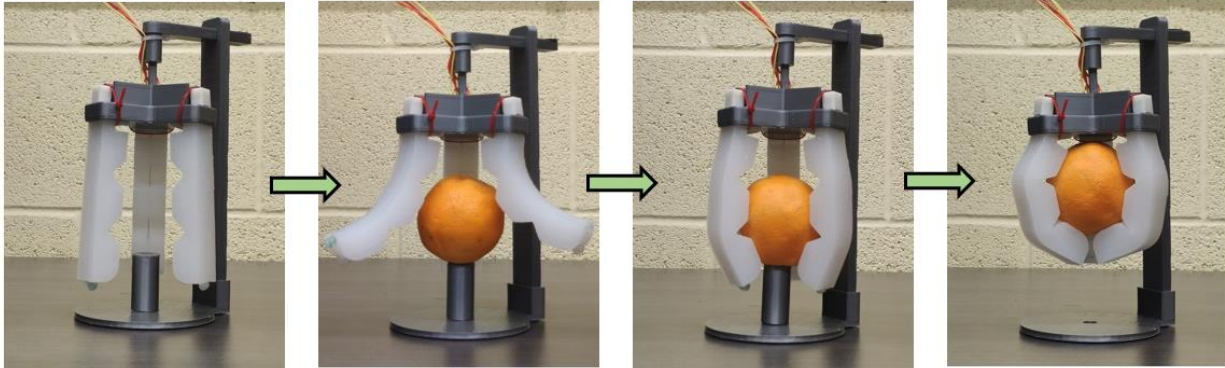


Figure 24. Demonstration of orange grasping using the bidirectional soft gripper.

## 2.4 Conclusion and Discussion

The soft cable-driven finger actuator which is capable of bidirectional bending is developed in this initial attempt. By embedding two nylon cables in the soft robotic body, and then connecting the cable to a specific designed spindle fixed on a miniature DC motor, the soft finger actuator can perform large-scale expansion to enlarge its grasping range when assembled as a gripper apparatus, as well as inward bending to form an enveloping profile for gripping objects. Such dexterous finger actuator can be easily fabricated in different shapes and sizes, actuated via straightforward cable-driven mechanism, and assembled into a gripper with specific configuration for different purposes, and what is more, its output behaviors can be adjusted with little effort by replacing the DC motors with preferred torque and speed output. The proposed soft finger actuator design can be applied to a variety of scenarios, like pick-and-place, packaging line, and field harvesting. With the capacity of extending its grasping range (i.e., outward bending of the finger body), the soft gripper can take on various challenging tasks with a minimum cost in control and maintenance.

To validate the robotic design, the nonlinear FEM is used to simulate the deformation and strain & stress distributions for the soft body with consideration of cable effects, which is different from the previous works on modeling cable-driven robots. The simulation results could predict the mechanical behaviors of the soft finger with the appropriate accuracy, and thus the same simulation

setups can be used for the following design jobs of other cable-driven robotics. Then the fabrication processes for this soft cable-driven finger are proposed. The fabricated bidirectional finger actuator has been tested in the two bending directions and an assembled gripper can perform robust gripping operation as well. However, the function for bidirectional bending of the soft finger actuator is not enough, as the stable and robust operation for a gripper requires a variety of sensors. Sensors will help the soft gripper detect whether the gripping force is appropriate and whether the grasp range should be enlarged to cover the object. As a result, efforts should be put to improve the intelligence of the cable-driven finger actuator, paving the way for soft robotic feedback controls and machine learning applications.

## CHAPTER 3: INTELLIGENT SOFT FINGER ACTUATOR

### 3.1 Objective

*The work of this chapter was published in *Advanced Materials Technologies*, 5(4): 1901075 (2020). <https://doi.org/10.1002/admt.201901075>.*

In this chapter, we aimed to develop an intelligent soft cable-driven actuator capable of fast response, accurate control, and most importantly, self-powered contact and bending detections via triboelectric nanogenerator technology, paving the way for feedback control and machine learning applications for soft cable-driven actuators. The sub-objectives were described as follows:

- Following the concept in Chapter 2, a similar cable-driven actuator was proposed, only actuated by a single cable (inward bending). And a chamber was designed close to the backside of the finger body to accommodate the soft bending sensor.
- Theory and mechanism for triboelectric nanogenerator were studied to guide the design of flexible contact and bending sensors compatible with the soft robot design.
- The silicone skin patch was designed to impart the soft finger with the highly sensitive pressure detection ability. Fabrication steps were investigated in detail to ensure quality, and experiments were conducted to calibrate its pressure sensing behaviors.
- The soft bending sensor consisting of two strips was designed and embedded in the soft finger, to perceive the size and shape of contacting object. Experiments were performed to calibrate its curvature sensing behaviors.

### 3.2 Method

#### 3.2.1 Structure Design of Smart Finger Actuator

The body of the cable-driven finger actuator was made of silicon rubber and split into four segments by three 45° triangular cuts (with a similar design as that in Chapter 2), so as to facilitate

its inward bending, achieve a better enveloping profile, and thus conformal contact with the objects possessing complex geometries (Figure 25). To simplify the structure and focus on the intelligence enhancement for the soft cable-driven actuator, only a single cable was deployed through the robot body, close to the bending side (inward bending), with one end connected to a miniature DC motor, and the other end fixed to the soft fingertip. In addition, a rectangular chamber close to the opposite side of the actuator was designed to accommodate the flexible bending sensor, and further facilitate the bending motions of the soft finger. In order to protect the rubber materials of the finger actuator and to reduce the potential friction, small plastic tube segments were bonded around the surface of the holes inside each phalanx correspondingly. The dimensions of the soft finger body were shown in Figure 26a.

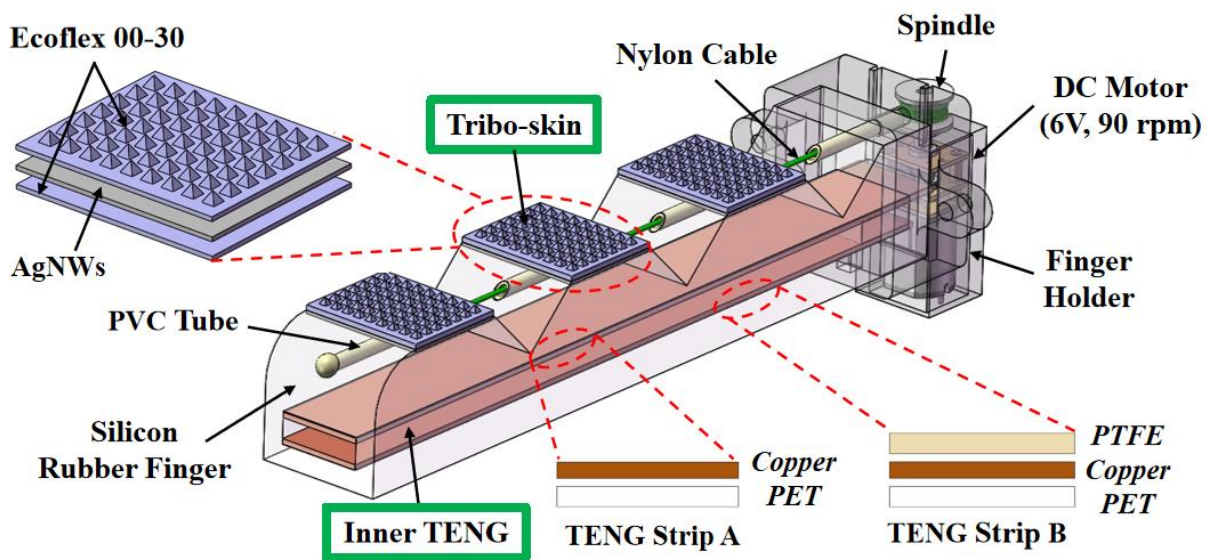


Figure 25. Structure design of the smart soft actuator equipped with tribo-skins and inner TENG.

To make the soft finger actuator intelligent (i.e., capable of perceiving the environment and conveying response), the technology of triboelectric nanogenerator was used due to its wide range of material selections and outstanding signal outputs. For full integration with the soft finger frame, a soft skin-like TENG patch which consisted of two silicone rubber layers sandwiching a layer of

silver nanowires (AgNWs) as electrode was developed, named tribo-skin. The tribo-skin would be attached onto the phalanges of the soft actuator and could generate electricity when contacts occur (the fundamental theory for TENG to generate electrical outputs will be discussed in Section 3.2.3). Due to the variation of output voltage under various forces, the tribo-skin could serve as a pressure sensor for the finger actuator. And to enhance its sensitivity and output performances, micropattern features were applied to the top surface of the silicone patch. It had been validated that the output efficiency of the patch-like TENG ranks as: pyramid (5~6 times higher than that of an unstructured film) > cube > line.<sup>[99]</sup> Such great improvement was due to the following reasons: (1) significantly improved capacitance changes of the TENG due to the air voids formed by surface feature and the enhancement in effective dielectric constant; (2) more evident triboelectric effect owing to a more sophisticated surface, thus inducing more surface charges during friction; (3) easier separation for the triboelectric charges on micro-structured surfaces, resulting in a larger dipole moment between electrodes. The dimensions of the soft skin patch were illustrated in Figure 26b.

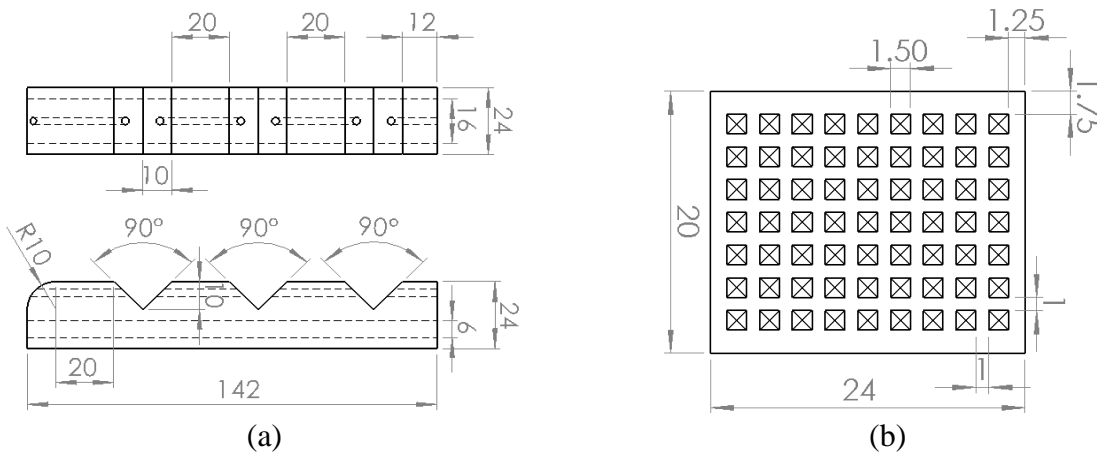


Figure 26. Dimensions of the soft finger body and tribo-skin patch.

Besides the array of tribo-skins attached onto the phalanx of the soft actuator, another TENG unit was embedded into the soft finger chamber to serve as the curvature sensor. This inner TENG device consisted of two separate strip structures: Strip-A connected to the actuator holder with its

tip end, while Strip-B entirely bonded to the chamber surface. When the finger actuator bent, Strip-A was free from the deformation of the finger because of the boundary condition mentioned before, while Strip-B could curve together with the soft body and then get in touch with Strip-A, resulting in a touched bending of Strip-A. Further bending of the soft finger actuator would lead to a larger contact area between the strips, which in turn produced more electricity due to triboelectrification effect. The voltage signals from these two kinds of TENG devices could be utilized to monitor and record the statuses of the finger actuator in different applications, like contact force, bending angle, shape profiles, and relative weights of contacting objects. The components for assembling the soft smart finger actuator were described in Figure 27a. And the soft actuator based on the modular design could be assembled into a gripper apparatus (Figure 27b) with various grasping scopes, to overcome the drawback induced by single cable pulling (i.e., outward bending of the finger actuator not allowed).

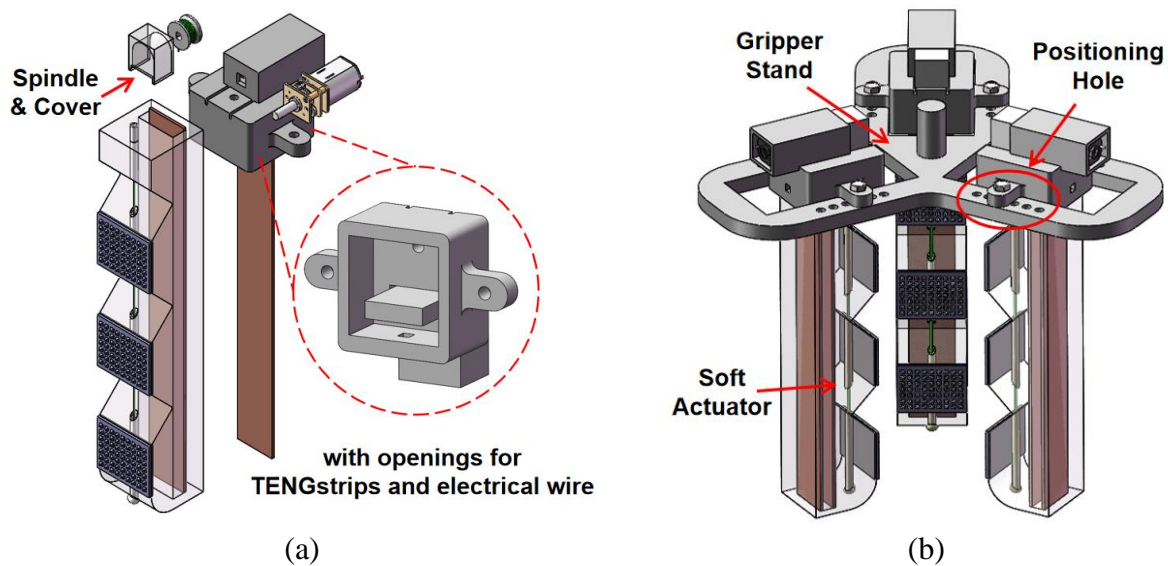
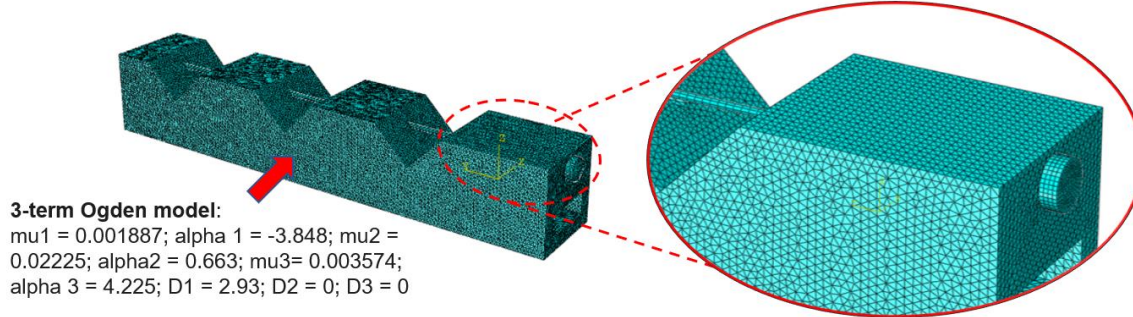


Figure 27. Assembled soft gripper based on modular design. (a) Components of the smart finger actuator and (b) an assembled gripper device.

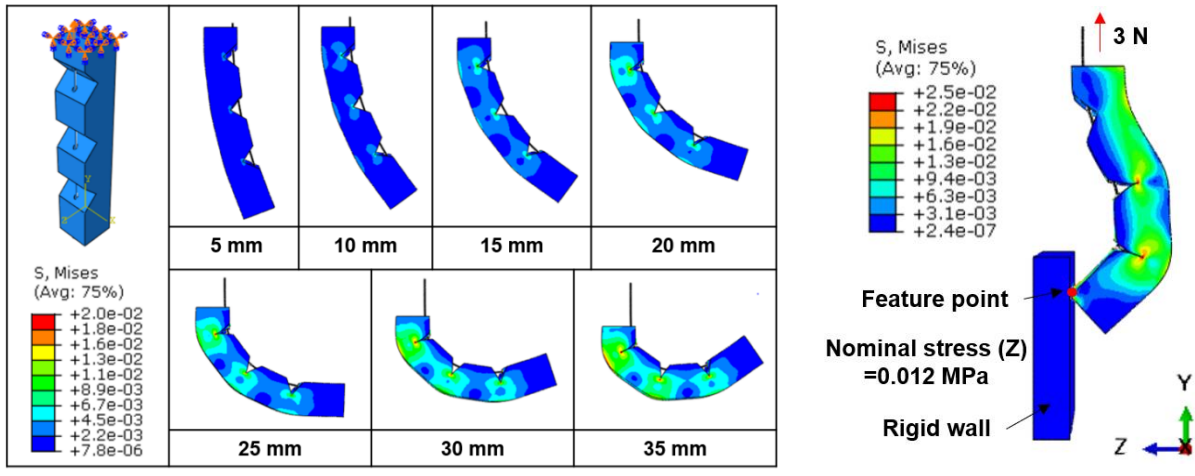
### 3.2.2 Finite Element Analysis for Actuator Body

As the mainframe, the mechanical behaviors of the soft finger actuator were investigated at

first, which was directly related to the grasping capacity of the assembled gripper. The deformation of the soft finger actuator was further modeled by nonlinear FEM with the software, Abaqus 6.14. 4-node tetrahedral element was utilized to discretize the soft finger body, cable, and cable fixture, as shown in Figure 28a. The constraint (tie type) between the cable and cable fixture, and the self-contact of notches and surface-to-surface contact between holes and cable were established. To be specific, tangential contact behavior was modeled by penalty method with the friction coefficient of 0.6. Normal contact behavior was modeled as ‘hard’ contact. The Ogden constitutive model was utilized to fit the property of Ecoflex 00-30 with parameters:  $\mu_1=0.001887$ ;  $\alpha_1=-3.848$ ;  $\mu_2=0.02225$ ;  $\alpha_2=0.663$ ;  $\mu_3=0.003574$ ;  $\alpha_3=4.225$ ;  $D_1=2.93$ ;  $D_2=0$ ;  $D_3=0$ .<sup>[100]</sup> The top of the actuator was clamped while a displacement loading was vertically applied to the tip of the cable to actuate finger bending. Detailed modeling setup was described in Section 2.2.2. As shown in Figure 28b, when the cable was gradually pulled up, the finger would keep bending inward due to the squeezing of the notches between the phalanges. In addition, a higher solution for the stress distributions and concentrations of the soft finger were chosen for a better prediction of its mechanical performances, as well as the contacting force induced from the fingertip of the actuator (Figure 28c). The chamber designed at the backside of the soft body could also facilitate the flex of the actuator, resulting from the reduced bending stiffness due to the removal of materials. As could be seen from Figure 28d, under a cable displacement of 30 mm, the soft finger actuator without the chamber structure induced a fingertip deflection of ~111 mm (in upward direction), while the finger with chamber close to its back could be deformed with a tip displacement of 117 mm.

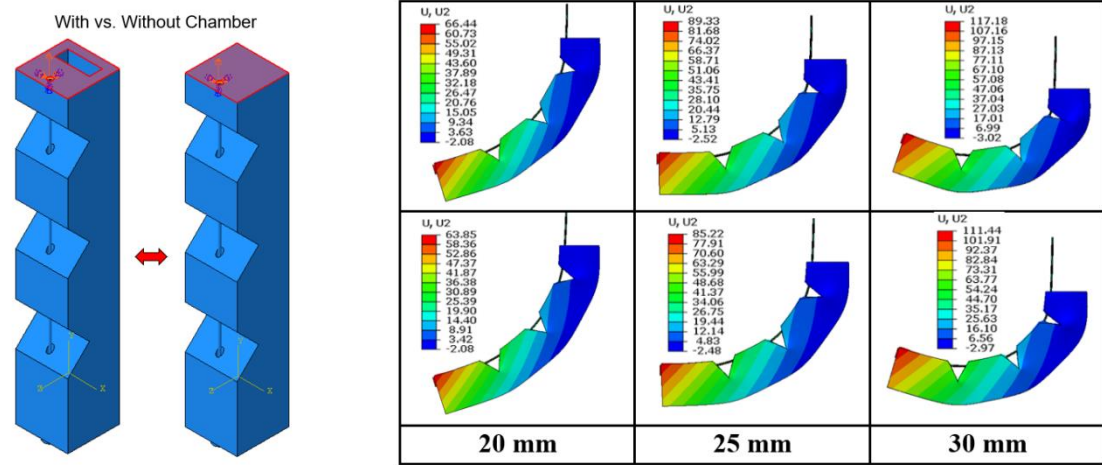


(a)



(b)

(c)



(d)

Figure 28. Finite element analysis for the soft finger actuator. (a) Meshes and material properties of soft actuator. (b) FEM results of the soft finger induced from cable pulling. (c) FEM results of the soft actuator via applying equivalent force on its tip. (d) FEM result of contact force from fingertip.

### ***3.2.3 Theory and Simulation of TENG Device***

A TENG is typically designed via different combinations of material pairs that are different in electron affinities. The electron affinity of material represents the easiness of attracting/donating the electrons. As a result, a pairing of materials which are far apart in the triboelectric series should be chosen to enhance electrical outputs for the TENG device.<sup>[101]</sup> TENGs have three basic working modes, including contact, sliding, and single-electrode (Figure 29). In a contact-separation mode, opposite charges will be generated on the surfaces of two materials with different electron affinities, when they get into contact with each other. Upon separation under external forces, a gap, and thus an electric potential will be induced in interfacial regions, driving electrons to flow via an external circuit to maintain the electrostatic balance. And the induced triboelectric charges vanish when the two materials contact again, resulting in a flow back of electrons. As for the TENG in sliding mode, it has a similar configuration to that in contact mode, inducing a circuit current when two materials slide relatively. Based on the electrical structure, both the sliding mode and contact mode utilize a pair of interconnected electrodes with a relative displacement, which would limit their applications as there are always a pair of wires connected to the external circuit. As a result, the single-electrode mode of TENG is employed where the (dielectric) material can be freely movable without electric connection. The single-electrode TENG can be operated in both the contact mode and sliding mode but with low electrical outputs. When a dielectric material (e.g., skin) approaches and departs from the pairing electrode following different routes, the triboelectric charges will transfer between the electrode and the ground. We could take advantage of the features of the TENG in single-electrode mode to develop tactile sensors for soft robot applications, so that the targeting object did not need any electric connection.

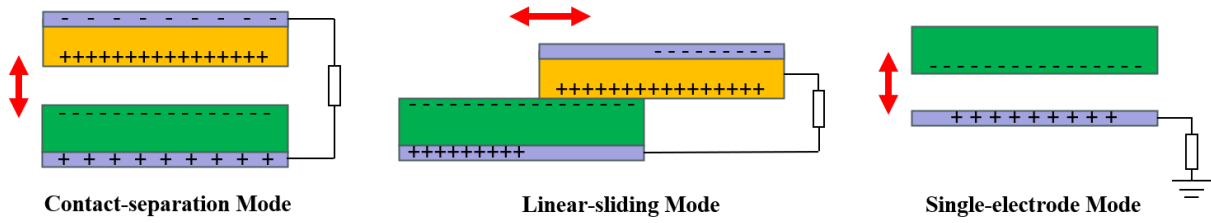
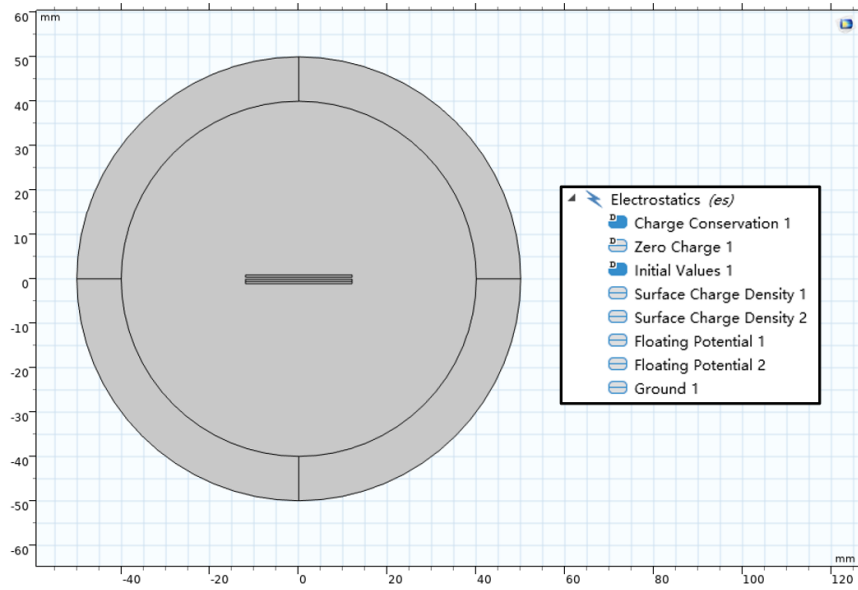
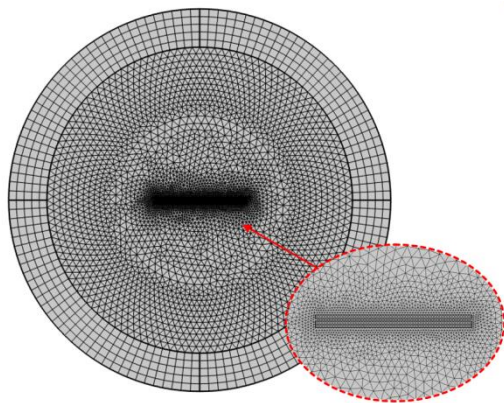


Figure 29. Typical working modes for TENG devices.

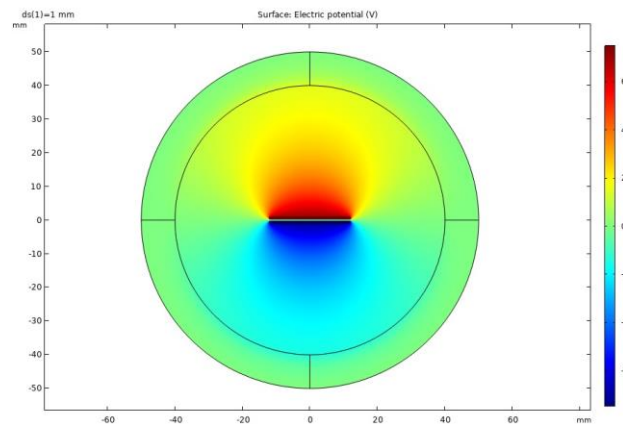
As for evaluation of the electrical performance of TENG device, the parallel-plate capacitor model is usually adopted to establish the numerical solution due to its inherent capacitive property. However, the following simplification and assumption should be made in advance: (a) the charges generated are distributed evenly on surfaces of dielectric materials and electrodes; (b) components parallel to the plate forming the capacitor are ignored and only the electric field vertical to the plate is considered. The  $V$ - $Q$ - $x$  relationship of TENG, where  $V$  represents the output voltage,  $Q$  denotes the amount of induced charges between the electrodes, and  $x$  represents the separation distance of the pairing components, is used to reveal its electrical behaviors. The potential difference between the electrodes of a TENG consists of two parts, including the contribution of polarized triboelectric charges to the voltage, i.e.,  $V_{OC}(x)$ , which is dependent on the separation displacement  $x$ , and the contribution of the already transferred charges  $Q$  to the potential difference, i.e.,  $-Q/C(x)$ , where  $C$  denotes the capacitance between electrodes, which changes according to the relative displacement. Considering TENG a typical capacitor, then its total voltage difference can be given as  $V=V_{OC}(x)-Q/C(x)$ .



(a)



(b)



(c)

Figure 30. Finite element analysis for the TENG in the contact mode. (a) Simulation model and setup via electrostatics module. (b) Meshing for the TENG. (c) Simulated potential distribution when the two materials are in close contact.

Finite element analysis is often used to calculate potential distributions between electrodes of a TENG via COMSOL Multiphysics, under open-circuit conditions. As the tribo-skin and inner TENG proposed in this study were based on a similar working mechanism, a contact-mode TENG was simulated here to simplify the modelling. Here, the 2D dimension was utilized to establish the simulation model, with a combined PTFE/Copper layer (length, 24 mm; each thickness, 0.5 mm), and a copper layer (length, 24 mm; thickness, 0.5 mm). And a circular area was designed to assign

the infinite element domain with material property of air, covering the material pair of the system. To apply the boundary condition, the surface charge density at contact surfaces of the material pair were assigned as  $\pm 1e-7 \text{ C}\cdot\text{m}^{-2}$  (positive for the upper layer, while negative for the bottom electrode due to the electrostatic induction of tribo-charges). And floating potentials were set 0 for the outer surfaces of the materials. Finally, the ground feature was applied to the outer rim of the circular structure (Figure 30a). The meshing of the entire TENG system was described in Figure 30b with finer mesh quality near the center. The simulation result of the potential distribution of the TENG with its pair of materials in close contact with each other was shown in Figure 30c.

### 3.2.4 Fabrication of Soft Finger Body

Figure 31 depicted the fabrication steps of the main body of the smart soft actuator. Briefly, the soft finger was mold-casted by pouring well-mixed Ecoflex 00-30 (Smooth-on Inc., USA) with a weight ratio of 1:1 for parts A and B into a 3D-printed mold (plastic tube inserted for a coherent hole to deploy the cable, as discussed before). Then the mold with liquid matter would be cured at 80 °C for 2 h in an oven. After curing, the soft finger was demolded and embedded with PVC tubes for deploying the nylon cable. Detailed fabrication steps were described in Section 2.2.3.

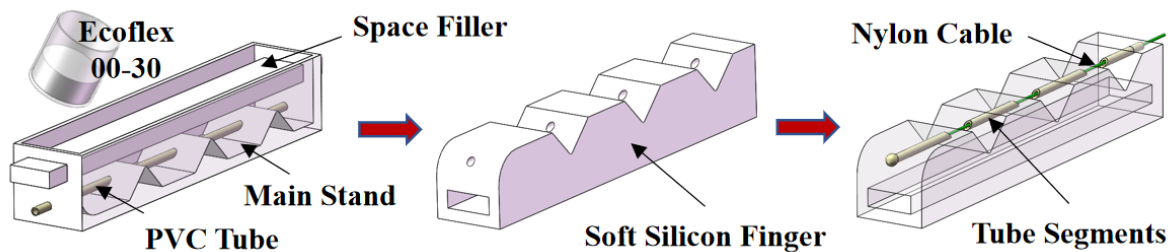


Figure 31. Fabrication processes for the soft finger actuator with backside chamber.

### 3.2.5 Fabrication of Compliant TENG Sensors

The inner TENG was fabricated by bonding a copper tape onto a PET film to make Strip-A and then attaching a PTFE film layer onto the top of the copper layer bonded with PET film to

form Strip-B. The compliant tribo-skin patches were also fabricated using the mold casting method (Figure 32) with the same material adopted for making the soft finger. After curing, the patterned patch was peeled off from the mold for later use. To apply an electrode layer on the rubber surface robustly, a dry transfer method was utilized for coating silver nanowires (AgNWs). To be specific, a glass slide covered with a PTFE film was first prepared for spraying AgNW solutions, and then a thin layer of silicone rubber was applied on its top. After curing, AgNWs could be dry-transferred onto this silicon-rubber layer. Finally, the patterned rubber surface made before could be bonded onto it with a wire inserted for conducting electricity.

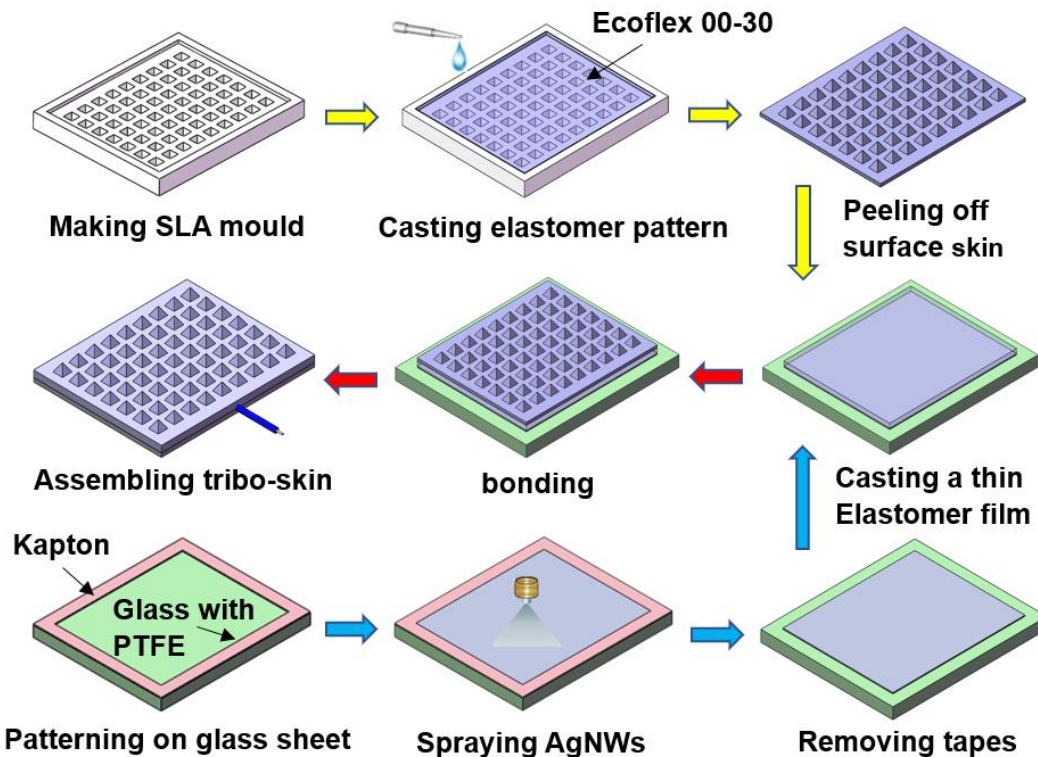


Figure 32. Fabrication procedure for the silicone tribo-skin patch.

### 3.2.6 Experimental Setup for TENG Device

To evaluate the sensing abilities of the soft tribo-skin under diversified working conditions, we combined a force gauge with a linear motor (LinMot MBT-37×120), as depicted in Figure 33. A glass slide was bonded onto the tip of the force gauge to allow full-face contact. The linear motor

which can be precisely controlled in terms of speed, acceleration, and displacement amplitude was utilized to impact the skin periodically. Output voltages, currents and transferred charges generated by TENGs could be measured by a current preamplifier (Keithley 6514 System Electrometer), and then be collected as real-time data via the software LabVIEW. For tribo-skins, we mainly focused on the test to reveal their sensing behaviors with different contacting force, frequency, and material. On the other hand, to characterize the ability of inner TENG, we measured the relationship between the open-circuit voltage induced by the TENG strips and the bending angles of the finger actuator. The motor equipped with an encoder was controlled using Arduino UNO to perform the two-way rotation with specific angular displacement. Upon testing, the motor was programmed to rotate by a degree (i.e.,  $60^\circ$ ,  $120^\circ$ ,  $180^\circ \dots 600^\circ$ ) and then get back immediately. The voltage generated from the inner TENG was recorded with the assistance of Keithley 6514 Electrometer and LabVIEW as well.

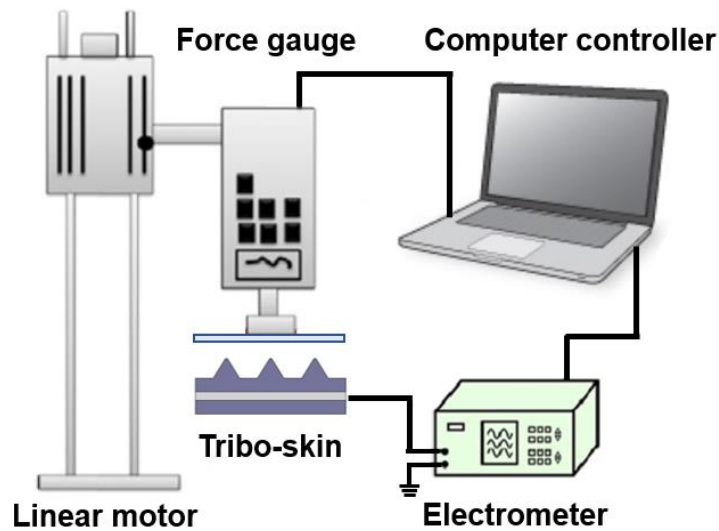


Figure 33. Experimental setup for testing electrical performances of the flexible TENG devices.

### 3.3 Result

#### 3.3.1 Illustration of As-Fabricated Smart Soft Finger Actuator

The as-fabricated major components for the smart finger actuator were illustrated in Figure

34a, including the finger body made of silicone rubber, TENG strips, and silicone tribo-skins. The soft actuator possessed an overall dimension of 142×24×24 mm and the thickness of the tribo-skin is 0.5 mm. After inserting the nylon cable with its ends fixed at the fingertip and the spindle of DC motor respectively, the tribo-skins and TENG strips were installed onto the surfaces of the actuator as discussed before. An assembled soft finger actuator based on the modular design was illustrated in Figure 34b.

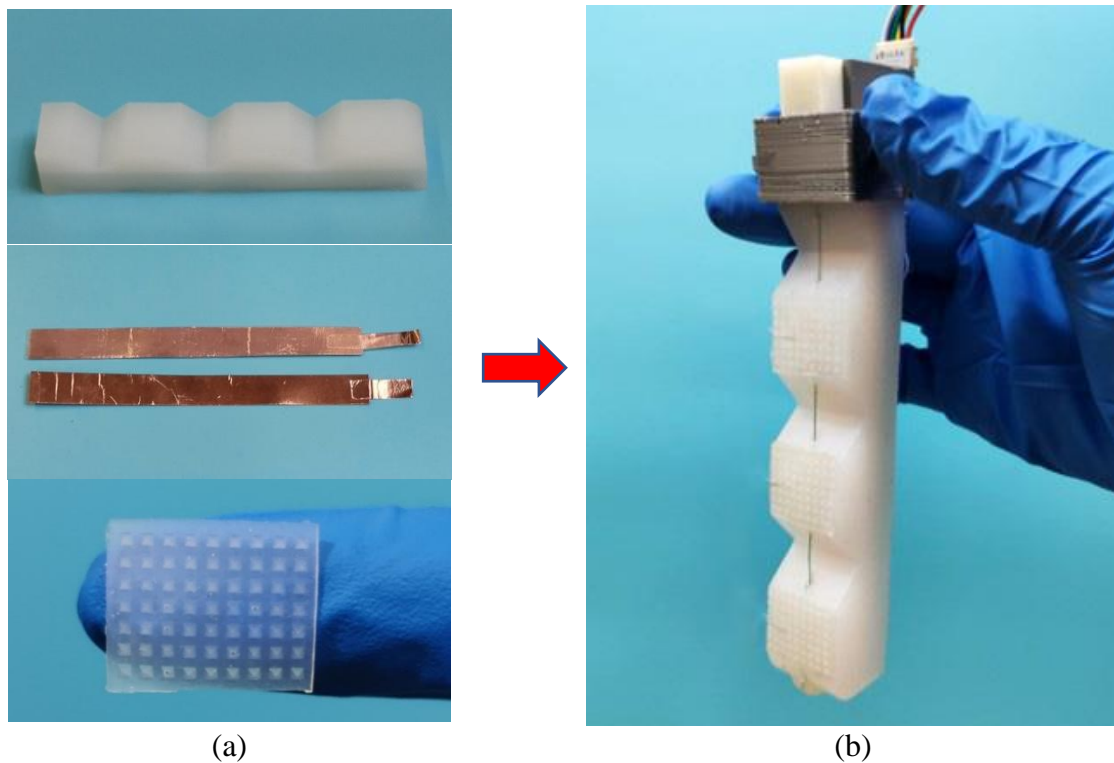


Figure 34. Assembled smart finger actuator with its components. (a) Fabricated components for the finger actuator. (b) An assembled smart finger actuator.

The top-view (captured by an electron microscopy) of the micro-pyramid feature patterned on the silicone tribo-skin, and the AgNWs (through scanning electron microscopy) evenly sprayed inside the skin layer were illustrated in Figure 35.

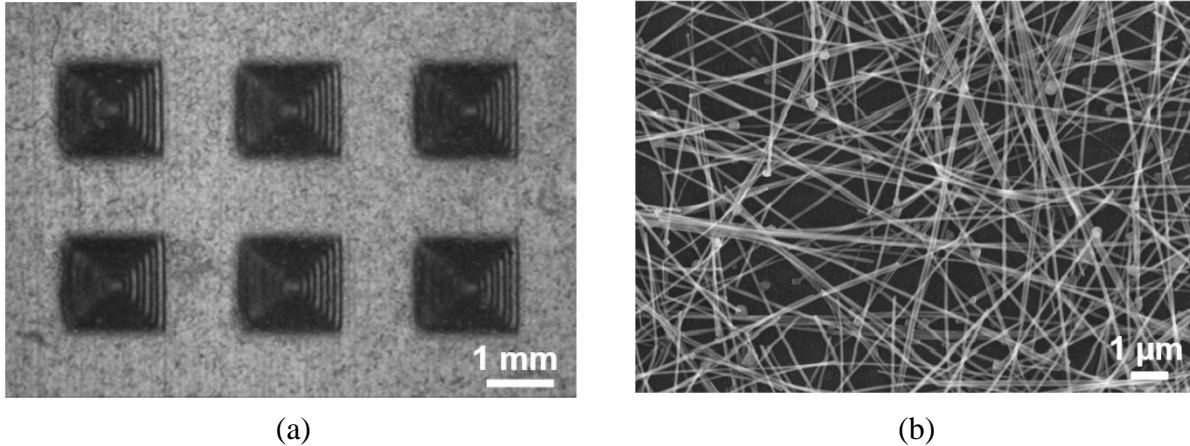


Figure 35. Illustration of the as-fabricated tribo-skin and sprayed AgNWs. (a) Photography of the surface feature of tribo-skin. (b) SEM view of AgNWs.

### 3.3.2 Performance Characterization of Tribo-skin (Force Sensor)

The working principle of the tribo-skin based on single-electrode mode was illustrated in Figure 36a. When the dielectric object (i.e., glass slide) approached the tribo-skin, electrons would be inducted from the ground to the AgNW electrode due to electrostatic induction effect, producing electrical currents in the circuit. When the object came into contact with the tribo-skin, the charge neutralization would happen, and the electrons would stop moving. When two oppositely charged surfaces were separated, the potential difference between the electrode and ground was generated, prompting the flow of electrons, and generating electrical current in the circuit. When the contacted subject was quite far away from the tribo-skin, a new electrical equilibrium would be established. Due to the micro-pattern feature on the top surface of the tribo-skin, its voltage output performance would be greatly enhanced, along with its sensitivity of pressure detection, as discussed in Section 3.2.1.

Tribo-skin could serve as a force or pressure sensor, after the calibration between the open-circuit voltage and the amplitude of applied force were made. Figure 36b-d recorded the real-time signals (voltage, current and charge) induced by the as-fabricated tribo-skin under the contact force

with a magnitude of 8 N and a frequency of 1 Hz. It was found the open-circuit voltage achieved a peak voltage of ~23 V in average (current ~50-60 nA and transferred charge ~7.5 nC). When the contact force with a frequency of 1 Hz increased from 2 to 10 N with increments of 1 V, the open-circuit voltage was enhanced from 4.8 to 41 V (Figure 36e). However, further increase in contact force (>10 N) would not alter the output anymore, indicating the detecting scope. Figure 36f was a calibration curve fitted with the data of the peak voltage and force amplitude. Due to the micro-pyramid pattern on the soft tribo-skin, the voltage showed a nonlinear relationship with the applied contact force. Contact frequency and contact material were two other factors that could affect the outputs of the tribo-skin. Figure 36g showed the peak open-circuit voltage as a function of contact frequency under an applied force of 7 N. It was noticed the peak voltage value could be increased from 18.7 V to 23.6 V as the frequency increased from 0.3 Hz to 2.2 Hz. As shown in Figure 36h, the voltage output varied with the types of contacting materials. Human skin, glass and paper could generate higher output under contacts of 5 N and 1 Hz. And the robustness of the tribo-skin under repeated contacts (1 Hz) was verified in Figure 36i with stable peak output within 1000 times of contact cycles.

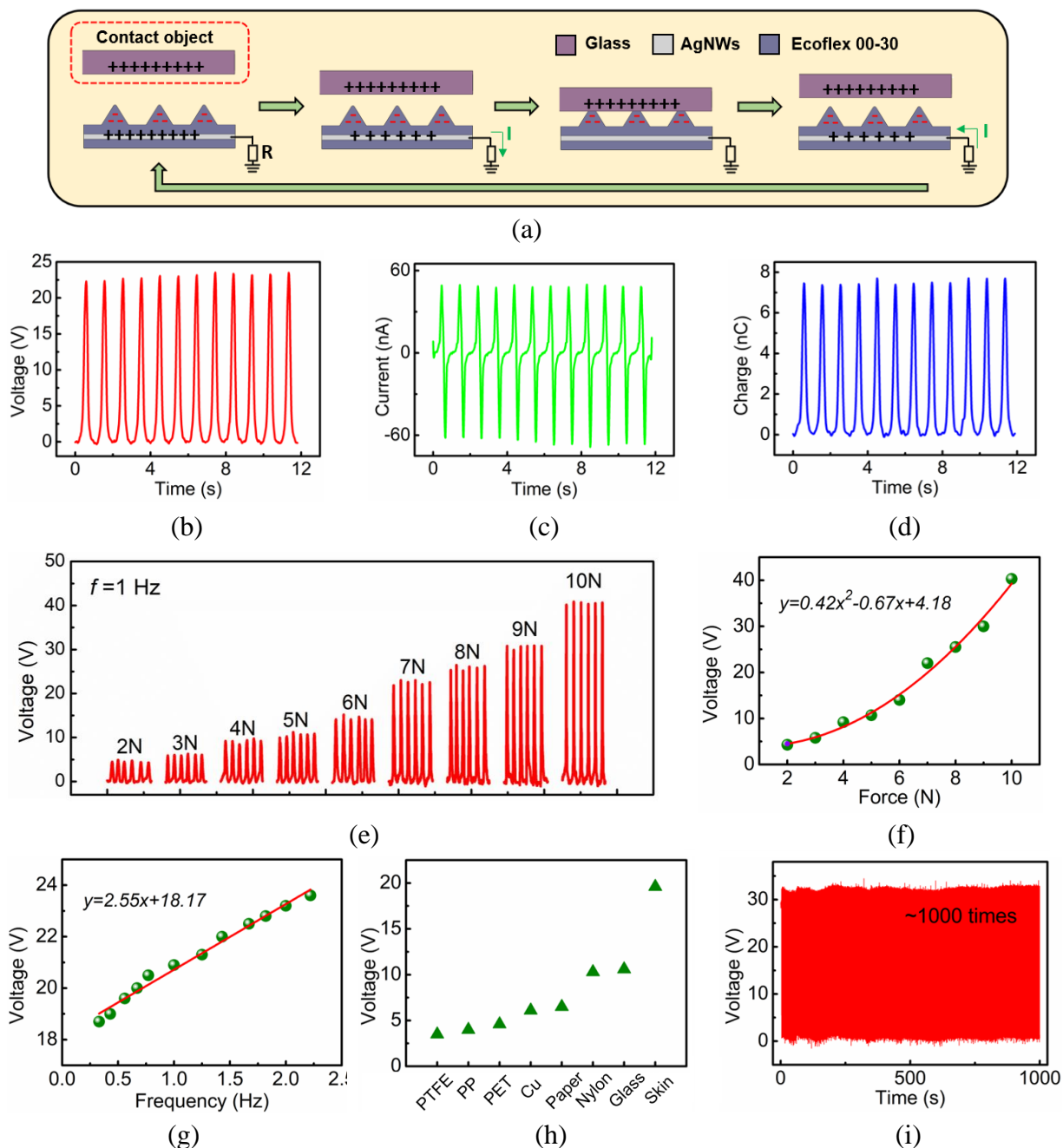


Figure 36. Mechanism and performance characterization of the tribo-skin. (a) Principle of the tribo-skin in single-electrode mode. (b) Open-circuit voltage, (c) Current and (d) Transferred charge induced from the tribo-skin under a cyclic compression force of 8 N (1 Hz). (e) Open-circuit voltages from the tribo-skin patch under different applied forces (1 Hz). (f) Fitted curve for the peak voltage as a function of force (1 Hz). (g) Effect of the contacting frequency on output of the tribo-skin under a force of 7 N. (h) Output performance of the tribo-skin affected by types of materials. (i) Robustness of the as-fabricated tribo-skin with ~1000 contact cycles.

### ***3.3.3 Performance Characterization of Inner TENG (Curvature Sensor)***

The inner TENG with 2 strips embedded in the chamber the soft finger actuator worked on the contact-separation mode (Figure 37a). The two strips, Strip-A fixed to the printed holder and Strip-B bonded to the chamber surface, would get into contact with each other when the soft finger actuator bent under actuation. Since the two strips had various boundary conditions, Strip-B would deform together with the finger, sharing the same bending degree. The contact area would increase with further bending of the actuator, making the Strip-A with copper positively charged and Strip-B with PTFE negatively charged according to the triboelectric theory. When the actuator returned to its original shape, the contacted surfaces separated apart with electrons flowing from Strip-A to Strip-B to neutralize the positive charges triggered by triboelectricity. Electrons kept flowing until the finger actuator turned straight. When the actuator was bent again, an inverse electron flow was generated between the TENG strips. The open-circuit voltage vs. the corresponding rotation angles of the motor was described in Figure 37b. With the constant rotation speed of the motor, bending the actuator to a larger angle required a longer time, which was observed from the increased wave width of the voltage pulse towards the right end of Figure 37b. Meanwhile, it could be seen that a larger curvature of the actuator generated a higher voltage magnitude, indicating that the voltage signal could be detected and analyzed for reporting the bending angle and bending profile. A peak voltage of 8 V could be obtained from the inner TENG when the actuator was bent when the motor rotates an angle of  $600^\circ$ . Based on the fact that the fingertip providing the largest gripping force in most cases, the angle  $\alpha$  between the intersection of the first and last phalanges of the actuator was selected to indicate finger profile and relate it with the peak output value (Figure 37c).

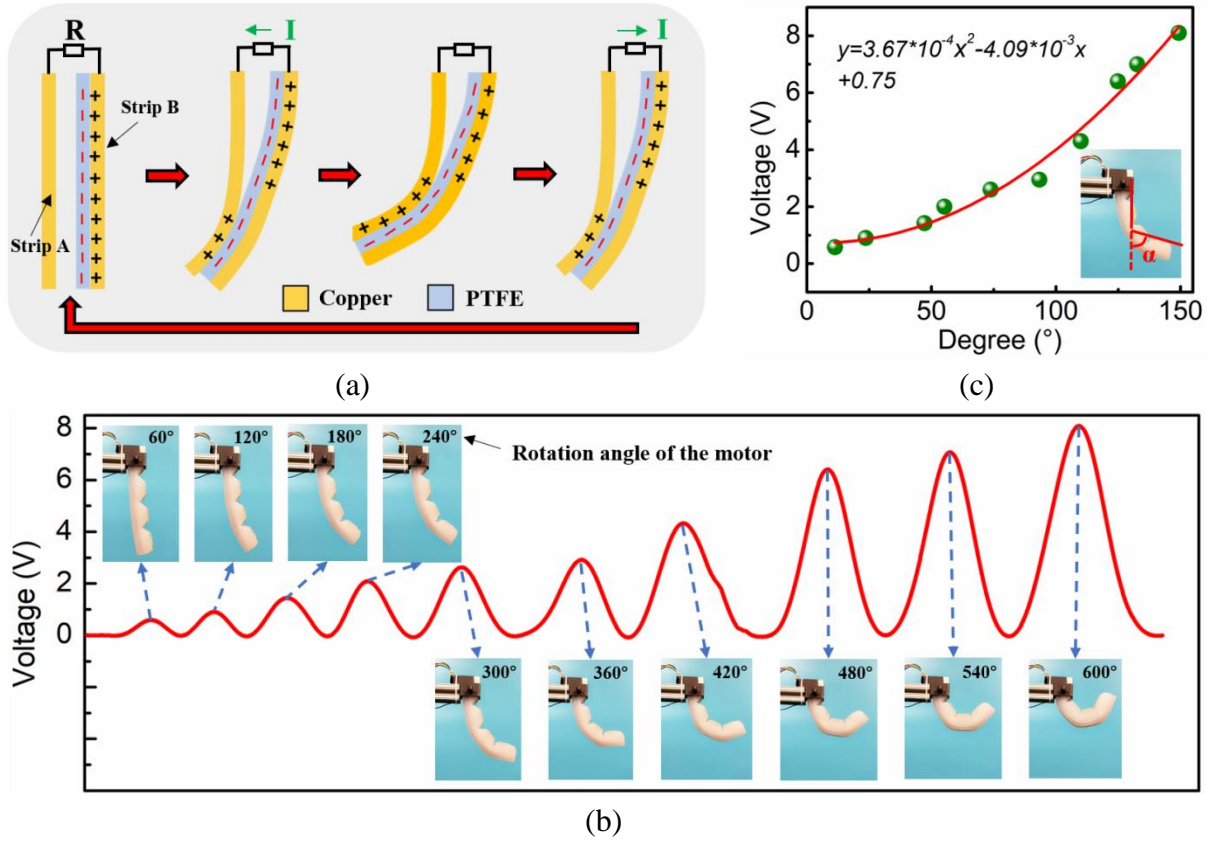


Figure 37. Mechanism and behavior characterization of the inner TENG. (a) Operation principle of the inner TENG. (b) Voltage generated by the inner TENG under different bending angles of the actuator. (c) Relationship between the peak voltage generated from the inner TENG and the bending degree of the actuator.

### 3.3.4 Performance Evaluation of Smart Soft Gripper

As illustrated in Figure 27b, a smart soft gripper could be assembled by the three soft finger actuators. Three actuators (separated at an angle of 120°) were mounted onto a printed holder with threaded holes left there for adjusting grasping scope of the soft gripper. All tribo-skins attached on the soft actuators were connected to a capacitor through a rectifier, to accumulate the electrical energy generated by the repeated gripping and separating (Figure 38a). The voltage of the capacitor (with a capacitance of 0.1  $\mu\text{F}$ ) would gradually improve and reach a value of 1.6 V after 30 s (Figure 38b). The charged capacitor could be further used as a power source to drive other sensors or electronics or batteries.

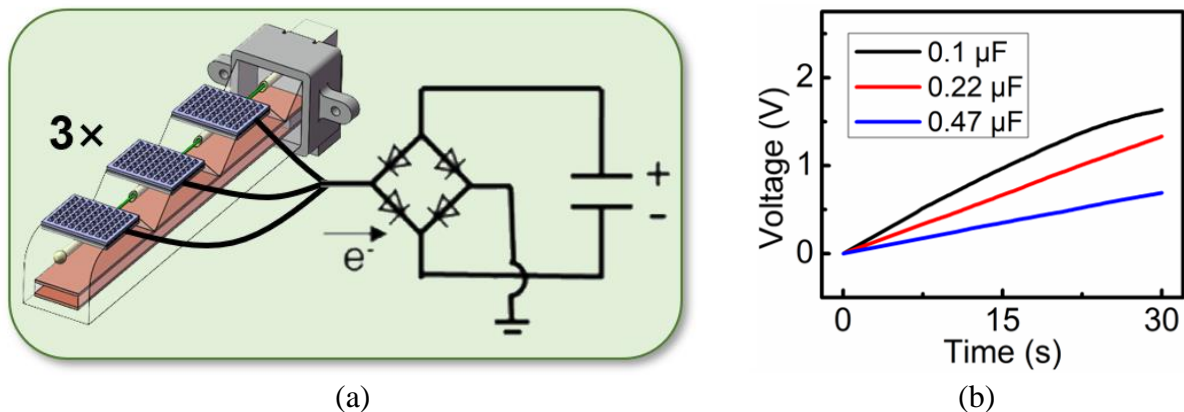


Figure 38. Energy harvesting performance for the smart gripper. (a) Circuit diagram for energy harvesting of the assembled gripper. (b) Charging process of different capacitors under repeated operations of the soft gripper.

After that, the sensing capability of the smart gripper was evaluated by grasping an acrylic ball with various weights and a PLA hexagonal prism. Due to the symmetric geometry, the voltage signals from the sensing units from only one finger actuator (three tribo-skins and one inner TENG) should be recorded. The process of grasping a plastic ball without extra weight added was shown in Figure 39a. When the soft fingers bent and approached the object, TS-2 would first contact the ball, followed by TS-1, and finally TS-3, and TS-2 and 3 offered larger forces, which was reflected by the real-time signals from tribo-skins. When the areas attached with tribo-skins kept squeezing the object further, the signals would achieve maximum values, and after that, the signals became almost constant during grasping and holding stages. In addition, it was found that when TS-3 fully got in touch with the ball, TS-1 would no longer provide support force, which was revealed by the vanished signal. A possible reason was the last phalanx lifted the object and pushed it against the gripper's stand, leaving a gap between the object and TS-1. When the gripper dropped the ball, the voltages induced from TS-2 and 3 vanished quickly, indicating separations between the object and the tribo-skins (while secondary impact might cause some tiny peak signals). A heavier plastic ball did not change the contact sequence of tribo-skins (Figure 39b), but the fingertip (TS-3) played a

more important role in lifting and grasping this heavier object with its peak output increasing to ~6 V. In addition, the voltage from TS-2 became smaller while gripping and holding this heavier object. Real-time signal from the inner TENG was also plotted as the inset. When the soft actuator curved to grab and hold the ball, the voltage achieved its maximum (~2 V), and the falling of the object would trigger a small signal due to the secondary impact as well.

Then a hexagonal prism grasped by the smart gripper was shown in Figure 39c. Due to the difference in shape, the contact sequence for the tribo-skins would turn to TS-1 > TS-2 > TS-3. In addition, due to the smaller bottom of the prism, TS-3 only touched the bottom edge of this object, thus the voltage signal became smaller and sharp during grasping and holding, with a peak voltage of ~1.2 V. The signal from the inner TENG gave a peak voltage of 1.1 V, and by comparing the bending angles of the soft gripper to grip the two different objects, it was observed that the actuator needed to bend more to wrap the ball, which corresponded to a higher output induced by the inner TENG in Figure 39b. The results proved that the actively generated signals could enable the soft gripper to perceive different actions during grasping an object and to be aware of the dropping and any following contacts from the object, indicating their promising uses in grasping monitoring and feedback control.

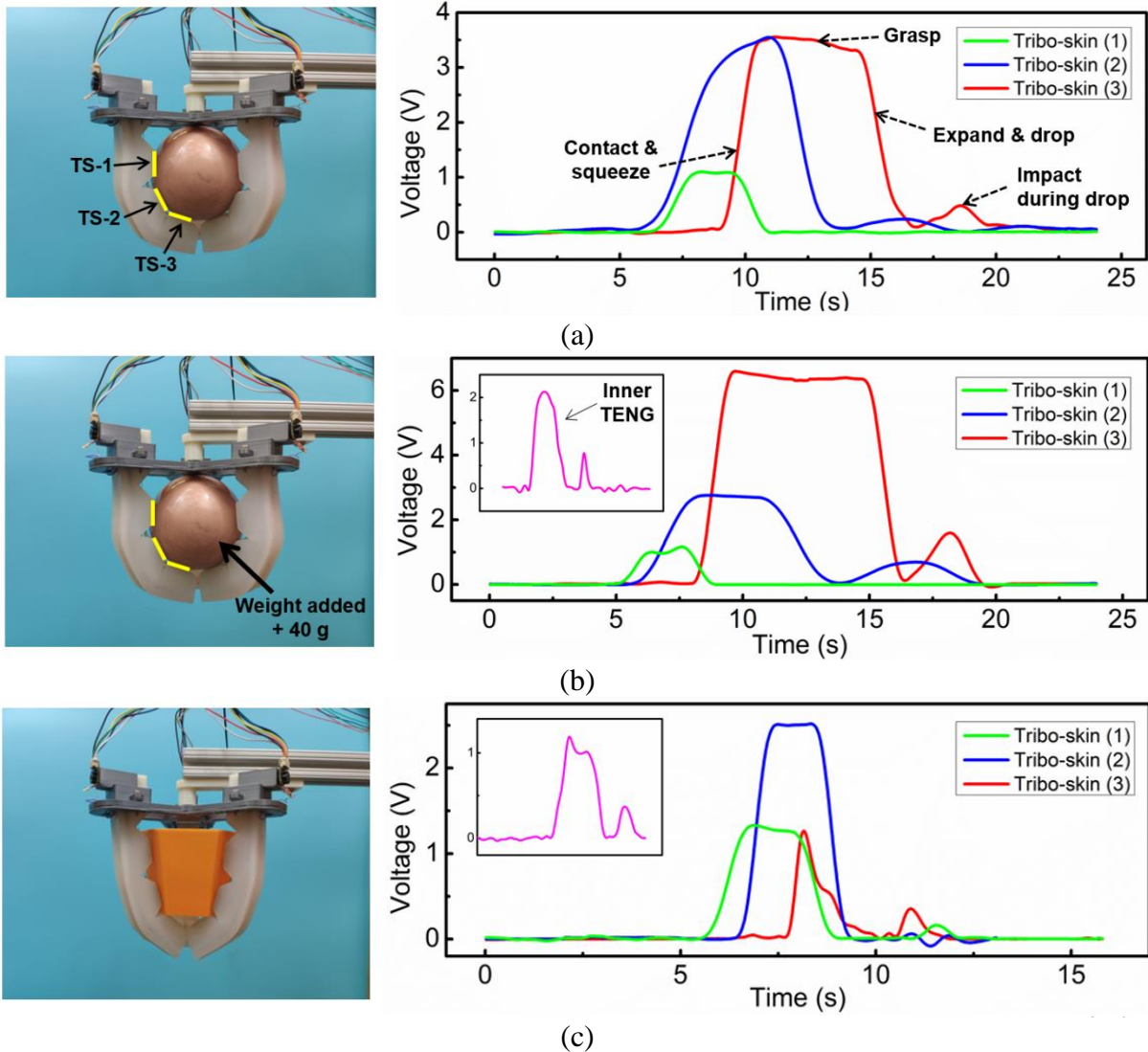


Figure 39. Evaluation of tactile sensing behaviors of the smart soft gripper. (a) Real-time voltage signals induced from all three tribo-skins when a plastic ball was grasped and dropped. (b) Real-time signals induced from tribo-skins and inner TENG when a heavier ball was manipulated. (c) Real-time signals induced from tribo-skins and inner TENG when a hexagonal plastic prism was grasped and dropped.

To enable more stable operation, we fabricated a gripper with stiffer elastomer, i.e., Dragon Skin 10 (Smooth-on Inc., USA). Figure 40 demonstrated its performances in picking and grasping tomatoes for potential agriculture harvesting applications. As the force required to pick the tomato from its stem would vary, two samples were prepared before testing. Figure 40a showed the output voltage generated by all tribo-skins (connected in series) from a single actuator. Different from the

voltage induced from a single tribo-skin (Figure 39), herein the output voltage gradually increased at the beginning until the gripper fully held the tomato. Upon a picking process, the voltage signal fluctuated obviously, leading to several smaller peaks along the curves. Comparing the two picking processes, it was concluded that picking tomato sample-1 was easier than picking tomato sample-2, indicated by the smaller voltage and the uniform and tiny peaks along the curves.

To further verify such a capability in harvesting, we used it to grasp three different tomatoes: 156 g, 180 g and 236 g (Figure 40b). The voltage signals generated by grasping were altered with the weights of tomatoes. Although the slight differences in size and shape might affect the voltage profile marginally, voltage signals during the holding stage were mainly determined by the weight of tomato. The total voltage induced by three tribo-skins in series at the grasping and holding stage for a tomato of 156 g weight is ~11 V, while for grasping a heavier one (180 g), it increased to ~20 V. And for the heaviest tomato, the output voltage increased to ~35 V. In summary, this proposed soft smart gripper was capable of detecting contact force and bending angle, and detecting possible secondary contact, picking force fluctuation and releasing/dropping phases.

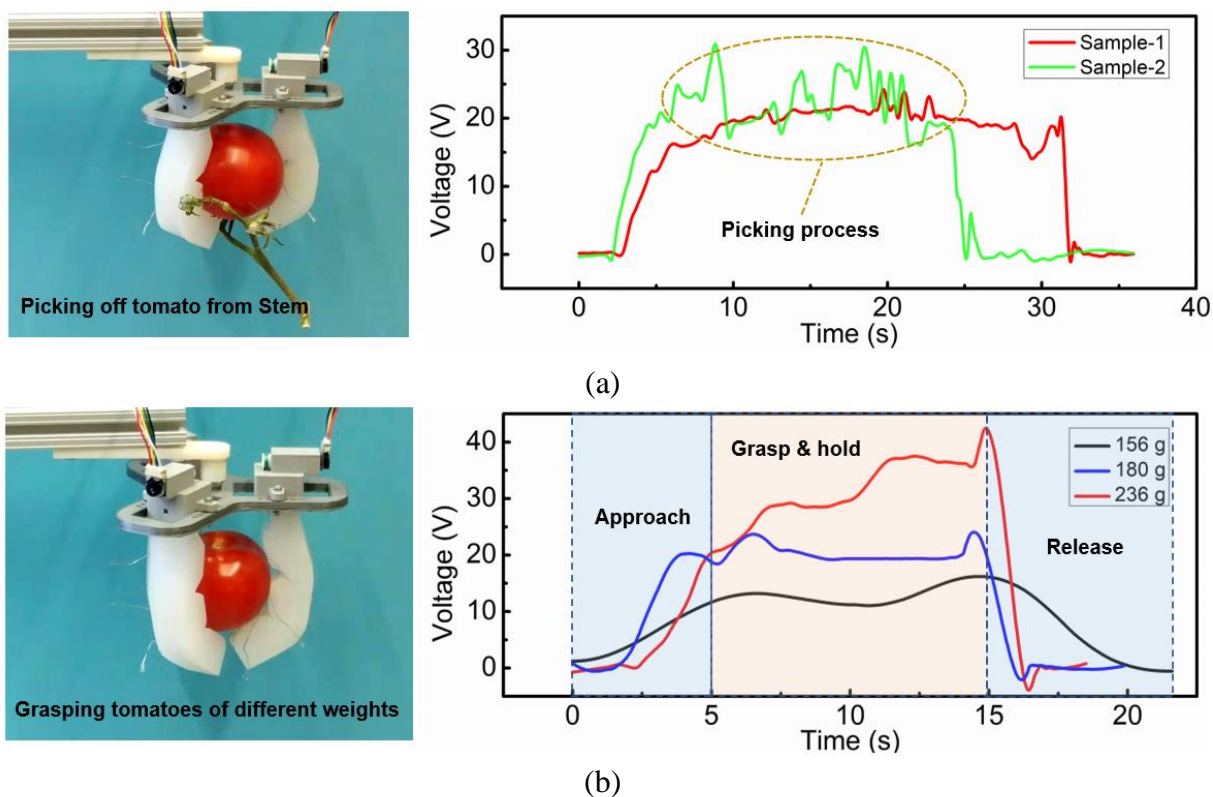


Figure 40. Perception performance of the smart gripper during tomato harvest. Real-time voltage signals induced from all tribo-skins (in series) on an actuator (a) when tomatoes were picked off from stem, and (b) when tomatoes of different weights were picked and gripped.

### 3.4 Conclusion and Discussion

In summary, we have developed a smart soft actuator with self-powered contact force and bending sensing units through the integration of soft elastomer, cable-driven principle and TENGs. Two different types of TENGs are equipped on the finger actuator: pair of inner TENG strips based on contact-separation mode that can induce voltage signals reflecting the curvature of the actuator, and tribo-skin patches patterned with micro-pyramids on surface and AgNWs stretchable electrode that can measure contact pressure through a single mode TENG design. The TENG-based sensors can be employed for monitoring the contact forces on objects, bending angles of the finger actuator and even the relative weight and rough profile of the contacting object. This finger actuator can be further assembled with a modular design strategy to form smart grippers for diverse applications.

The experiments have demonstrated that a three-fingered gripper can be used to complete different tasks, and perceive various operation stages, like approaching, grabbing, releasing, paving the way for building efficient but simple robotic manipulator for wide application. However, it is observed that the sensing performance of the tribo-skin is strongly affected by other factors, including the materials of objects, humidity, and temperature. Also, the contact area of tribo-skins may vary due to the shape variation of grasped objects, which would be challenging for calibrations. Thus, to get a reliable detection behavior, other factors should be kept constant during operation, which is not an issue in factory but would be challenging in outer spaces. One solution is to develop a new tribo-skin via contact-separation mode of TENG, which can get rid of the influences from materials and environmental factors. Furthermore, with integration with machine learning, the gripper could be capable of object recognition.

## CHAPTER 4: INTELLIGENT SOFT MANIPULATOR

### 4.1 Objective

*The work of this chapter was published in Advanced Materials Technologies, 6(5): 2100084 (2021). <https://doi.org/10.1002/admt.202100084>.*

In the chapter, an entirely soft manipulator with arm and gripper capable of dexterous shape morphing and stiffness modulation for safe human-machine-environment interaction was designed by taking advantages of cable-driven mechanism, phase transitions of low-melting-point alloy, and self-powered TENG technologies. The smart soft manipulator consisted of an omnidirectional arm, a dexterous multi-material gripper which was an improvement for the initial design, and a human-machine-interface (HMI) in the form of wearable finger patches for remote control of the soft robot. To be specific,

- A soft arm was designed to be capable of omnidirectional deformations via a minimum number of cables required, and the stiffness tuning tubes filled with low-melting-point alloy were embedded into the robotic arm structure for adjusting its overall stiffness.
- An improved soft gripper was made with bidirectional flex ability by taking advantages of flexible hinge design, so that the driving cables could be encapsulated inside the soft robotic body without hindering its bending performances.
- An entirely soft robot manipulator was designed and assembled through connecting the soft arm and soft gripper with a compliant stander structure.
- Wearable patches for human finger were designed in contact-and-separate TENG mode and could detect finger flexion. The voltage signals generated from finger bending were utilized for teleoperation of the soft manipulator, functioning as an effective HMI.

## 4.2 Method

### 4.2.1 Structure Design of Soft Arm with Adjustable Stiffness

A bioinspired soft robotic manipulator capable of bending omnidirectionally for navigation and grasping objects dextrally was depicted in Figure 41. This manipulator took advantage of the cable-driven approach, where miniature motors pulled the cables inside the robot body to squeeze the rubber materials located between cable fixture and driving motor, so as to realize deformations. Such an actuation method is attractive due to its intuitive shape morphing, and simple fabrication and control designs. This soft arm design was able to reach any point in a sphere-like workspace through a three-cable configuration, and its overall stiffness could be adjusted via phase changes of the embedded LMPA tubes under heating or cooling, in order to achieve more reliable operation (e.g., counter its own gravitational effect in some orientations and increase its grasping weight). In detail, this soft arm was mold-casted into a bellows-shaped profile using silicone rubbers, with an effective length of 200 mm and an outer diameter of 74 mm (dimensions in Figure 42), to prevent the potential buckling arising from the compression of the rubber material. A central through-hole with a diameter of 20 mm was left there to reduce the bending stiffness of the soft arm and facilitate its deformations in all directions, 3 cable holes with a diameter of 2.8 mm were uniformly allocated around a central circle with a 40 mm diameter, and another 3 holes with a larger diameter of 8 mm were placed around a central circle (diameter of 34 mm) for housing LMPA tube that adjusted the stiffness of the soft arm when needed.

Tunable stiffness of the soft robot arm was realized by heating and cooling LMPA elements in the soft body. These LMPA tubes were of the same length as the robot arm (200 mm), and under Joule-heating, the LMPAs encapsulated in the tubes would switch between the solid phase and the liquid phase, thereby altering the overall stiffness of the robot arm. The LMPA tube was fabricated

by enclosing LMPAs (Field's Metal with 16.5wt% Sn, 32.5wt% Bi, 51wt% In, melting point: 62°C) within a PVC tube. Coils were twined around the tube for applying Joule-heating. In addition, self-healing of the LMPA tubes could be ensured by pre-stretching the silicone tube during fabrication. Because of the internal stress equilibriums, the ruptured LMPA segments inside the tube would be forced to rejoin again upon heating.

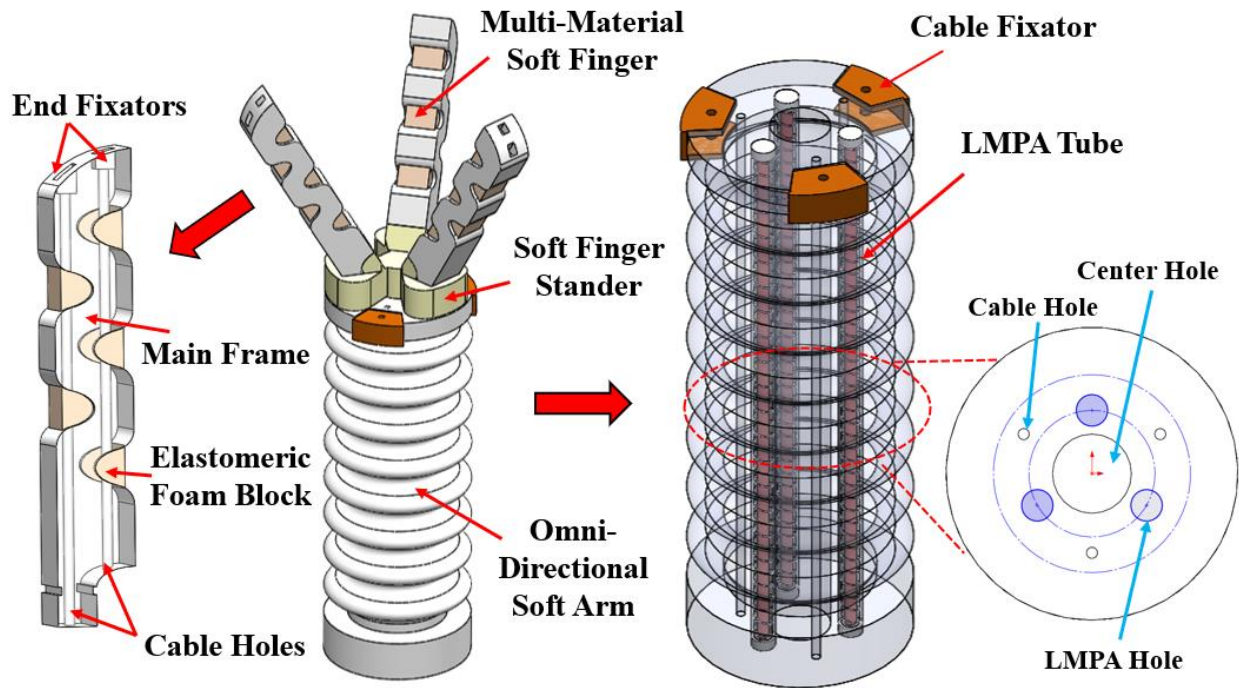


Figure 41. Structure of the soft manipulator with a soft arm capable of omnidirectional bending and stiffness variation, and a bidirectional gripper mounted on a silicone stander.

The gripper was assembled by three multi-material fingers capable of outward and inward bending, thanks to the flexible hinge structure design. Inspired by the phalanx and joint motion of human fingers, the primary frame of soft finger was constructed with interlaced semi-ellipse hinges on both sides (one more hinge on the inner side for better inward flexion performance). Such hinge structures could produce a larger bending displacement than other patterns like circular and corner-filled hinges, with the same actuation force. The main frame of the soft finger was designed with a stiffer silicone rubber material (Dragon Skin 30, smooth-on Inc., USA) to provide relatively high



Furthermore, in order to assemble an entirely soft robotic manipulator, a compliant stander structure was designed to accommodate the soft finger actuators (Figure 44). The soft stander was made of the same material employed for fabricating the main frame of the soft finger actuator. And there were cable through-holes prefabricated for the installation of each finger actuator.

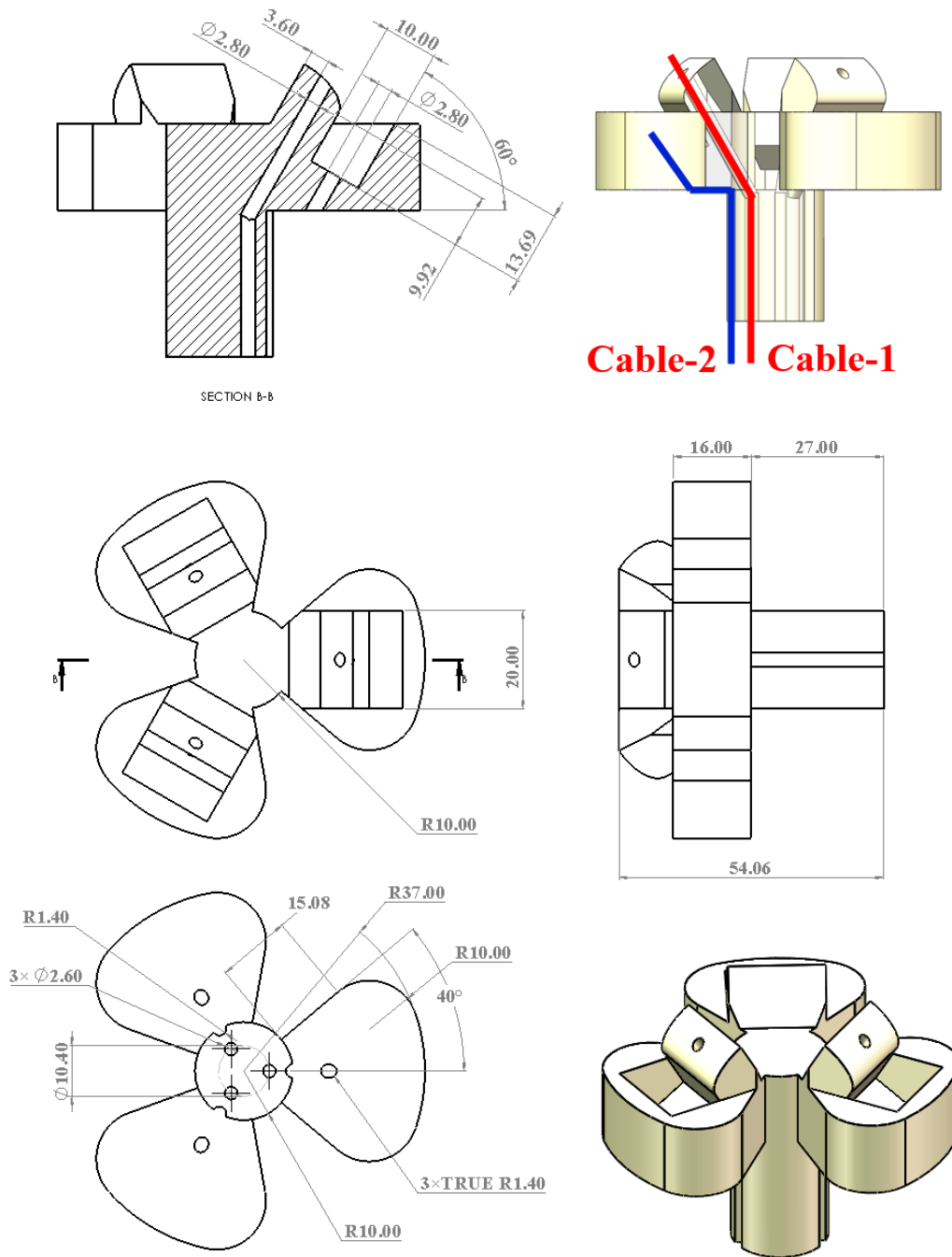


Figure 44. Structure design of the silicone stander for connection of the soft fingers and arm.

#### 4.2.2 Finite Element Analysis for Soft Manipulator

All the simulations were conducted using software Abaqus 6.14. For modeling the LMPA embedded arm, the CAD models of manipulator were discretized by 4-node tetrahedral elements. Ogden model was used to fit the mechanical properties of Ecoflex 00-30 with the same parameters in Section 2.2.2, and the stiffer material, Dragon skin 30, was also modeled utilizing Ogden model, with these parameters as:  $\mu_1=1.1806$ ;  $\alpha_1=1.0698$ ;  $\mu_2=0.8743$ ;  $\alpha_2=-1.2370$ ;  $\mu_3=-1.9396$ ;  $\alpha_3=0.1347$ ;  $D_1=0.7029$ ;  $D_2=0$ ;  $D_3=0$ .<sup>[102]</sup> To predict the bending deformation of the soft robotic arm, along with the corresponding stress distributions, under different cable-pulling displacements, the bottom part of the arm was constrained in all DOFs and a displacement was applied to the tip end of the inserted cable (Figure 45a). The detailed simulation procedures could be found in Section 2.2.2.

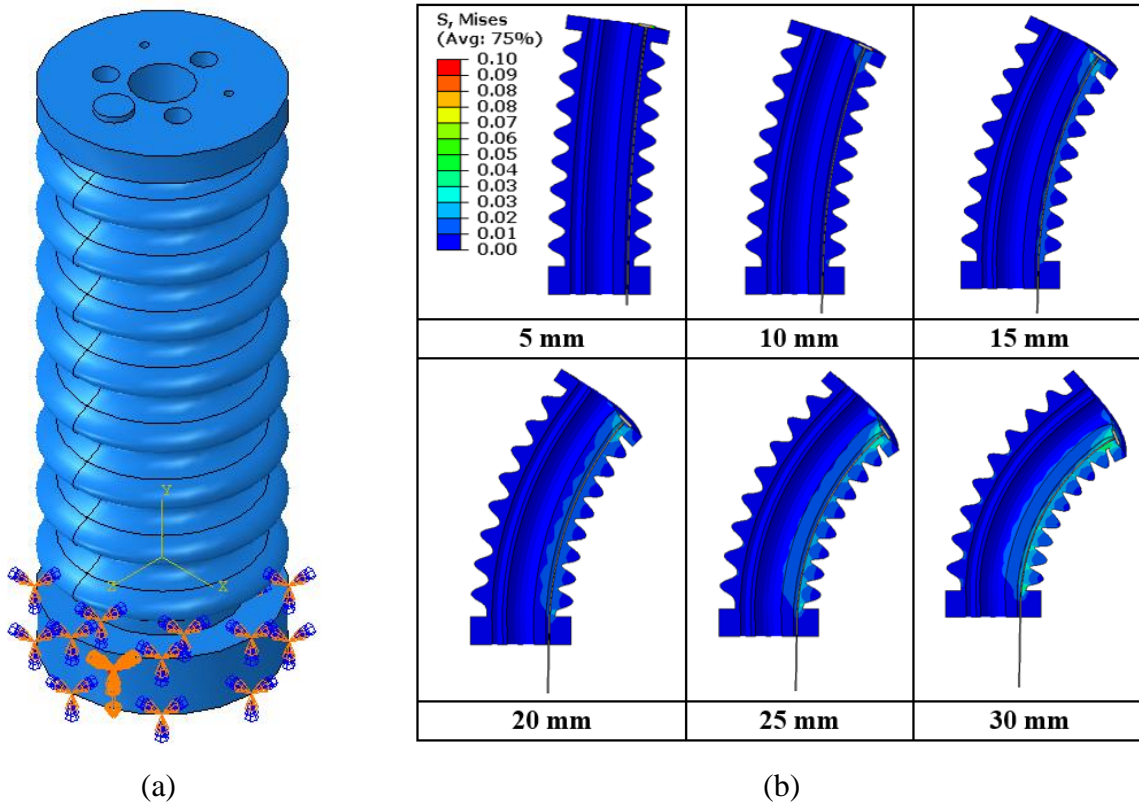


Figure 45. Simulation for the bending behaviors of the soft robot arm. (a) Setup for the boundary condition of the robot. (b) Stress distribution and deformation of the soft arm under various cable pulling displacements.

By pulling the cable, the soft arm would gradually flex to the corresponding direction. And the soft materials surrounding the cable hole would be continuously compressed. So, a high stress concentration would first occur at the contact area near the cable fixture, and then spread along the length direction of the cable (Figure 45b). Due to the complicated contact, a fully bent deformation could not be attained for the simulation of this soft arm. After that, the effects of embedding LMPA tubes inside the soft arm were analyzed. The physical properties of Field's metal in solid state were selected from Table 4. LMPA cores were bonded onto the hole surfaces by tie constrain, and self-contacts of the outer surfaces of the arm were defined in case of large deformations. To model the real situations and reveal the hardening effects from LMPAs, a gravity field was applied along the corresponding direction. Also, the cable-pulling effect was simplified by adding forces on the cable fixation point due to the difficult convergence.

Table 4. Major mechanical properties of Field's metal.

<b>Material</b>	<b><i>Young's Modulus</i></b>	<b><i>Density</i></b>	<b><i>Tensile strength</i></b>	<b><i>Strain</i></b>
LMPA	3050±209 MPa	$7.9 \times 10^{-3} \text{ g/mm}^3$	25.95±1.47 MPa	2.05±0.18%

The FEM results of the effect of LMPA tubes on the deformation of the robotic arm under different situations were illustrated in Figure 46. When only gravity was applied to a horizontally orientated soft arm (Figure 46a), its maximum strain could be reduced from 0.57 to 0.14 when the LMPAs became solid. When a soft arm was placed vertically, the LMPA tubes in solid state would prevent it from deflecting when a cable inside was driven by exerting a pulling force of 2 N (Figure 46b). Moreover, the combination of LMAP tubes and cable pulling effects could greatly enhance the loading capacity of the bent soft arm. As shown in Figure 46c, when an extra load (1 kg weight) was applied to the tip end of a soft curved arm, the robotic arm would be further bent with LMPAs in liquid state. While the LMPAs in solid status could greatly improve the bending stiffness of the soft curved arm, with only a slight further deflection.

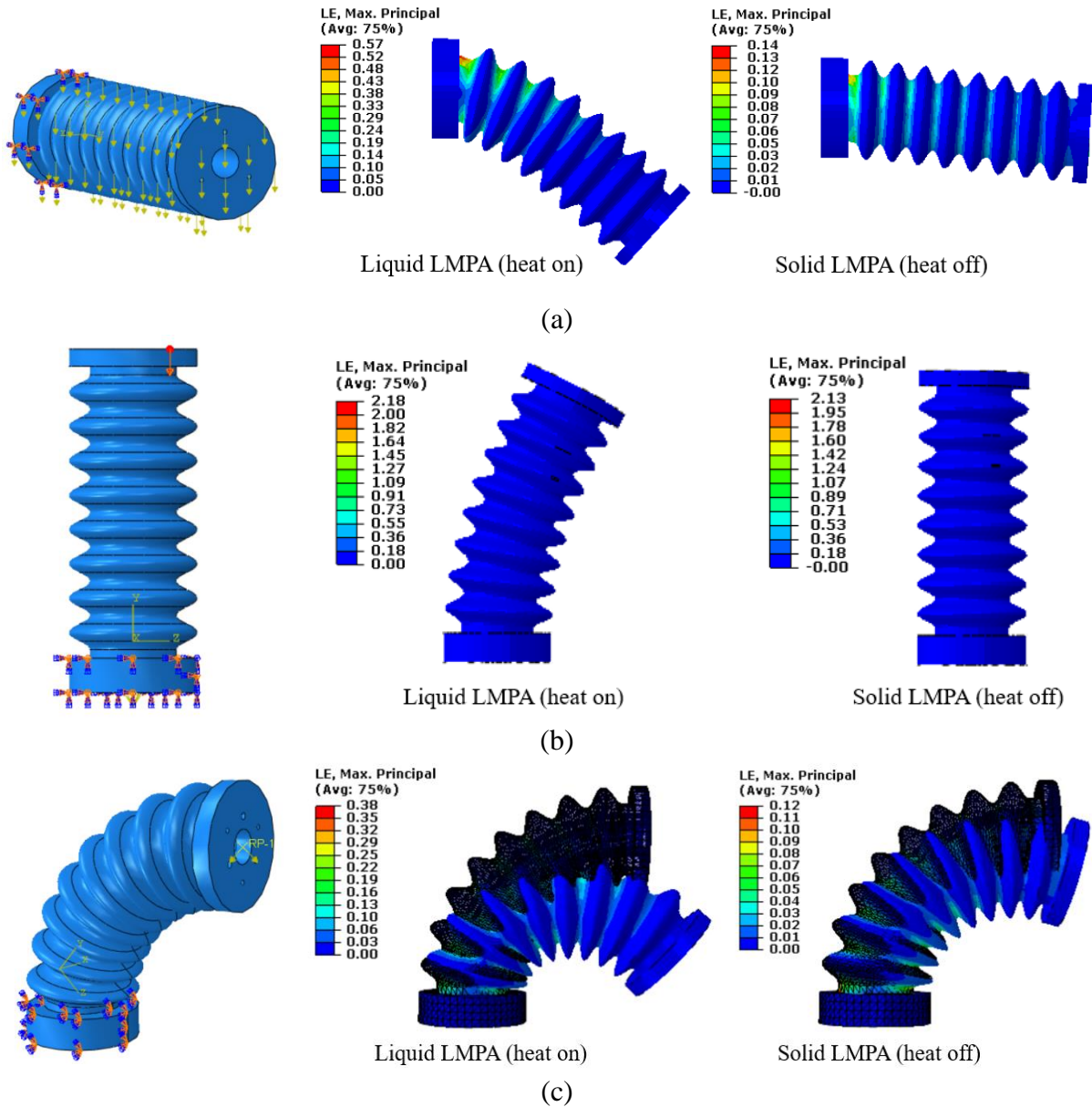


Figure 46. Simulation of the hardening influence of LMPAs on the soft arm. (a) Deformation of a horizontally placed soft arm under gravity with and without solid LMPAs. (b) Deformation of a vertically upward arm actuated by one cable with and without solid LMPAs. (c) Deformation of a soft arm under a tip external load (1 kg) with and without solid LMPAs.

For simulating the multi-material finger actuator, the main frame, and the soft filling blocks (porosity=0, to reduce modeling cost), as well as other parts, were discretized by 4-node tetrahedral elements. The filling blocks were bonded to the stiffer finger frame by tie constraints (Figure 47a). The surface-to-surface contacts were set for the cable and holes of the mainframe and filling blocks,

and for the cable fixture and fingertip (Figure 47b). A displacement load would be directly applied to the cable end and all DOFs of the top segment of the finger were fixed, as shown in Figure 47c.

The other modeling setups were the same as those in Section 2.2.2.

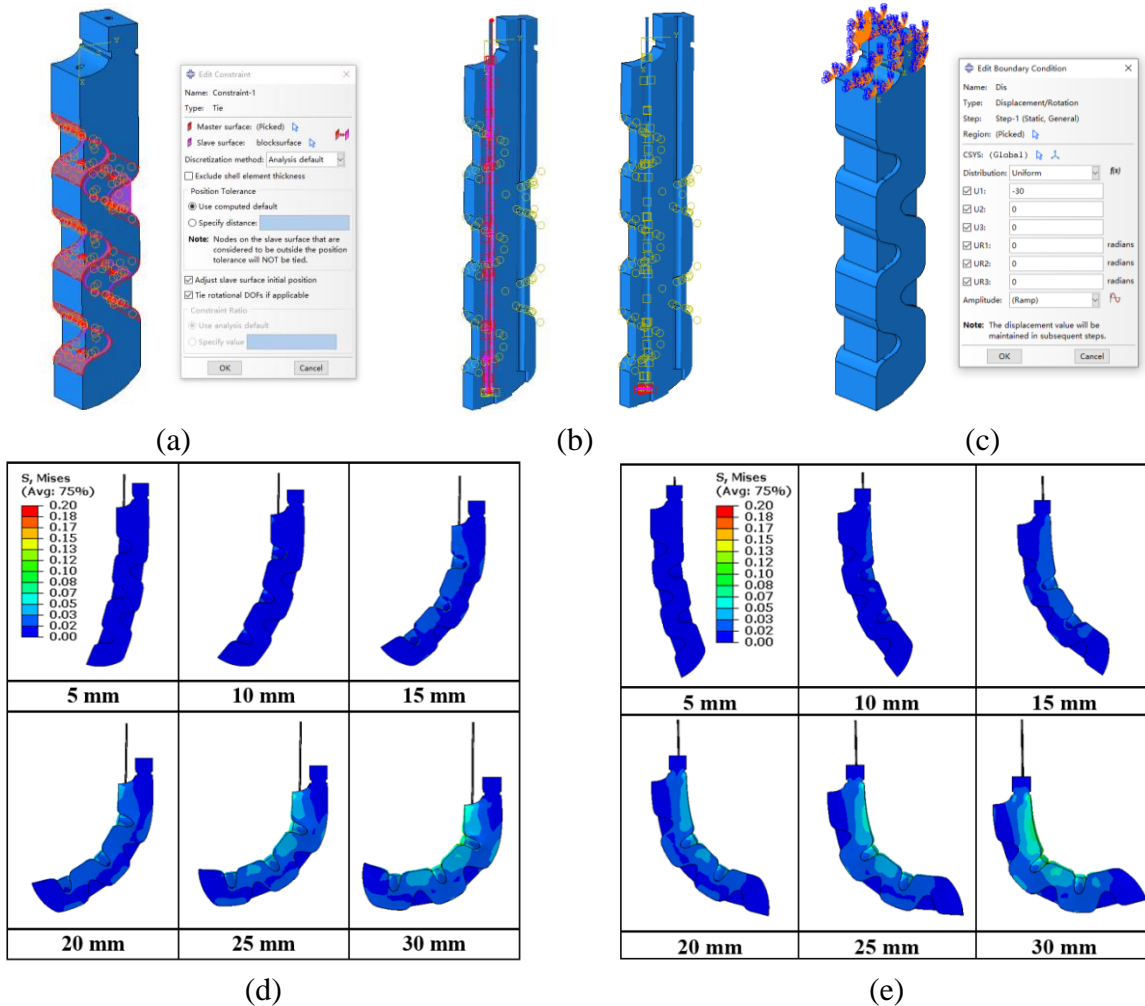


Figure 47. Simulation results for the multi-material soft finger actuator. (a) Constraint setup for the main frame and soft filling blocks. (b) Contact setup for the cable and holes. (c) Boundary condition setup. (d) Inward bending deformations and stress distributions of the finger actuator. (e) Outward bending deformations and stress distributions of the finger actuator.

As could be indicated in Figures 47d and e, the improved bidirectional soft finger actuator was still able to conduct evident inward and outward bending. In the previous design, the phalanges of the soft finger actuator were divided by several notches with the angle of 90°, and the backside of the finger actuator was just left as default. For enhancement, the notch structures were replaced

by the flexible hinge structures with softer and porous filling blocks as cable coverages. From the simulation, the porous filling blocks would be gradually compressed (as the porosity was not taken into account during the modelling, the actual deformation of the finger would be larger). Similarly, stress concentrations were observed near the flexible hinge structures (i.e., notch and filling block).

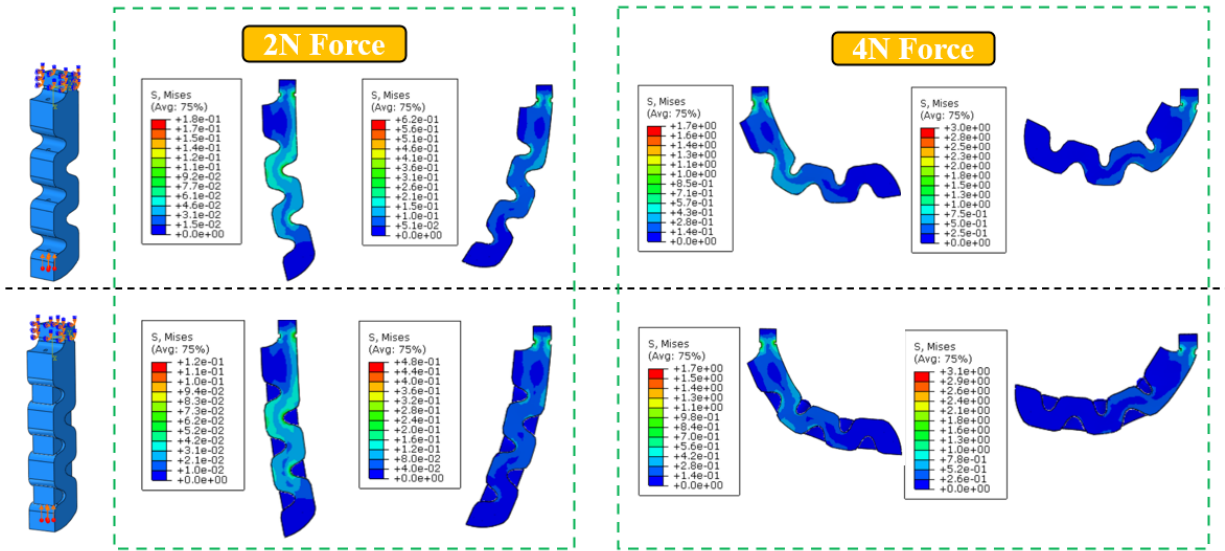


Figure 48. Simulation result for the effect of soft filling block on inward & outward deformations of the finger actuator.

To further validate the effects of adding soft filling blocks onto the main frame of the finger actuator, the simulation model was simplified by removing the cable system and directly applying an upward concentrated force to the area where the cable fixed at. The results of the finger actuator with and without adding softer filling blocks at the notches were described in Figure 48, and those notch fillers would not evidently hinder the bending motion of the finger actuator as the porosity of these soft filling blocks was set as zero during the simulation.

#### 4.2.3 Structure Design of Wearable Finger Patch for HMI

Among wearable devices for HMI, hand motions are the mostly captured information for different applications, such as dactylology, robotic control/guidance, and VR/AR. In the proposed HMI design, we used the TENG technology to design a self-powered motion detector and provide

instructions for manipulator operations. As shown in Figure 49a, flexion and extension of human finger are based on rotations of hinge joints located between phalanges. Proximal interphalangeal (PIP) joint, the joint located between the proximal and the middle phalanxes, possesses the highest flexibility and motion independence among all finger joints. In addition, the tensile displacement of the skin around the PIP joint is linearly related to the joint rotation angle, enabling quantitative and qualitative measurements. As a result, a TENG-HMI patch would be designed in sliding mode and include two triboelectric layers (PTFE and copper) with electron injection applied to improve its overall output (Figure 49b). In detail, Part A consisted of a PET strip covered with a thin copper layer and partially stuck to the adhesive surface of a piece of Kinesio tape. Part B was built with a shallow chamber, and a PET strip coated by a copper layer and then a PTFE layer, was sandwiched between two pieces of Kinesio tape. When the TENG patches were respectively attached onto the proximal and middle phalanxes, the tribo-layers would slide relatively under the rotation of finger joint, dragging the copper strip out of/into the chamber and generating electrical signals. Kinesio tape was used as the substrate due to its great flexibility, durability, and biocompatibility.<sup>[103]</sup>

Figure 49c depicted the working principles of the TENG patch. Initially, two triboelectric layers were in close contact and overlap with each other, and no electric potential would be induced due to the electrostatic equilibrium between PTFE and copper layers. Once the finger bent inward, a relative slide would occur between the tribo-layers. Then, a potential difference would be formed between electrodes, resulting from the in-plane charge separation. Within a closed circuit, a current would be triggered to neutralize the electrons due to the triboelectric effect. Keep flexing the finger would prolong the charging process and a new electrostatic equilibrium state would be made once a full separation between the tribo-layers was done. On the contrary, when the finger extended, the copper layer would slide backwards to be stacked together again, resulting in a reverse current.

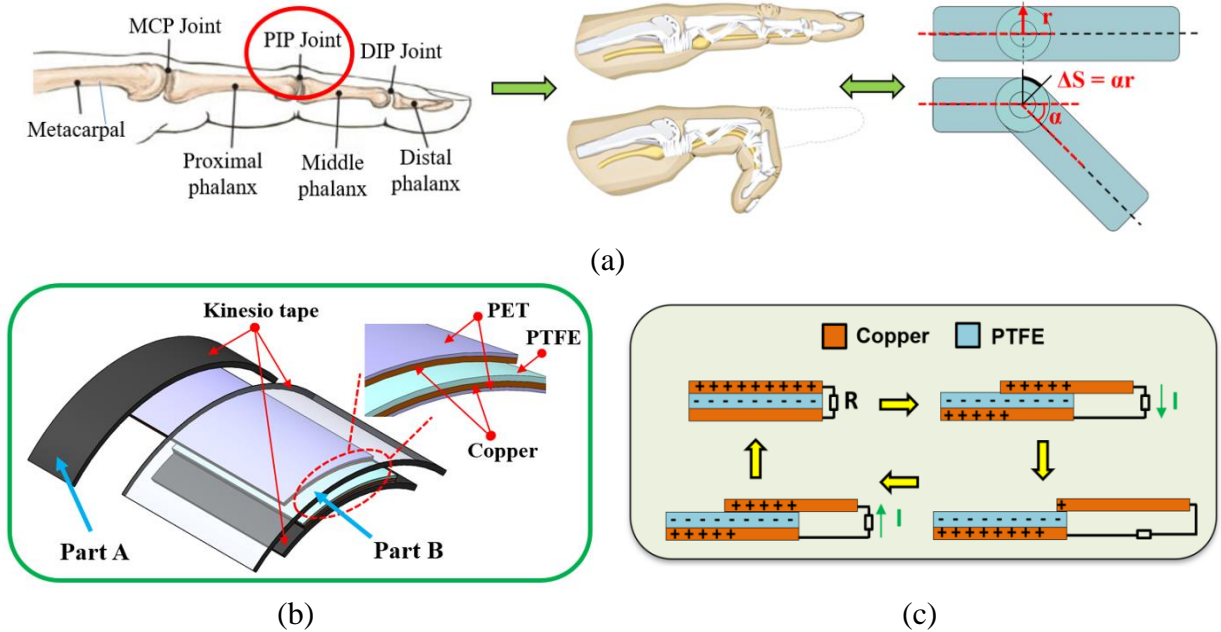


Figure 49. Design and working principle of the TENG-HMI patch. (a) Schematic illustration of an index finger and the corresponding hinge model based on PIP joint. (b) Schematic structure of the TENG wearable patch. (c) Working principle of the HMI patch in sliding mode.

#### 4.2.4 FEM Simulation for Sliding-Mode TENG

To support this proposed mechanism, corresponding electric potentials between the PTFE layer and the copper layer were modeled by COMSOL under open-circuit condition. The 2D model was used due to the long and thin configurations of the involved layers. The combined PTFE and copper layer (length of 36 mm; thickness of each, 0.5 mm), and the copper layer (length of 36 mm; thickness of 0.5 mm) were established with a rectangular area assigned the infinite element domain with air properties, simulating the environment. The same boundary conditions as those in Section 2.2.3 were utilized. The simulation results in Figure 50 revealed the potential distribution between the tribo-layers in the sliding mode. The potential difference between the layers almost disappeared when the two layers overlapped with each other, and when their separation distance became larger, the potential difference gradually improved. As a result, a high voltage signal would be generated when the two tribo-layers got further apart, i.e., the human finger bent fully. And the bending angle

of human finger was in direct proportion to the signal output of the TENG patch.

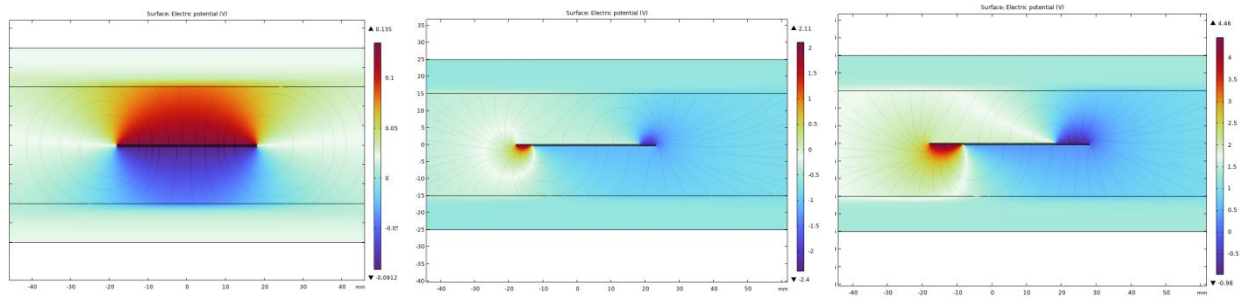


Figure 50. Simulation result for the TENG-HMI patch in sliding mode.

#### 4.2.5 Fabrication of Soft Robotic Manipulator

An assembled 3D-printed mold with two reverse sawtooth covers and cylindrical rods, was first prepared for mold casting with polyvinyl chloride (PVC) tubes as the hole fillers for installing driven cables (Figure 51a). Ecoflex 00-30 (a weight ratio of Parts A and B = 1:1) was well mixed and poured through the top opening of the mold. After curing, the soft robotic arm segments were demolded with tube filler removed and bonded robustly by silicone rubber glue, Sil-poxy (Smooth-on Inc., USA). To reduce the friction between cables and silicone body, and to avoid cable-induced damage to soft matters, short tubes were trimmed and bonded to the junctions of the arm segments. Finally, braided fishing cables (30 LB) were guided through the cable holes, and each had one end surrounded around a screw on the cable fixator and the other wound over the motor shaft.

Fabrication of the LMPA tube was in Figure 51b. Molten Field's metal (ChemistryCabinet, USA) in hot water (100°C) was sucked into a silicone tube (Uxcell, China) with an inner diameter of 4 mm via a syringe. Holding the position of the plunger and removing the tube out of water, the liquid LMPA core would gradually solidify at room temperature. Then, the plastic tube filled with solid alloys was pre-stretched longitudinally by pushing it to slide along the metal core (2~3 mm), and the stretched tube parts were filled with silicone adhesive for encapsulation. Finally, a coil of nichrome (radius of 0.05 mm) was wound around the tube for applying Joule heating.

The fabrication of the soft finger actuator was based on mold-casting as well (Figure 51c). A printed mold was prepared with PVC tubes as pre-hole fillers and filled up with Dragon skin 30 mixture (weight ratio of parts A and B, 1:1). The stiffer mainframe was demolded after curing with tubes trimmed and inserted correspondingly, which could reduce wear and tear arising from cable pulling. Elastomeric foam-like filling blocks were made by mixing Ecoflex 00-30 with salt particle for desired porosities. A centrifugal mixer (ARE-310, Thinky, US) was used to mix the elastomers and salt particles for making a homogenous compound, and ultrasonic bath was used to accelerate dissolution of the remaining salt in elastomers. For assembly, fishing lines were routed sequentially along the holes of the finger frame and soft blocks, each with one end twined on a spindle and the other fixed near fingertip. Sil-poxy was employed to combine the finger frame with soft blocks.

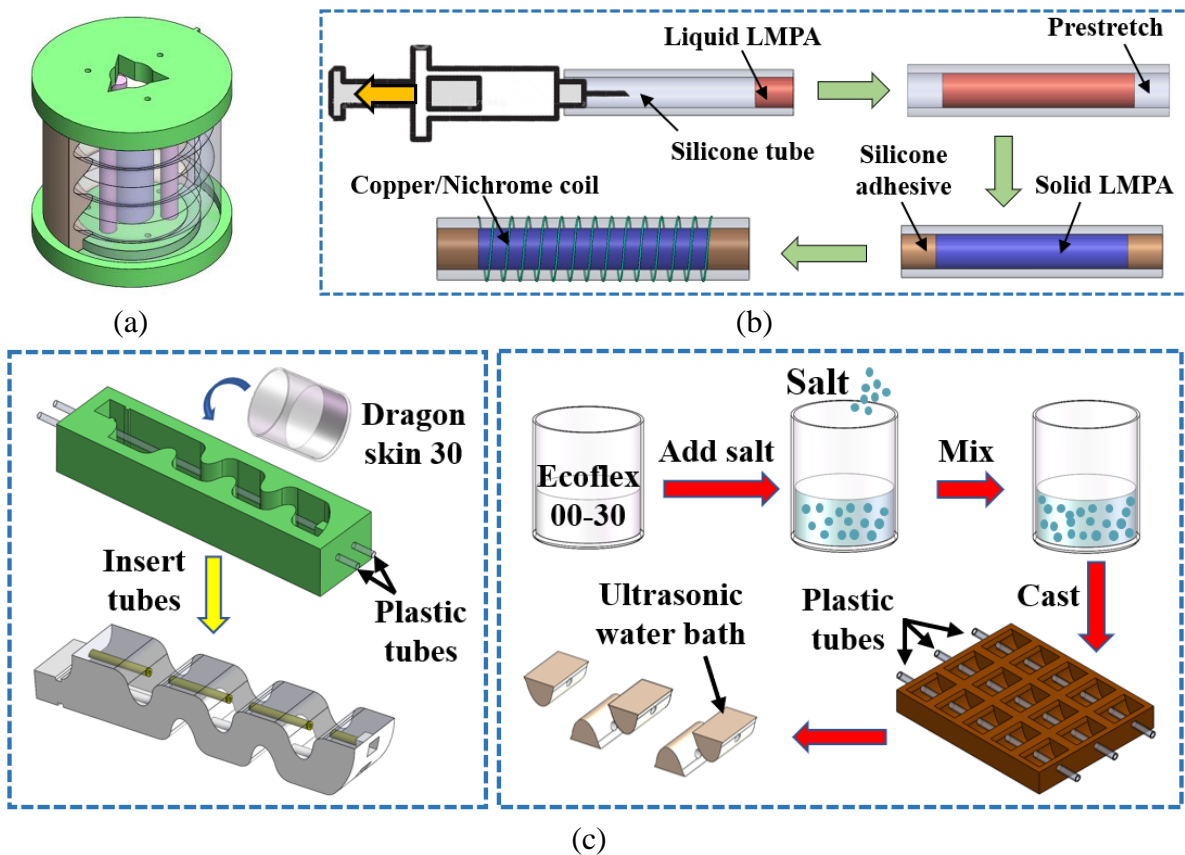


Figure 51. Fabrication for the soft manipulator. (a) Casting mold for the soft arm. (b) Schematics of fabrication steps for the LMPA tube and (c) the multi-material soft finger actuator.

#### ***4.2.6 Fabrication of Kinesio-Tape-based TENG***

The PET film (thickness of 0.2 mm) was coated by a thin copper foil (0.05 mm) (EMI Ltd., China), and then multiple pairs of PET-based strips were cut from it in two sizes ( $1.5 \times 3.6 \text{ cm}^2$  and  $1.5 \times 5.0 \text{ cm}^2$ ). The PTFE film (0.1 mm) was placed onto the copper layer of the shorter strips with wires connected. Meanwhile, pieces of Kinesio tape (SME Inc., USA) were cut as a substrate with appropriate shapes. The longer strip was bonded to the adhesive layer of a slender piece of Kinesio tape, forming Part A, while the shorter one with PTFE was stuck to the top of the tape via a double-sided adhesive tape. To apply electron injection, the PTFE strip was connected to the anode of a high voltage polarimeter (ET2673A), and the needles in an array pointing to the PTFE surface were wired to the cathode (10 mm vertical distance). A polarization voltage of 6 kV was applied onto the needles and lasted for 4 min for electron injection. Then, a wider Kinesio tape with its release liner partially trimmed on both sides was placed and stuck on the shorter strip, forming a free-moving chamber, Part B.

#### ***4.2.7 Data Processing and Wireless Control for HMI***

As discussed before, the voltage induced from TENG patch had a positive correlation with the bending angle of human finger, a threshold-based control method could be used for capturing the intended finger motions with the assistance of a suitable Arduino board and a radio-frequency module that are commercially available in the market. Specifically, the triboelectric signal induced by a single flexion-extension cycle of human finger would be conditioned (amplified and rectified) and acquired by an Arduino board via an analog port. Then, the microprocessor would compare the received signals with the preset thresholds and determine whether to transmit the corresponding commands wirelessly to the control board that controlled the soft manipulator (Figure 52).

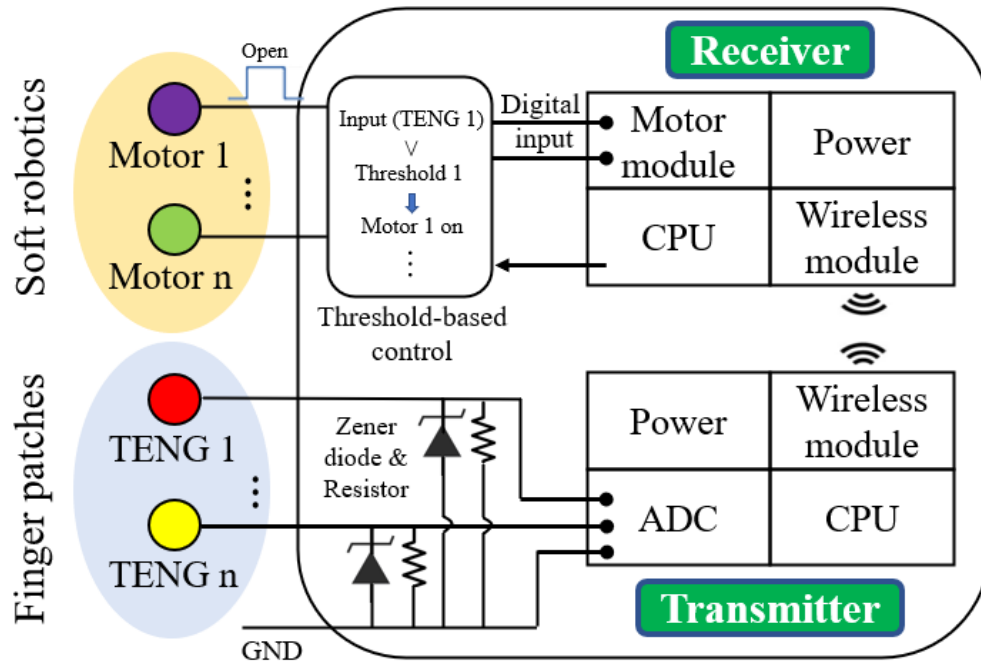
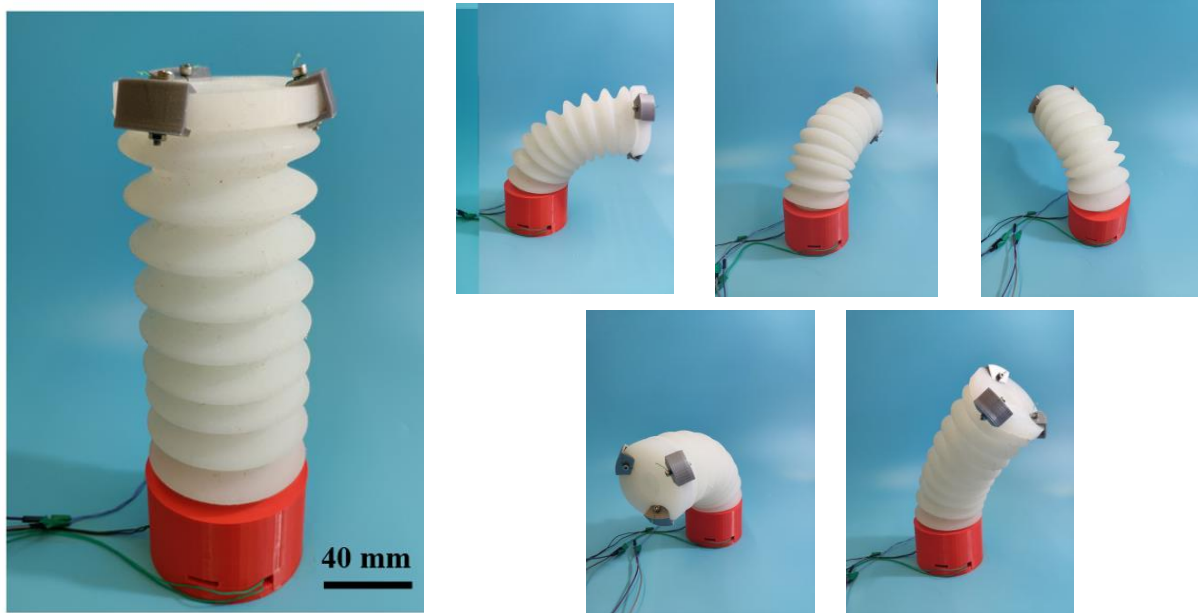


Figure 52. Control strategy through wireless transmission and threshold logic for communication between soft manipulator and TENG patch.

Figure 53 depicted the electronic diagram for the wireless HMI control system. The analog voltage signals generated from the TENG patch were converted into digital signals via an analog-to-digital converter embedded in the port of Arduino Nano. However, the analog port only allowed positive voltage,  $\leq 5$  V, so a resistor (500 M $\Omega$ ) and a Zener diode (5.1 V) were connected in parallel with the TENG patch to remove the background noises, adjust the input voltage levels, and protect the circuit board. The microprocessor of transmitting board could compare the trigger signals with the preset thresholds and decided whether to send the commands to the corresponding motors via radiofrequency (RF) module (nRF24L01), which utilized the 2.4 GHz band and worked with baud rate of 250 Kbps~2 Mbps, ensuring the stable and fast multi-channel data communication. For the motion control board actuating the soft robot manipulator, an actuation module (L298n) was wired to the Arduino UNO to enlarge the allowed operating voltage for motors (up to 46 V). The program for realizing the remote and threshold control of the soft manipulator, by using Arduino UNO, was





(a)

(b)

Figure 54. Behaviors of the soft arm with omnidirectional bending ability. (a) An assembled soft robot arm driven by cables. (b) Bending deformations of the soft arm in different directions.

Then an as-fabricated LMPA tube was shown in Figure 55a, The LMPA core stored in the PVC tube could be fully melted in  $\sim 2$  min when a constant current of 0.3 A was applied. However, the cooling process of LMAP took longer time (160 s) due to the poor convection between LMPAs and the surrounding air. A higher current accelerated the melting process but not the cooling, which posed a big issue for realizing fast stiffness tuning for soft robotic system and should be addressed in the following research. Insertion of these LMPA tubes improved the overall stiffness of the soft manipulator when the LMPA tubes were inactive (i.e., w/o heat applied) and made the manipulator withstand its own weight under gravity (Figure 55b). The total mass of the soft robot was  $\sim 860$  g. It was observed that the soft manipulator could remain straight with only a small inclination angle of  $23^\circ$ , deviating from its initial horizontal position, when LMPA cores were in solid state without applying Joule heating, while the inclination angle increased to  $63^\circ$  under gravity when the LMPAs were heated to a fully liquid state.

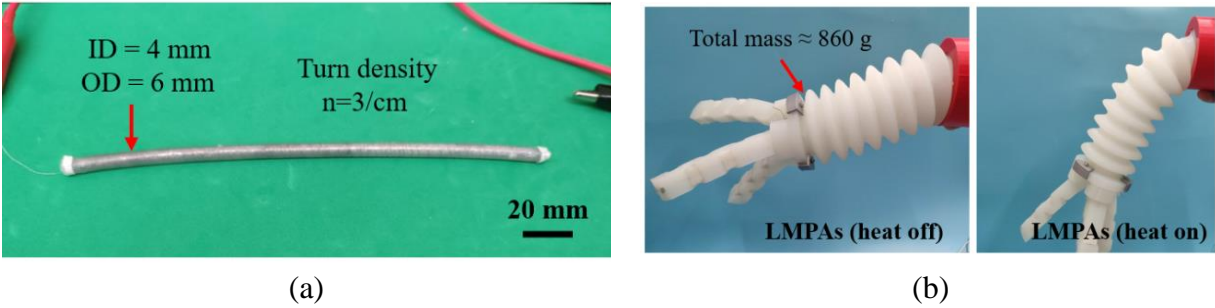


Figure 55. Performance of LMPA tube and its stiffness adjustment effect. (a) Photograph of an as-fabricated LMPA tube. (b) LMPA tubes prevented the deflection of a horizontally placed soft manipulator under gravity.

The bidirectional bending behaviors of the multi-material soft finger actuator were shown in Figure 56a. As the motor rotated, the length of the cable twined on the spindle would be reduced and the tension in the cable would make the soft finger gradually bend along a certain direction by squeezing the filling blocks placed in the semi-ellipse notches. Soft blocks with a lower modulus were preferred for bending actuation. Experimental results showed that the soft finger produced a  $112^\circ$  inward bending when a cable-pulling force of 5.2 N was applied, and an  $80^\circ$  outward bending under a force of 4.8 N. A gripper (Figure 56b) was assembled onto the arm segment by mounting soft fingers onto a stand made of Dragon Skin 30. To enlarge the initial grasping scope, each soft finger would exhibit a  $30^\circ$  inclination angle, and the cables inside the finger actuator were guided through the pre-designed holes and pathways on the stand to reach the corresponding motor fixed on the bottom base. The finger actuators in the gripper could operate separately or simultaneously by controlling the motors.

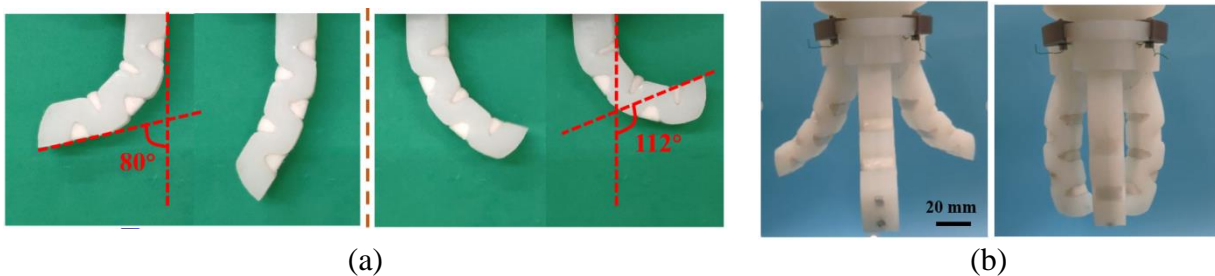


Figure 56. Performance of soft multi-material finger/gripper. (a) Bidirectional bending of the soft finger. (b) Expanding and grasping postures of the assembled gripper.

### 4.3.2 Behavior of TENG-HMI Wearable Finger Patch

After wearing the TENG-based finger patches (Figure 57a), finger flexion and extension would induce relative sliding motions between the tribo-layers and thus generating voltage signals and the output values were highly related to the bending angle of human finger. We measured the output voltage signals from different bending gestures of fingers (Figure 57b). As could be seen from the real-time monitoring data, the voltage varied with the finger flexion angle (PIP joint) and such a triboelectric signal exhibited merits of fast response and ultrahigh sensitivity, demonstrating obvious peaks at the slight flexion cycles ( $<30^\circ$ ). To make the patch a stable and robust “controller” for robotic operation, the signals induced via involuntary finger movements or from the interferent movements of adjacent fingers should be eliminated through a suitable signal processing method. Herein a threshold control strategy was adopted for intent detection. It was shown that a maximum peak voltage of 1.5 V could be induced with an external resistor load of 500 M $\Omega$  by a slight flexion of thumb ( $\sim 30^\circ$ ), while the minimum peak voltage of 3 V was generated when the thumb ( $\sim 90^\circ$ ) was fully bent (frequency 1 Hz). Thus, a threshold value in the range of 1.5~3 V, close to the upper limit, should be selected to guarantee the robust and stable trigger response. With this approach, a valid signal would be generated for control purposes each time the finger bent fully and intently.

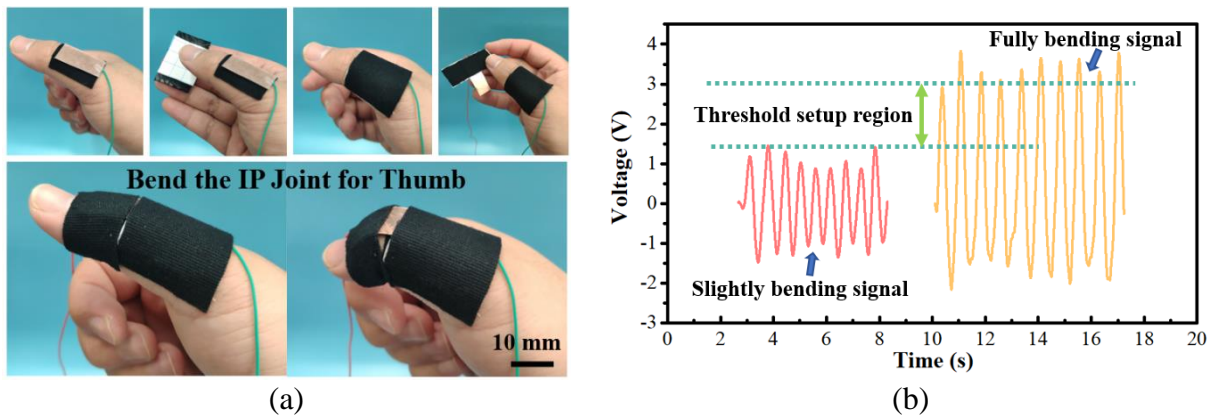


Figure 57. TENG-HMI wearable finger patch. (a) Wearing process of the TENG patch on finger. (b) Voltage outputs of the TENG patch induced from slight and full finger bending, respectively.

### 4.3.3 Demonstration of HMI for Soft Manipulator

Figure 58a presented the interactions of the soft manipulator and the human fingers via the TENG-HMI patches. In the first case, three TENG-based HMI patches were designated separately for controlling the bending of the arm (corresponding to three cables). When a valid trigger signal was applied through finger flexion, the signal would be converted into a command for controlling the actuation of motors. As illustrated in Figure 58b, when the index finger was bent, the soft arm would bend to the left side, and then the flexion of thumb would actuate another motor to turn the arm counterclockwise. For a hanging manipulator shown in Figure 58c, the trigger signals induced from the flexion of thumb could be programmed to control the gripping of the soft gripper. A series of actions were performed sequentially: the soft arm was first bent to approach the object by flexing the right index finger; the trigger signal induced by the thumb would drive the soft gripper to grasp and hold the object. A secure grasp could be achieved by multiple flexions of the thumb. Finally, the soft arm restored back to its original position/gesture by bending the left index finger.

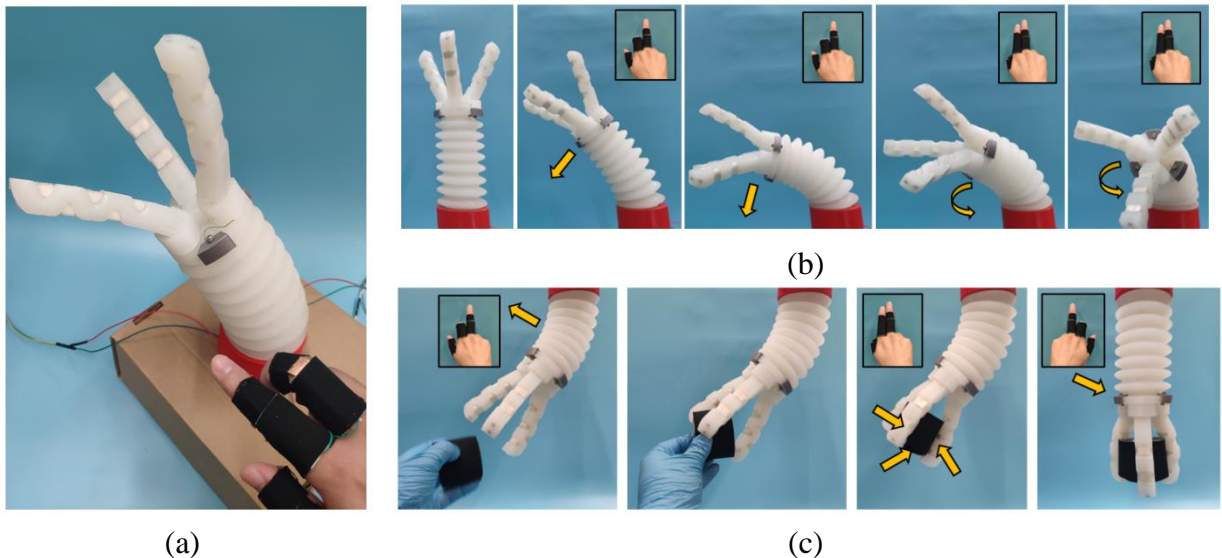


Figure 58. Teleoperation of the soft manipulator by TENG-HMI patches. (a) A soft robot system in a synchronous control scenario. (b) Demonstration of the omnidirectional bending of the soft arm by TENG patches. (c) Demonstration of the collaborative operation (navigation & grasping) of the soft manipulator by TENG patches.

#### 4.4 Conclusion and Discussion

In summary, we have developed a soft manipulator system based on the bio-inspired cable-driven soft arm and soft gripper together with the self-powered TENG-HMI wearable finger patch. The soft manipulator arm is bellow-profiled and omnidirectionally bendable (realized by a 3-cable configuration), and the three-finger gripper is able to perform both inward and outward bending, greatly expanding its operation range. The LMPA tubes embedded in the soft robot arm can adjust the overall stiffness of the robotic body through phase changes of the alloy under Joule heating, to overcome the gravity and pressure from external loadings. Although the heating process of LMPAs (solid to liquid status) could be accelerated via high-power sources, the cooling process (liquid to solid status) usually takes a much longer time due to the poor convection between LMPAs and the surrounding air, resulting in a slow stiffness tuning speed. Therefore, another method for realizing swift stiffness adjustment for the soft robotic arm should be discussed later for a more efficient behavior. Multiple materials are adopted for designing the finger actuator, including a stiffer frame for structural robustness and some porous filling blocks to cover the voids of flexible hinges for encapsulating exposed cables during operation but still maintaining the flexibility of the soft finger actuator. Such multi-material design has been proved to be an effective method to design any soft robotics actuated by cables. Based on the cable-driven mechanism, the soft manipulator is flexible in motions and controllable by adjusting the motors.

The TENG-based wearable device is a flexible, compact, and biocompatible human finger patch for self-powered motion detection of human fingers. Flexion and extension of human finger will induce a relative sliding motion of the tribo-layers inside the finger patch, and produce a signal correlated with the bending degree of human finger. For a concise implementation and minimizing interference, a threshold-based control strategy is utilized to screen out the trigger signals for HMI

between the soft manipulator and the operator (through his/her finger motions). This work presents a compact design and way for self-powered finger motion sensing and offers a solution to construct a straightforward wireless HMI for soft robotics development.

## CHAPTER 5: CABLE-DRIVEN STIFFNESS MODULATION

### 5.1 Objective

Stiffness modulation through phase-changes of the LMPAs suffered from long heating and cooling lag time, which would definitely hinder the real-world applications for soft manipulators. In this chapter, a hybrid stiffness adjustable structure inspired from mammal spines was developed and integrated into the soft arm proposed in Chapter 4 to achieve a faster stiffness modulation with an appropriate varying range. The hybrid structure was comprised of alternatively stacked soft and hard disk-like segments and was actuated via cables. By utilizing this stiffness adjustable structure, the soft manipulator mentioned before would be compact and consistent in actuation approaches. This task was mainly based on numerical calculations and finite element analysis due to the mature theories and the sub-objectives were listed as follows:

- A hybrid rod structure with alternatively stacked soft and rigid disk-like segments was developed and embedded into the large central hole of the soft robotic arm proposed in Chapter 4.
- The behaviors of the hybrid structure on stiffness adjustment were investigated through numerical calculation and FEM, and the results from different methods were compared to ensure the simulation accuracy for the hybrid rod structure.
- The stiffness adjustment effects of the hybrid rod structure on the soft robotic arm were studied based on finite element analysis, owing to the high simulation accuracy proved by the previous works.

## 5.2 Method and Result

### 5.2.1 Structure Design for Hybrid Rod Structure

Taking advantage of the unique feature of most soft materials, i.e., their stiffnesses change under compression. A hybrid rod structure was proposed to change the stiffness of the robotic arm shown in Chapter 4, where rigid (PLA) and compliant (silicone rubber) disk-like structures were connected alternately in series, and a cable was deployed through, with one of its ends fully fixed (Figure 59a). This structure shared great similarity with a spine, which consists of hard bones and flexible cartilages connected alternatively (Figure 59b). Pulling the cable which ran through the hybrid rod structure would compress the soft materials sandwiched between those hard segments, thus improving the axial stiffness and then the bending stiffness of the whole structure. Releasing the cable would turn the rod structure back to a flexible state. As for the thickness of soft and hard segments of the structure, when the soft segments were squeezed, the soft material would protrude in radial direction. A long soft part induced larger radial deformations upon compression and then would lead to uneven bending behaviors of the hybrid structure. While a relatively short length of soft segments would induce a smaller radial protrusion and a higher resistance to buckling for the entire structure (as the critical load is inversely proportional to the length squared). The hybrid rod structure would then be embedded into the center hole of the proposed soft arm and provide variant bending stiffness when needed (Figure 59c).

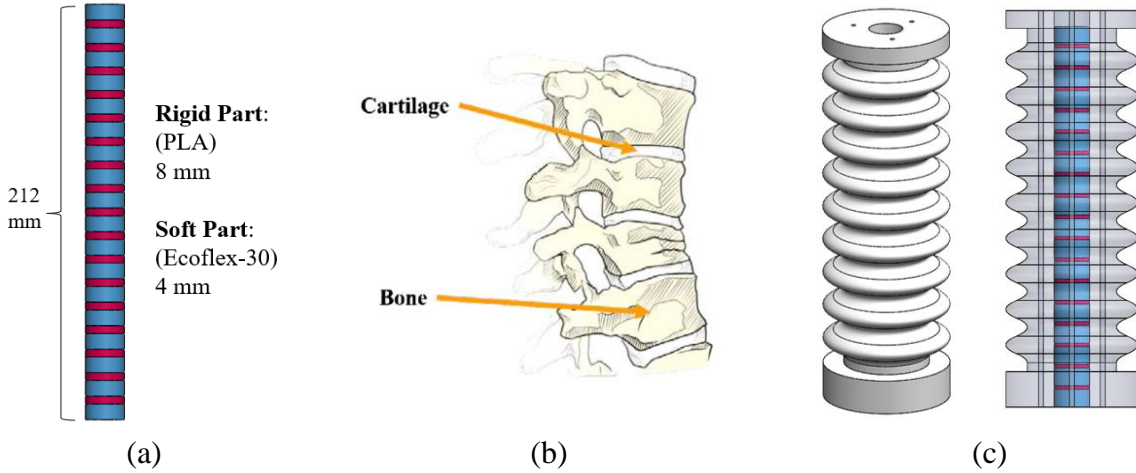


Figure 59. Design of the hybrid rod structure. (a) Dimensions of the hybrid rod structure. (b) Illustration of a human spine. (c) Integration of the hybrid rod structure with the soft arm.

### 5.2.2 Numerical Modelling for Hybrid Rod Structure

Variation in the stiffness of the hybrid rod structure was induced by the deformation of the soft segments sandwiched by the stiff segments. Material properties of the soft segment determined the variation of bending stiffness of the entire structure, and here a softer rubber material, Ecoflex 00-30 was employed (Young's modulus of 0.125 MPa without deformation). To model the hybrid rod structure, we adopted the Pseudo-rigid-body model, which described the relationship of motion and force of an elastic member via the rigid-body mechanism. To be specific, the soft segment was regarded as a combination of a torsional spring and two stiff rods (Figure 60a). Then, the bending stiffness represented by  $(EI)'$  of the hybrid rod structure was first derived through Equations (1) and (2).  $S$  denoted the shape factor of the rod structure ( $R$  and  $l$ , the initial radius and length of soft segment).

$$S = R/2l \quad (1)$$

$$(EI)' = (E + 2GS^2)I \quad (2)$$

where  $E$  and  $G$  were the Young's and shear modulus, and  $I$  was the area moment of inertia of the rod structure,  $I=\pi(2R)^4/64$ .

To simplify the modeling process, we assumed the material properties of soft segment were not changing upon compressive deformation. The parameters for the pseudo torsional spring under pure vertical loading condition were:  $\gamma=0.8517$ ,  $c_\theta=1.2385$  and the pseudo torsional spring constant  $K$  could be denoted from Equation (3). After deriving the spring constant  $K$ , we could measure the angle of each bending rod in the Pseudo-rigid-body model, by Equations (4) and (5) via MATLAB. In the end, the cumulated deflection of the tip end of the hybrid rod structure was figured out via Equation (6).

$$K = 2.67617 \times \gamma \frac{(EI)'}{l} \quad (3)$$

$$K \frac{\theta_n}{c_\theta} = F(t + \gamma l) \cos \left( \sum_{j=1}^n \theta_j \right) \quad (4)$$

$$K \frac{\theta_i}{c_\theta} = K \frac{\theta_{i+1}}{c_\theta} + F(t + l) \cos \left( \sum_{j=1}^i \theta_j \right) \quad (5)$$

$$D = \sum_{i=1}^n \left\{ (t + l) \sin \sum_{j=1}^i \theta_j \right\} - (1 - \gamma) l \sin \left( \sum_{j=1}^n \theta_j \right) \quad (6)$$

The numerical results for the bending displacements of the hybrid rod structure were shown in Figure 60b under different bending forces applied on its tip end (0.1-1N). And the results would be used to compare with those gotten from FEM analysis in the following section, so as to validate the accuracy of the modeling process for the proposed hybrid rod structure.

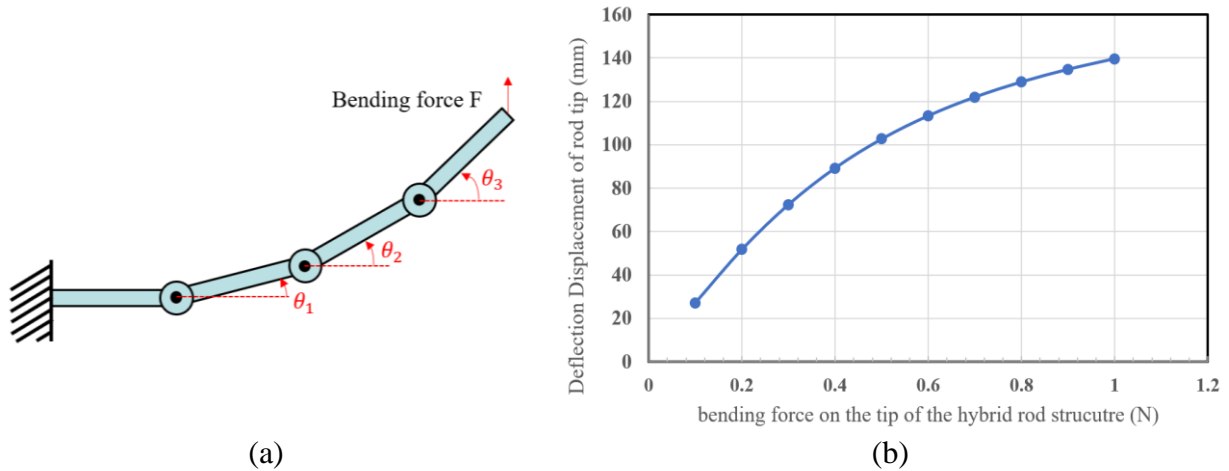


Figure 60. Numerical modeling for the hybrid rod and calculated results. (a) Pseudo-rigid-body models for the hybrid rod. (b) Deflection of the rod tip under different bending forces.

### 5.2.3 Finite Element Analysis for Hybrid Structure

Simulations of bending stiffness variation due to compressed soft segments and interactive effects on the soft robotic arm would be performed via Abaqus 6.14. The CAD model of the hybrid rod structure was directly imported into Abaqus as an entire unit, without merging the intersections of CAD parts. By doing so, we could easily assign various material properties (soft Ecoflex 00-30 and stiff PLA), as shown in Figure 61a, and the hybrid structure would be taken as a whole without the need of applying constraints later. To verify the enhancement in bending stiffness of the hybrid rod structure, its bottom would be constrained in all DOFs, and cable-pulling process for the hybrid rod was simplified by adding a downward pressure on top surface. Different levels of compression pressure and horizontal bending forces (leading to deflection of the hybrid rod) would be applied to the simulation model (Figure 61b). At first, the hybrid rod was deflected under a 1 N bending force applied on top (Figure 61c), so as to compare with the numerical result via the Pseudo-rigid-body models. The deflection displacement was 139.47 mm through finite element analysis and the corresponding numerical result was 139.7 mm, only 0.17% deviation. Then the horizontal bending force was decreased to 0.1 N to check the effect of compression pressure applied to the hybrid rod.

As shown in Figure 61d, without any compression on the hybrid rod, its deflection displacement was 23.88 mm, which was close to the numerical result, i.e., 27.2 mm. Improving the compression pressure to 0.01 and 0.02 MPa made the deflection displacement of the hybrid rod decline to 9.54 mm and 2.56 mm, respectively, indicating that the further the hybrid rod was squeezed, the stiffer it was, which could be used to adjust the bending stiffness of the soft robot arm.

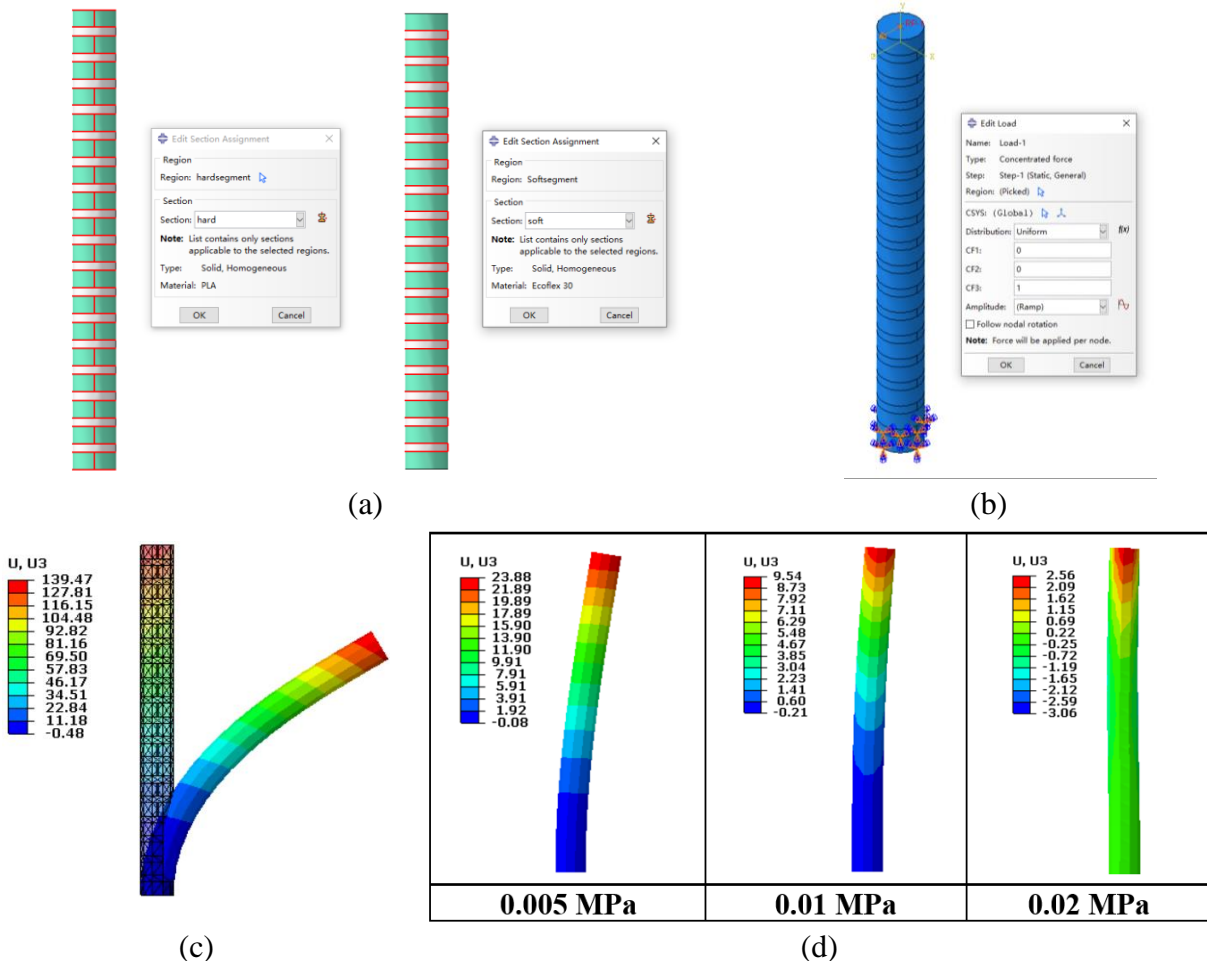


Figure 61. Simulation setup and results of the hybrid rod under different loading conditions. (a) Material property and (b) loading and boundary conditions for the hybrid rod. (c) displacement of the hybrid rod under a 1 N deflection force. (d) Effect of cable-pulling (compression pressure) on variable stiffness of the hybrid rod under a 0.1 N bending force.

Then the hybrid rod structure was integrated into the central hole of the soft arm proposed in Chapter 4. By importing the CAD model of the robot arm with its driving cable and cable fixture

(round cap), the entire simulation model could be established to reveal the effects of hybrid rod on the stiffness adjustment for the robotic arm. To be specific, an additional surface-to-surface contact was applied to the outer surface of the hybrid rod and the inner surface of the central hole. And the surface contact for the cable and cable hole was established in the same way as the previous section (Figure 62a). As for the loading and boundary conditions, both the bottoms of the hybrid rod and the soft arm were constrained in all DOFs, and a pressure load was directly added on the top surface of the rod structure, mimicking cable pulling for the rod structure. A displacement load was applied to the driving cable for the soft arm to induce the bending deformation of the arm as usual (Figure 62b). To accelerate and ease the convergence process for the simulation, multi-steps analysis was performed. In detail, the pressure load was first activated to compress the hybrid rod structure that was embedded in the central hole of the robot arm. As could be seen in Figure 62c, the hybrid rod structure was squeezed under a compression pressure of 0.1 MPa and the higher strains were found from the soft segments in the top positions. After the full compression of the hybrid rod, the cable dragging displacement load was activated, so as to bend the soft arm structure with consideration of the stiffening effect from the hybrid rod. The bending deformation and the strain distribution of the integrated soft arm were illustrated in Figure 62d under different cable pulling displacements. And the continuously compressed hybrid rod could prevent the bending of the soft robotic arm.

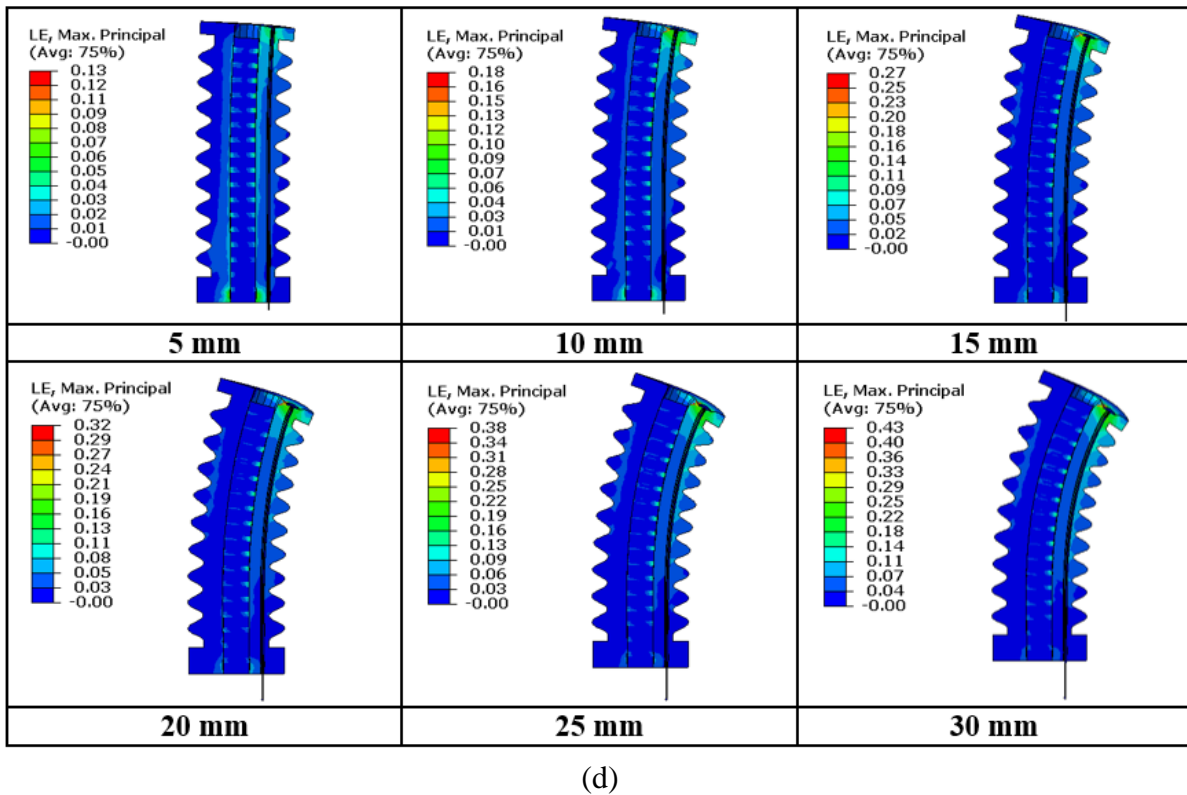
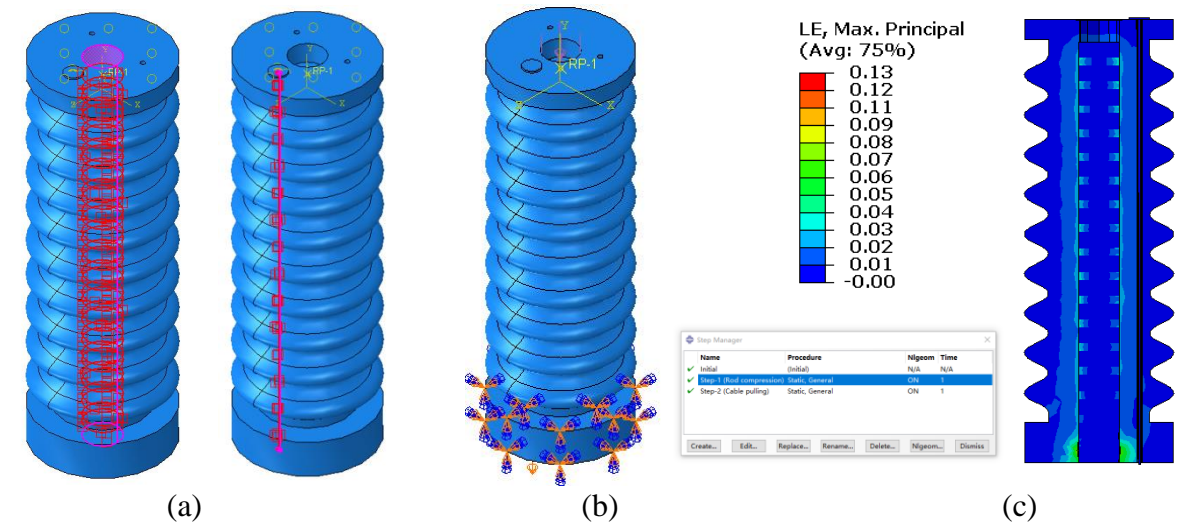


Figure 62. Simulation setup for the soft arm embedded with hybrid rod. (a) Surface contacts and (b) loading and boundary conditions for the entire robot system. (c) Multi-steps analysis for the robot system. (d) Deformation and strain distribution of the hardened arm under different cable pulling displacements.

In addition, another series of simulations was conducted to reveal the effect of compression pressure (i.e., how tightly the hybrid rod was being pulled via cable) on the bending deformations of the soft robotic arm (Figure 63). Without continuously compressing the hybrid rod structure but

just embedding it into the central hole of the robot arm, the maximum displacement of the arm in its bending direction was 67.45 mm under a cable pulling displacement of 30 mm, with a maximum strain of material 0.38. When a 0.05 MPa compression pressure was applied to the hybrid rod core, the arm turned harder to bend, and the maximum bending displacement was reduced to 55.41 mm. The increase of the compression pressure applied to the hybrid rod from 0.05 MPa to 0.1 MPa, reduced the bending displacement of the arm by 15 mm. And when the compression pressure improved to 0.2 MPa, the soft robotic arm could hardly deflect, with a bending displacement of 20.51 mm only. And we could easily tell that the soft arm turned more and more difficult to curve, as the maximum strain increased from 0.38 to 0.47 when the compression pressure moved to 0.2 MPa.

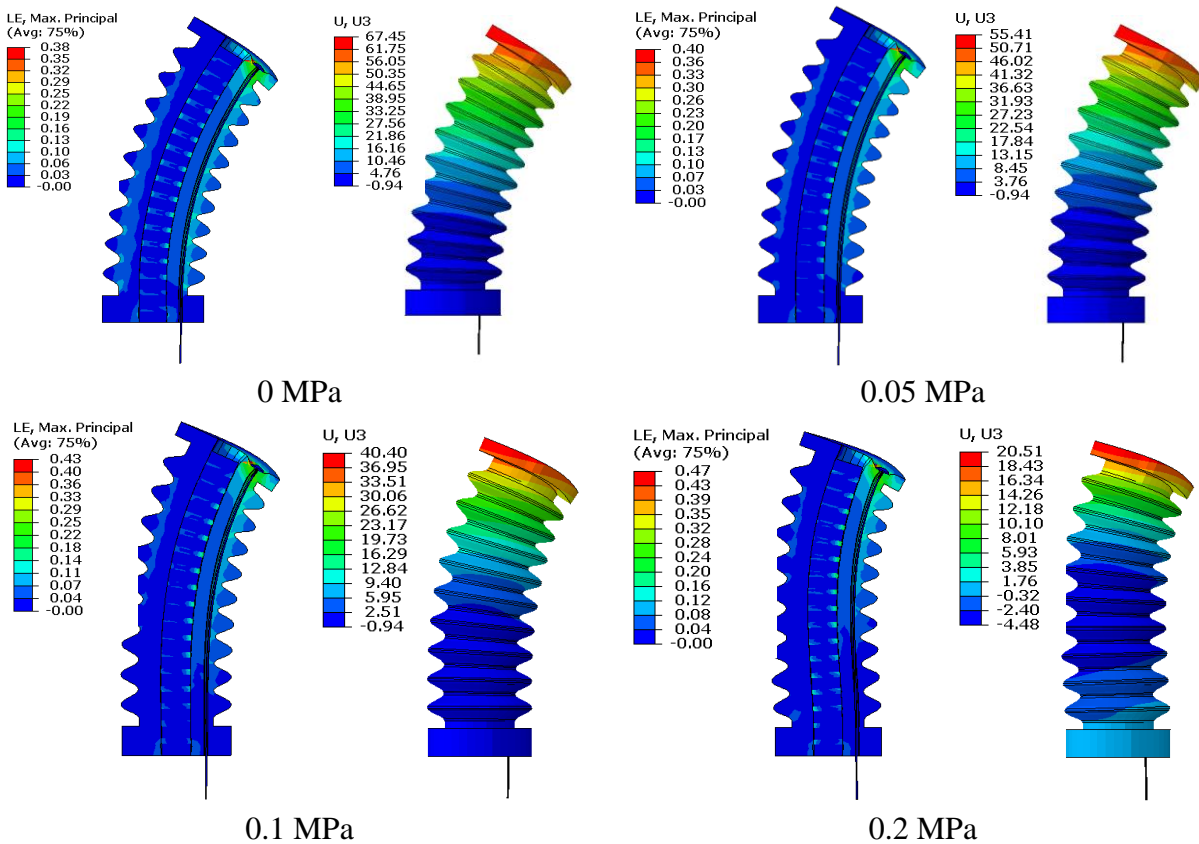


Figure 63. Bending deformation and strain distribution of the integrated soft arm under different compression pressures applied to the hybrid rod structure.

### **5.3 Conclusion and Discussion**

In this chapter, a hybrid rod structure has been designed and embedded into the central hole of the soft robot arm designed in Chapter 4, so as to enable the swift stiffness adjustments. Stiffness modulation for the soft arm via phase-changes of LMPAs suffers from long heating & cooling lag time, as discussed in the previous chapter, which will hinder the applications of soft manipulators. While a hybrid rod design, inspired by mammal spine structure, consists of soft and rigid segments alternatively stacking and bonding with each other, and can realize fast stiffness variation through compression of the soft segments via cable pulling as well, leading to a consistence in the actuation mechanism for the entire soft robotic system. This hybrid structure can easily change the stiffness variation range by applying different cable-pulling forces, which has been validated by various compression pressures on the top surface of the hybrid rod during the FEM analysis. Through the numerical calculation and FEM simulation procedures proposed in this study, people can achieve a desired stiffness adjustment range for the rod structure with arranging various dimensions of the soft and rigid segments, and the hybrid structure can be applied to any soft robot system. Owing to the high accuracy of simulation, the task is only performed numerically, without conducting physical experiment. Anyway, this study has validated the efficient stiffness adjustment approach from a hybrid stacking structure and paved the way to apply such method into different soft robotic applications.

## CHAPTER 6: CONCLUSION AND FUTURE RESEARCH

### 6.1 Conclusion

Throughout this dissertation research, contributions have been made to develop structures for the dexterous soft manipulator including arm and finger/gripper, develop flexible sensing units compatible with soft robot body (pressure and curvature detection), establish reliable human-machine interface for efficient robotic teleoperation, and design stiffness adjustment approaches for the soft robotic arm (navigation and support purposes for the soft manipulation system). Among all the as-mentioned actuation methods for soft robotic application, cable-driven mechanism is selected as the actuation approach for soft robotic constructions. Cable-driven approach exhibits features, like light weight, fast response, and large force exertion. Its output characteristics can be easily adjusted by replacing DC motor of various specifications, and the actuation force via the cable can be delivered along the whole soft body from a (cable) fixing point to minimize the inertia of the robotic body.

To design the soft finger actuator/assembled gripper device, in the initial stage (Chapter 2), an actuator mimicking human finger and capable of bidirectional bending is proposed. By inserting two cables in the robot body (at offset positions), fixing them at the fingertip of the soft robot, and twining both cables to a spindle on a miniature DC motor, the soft finger actuator can bend outward to expand its grasping scope, and bend inward to form a conformal enveloping profile for targeted object. Then, a smart soft actuator with similar structure (triangular notch features) as the previous one is developed in Chapter 3. Its intelligence is enhanced by incorporating soft TENG technology. In detail, two different flexible TENGs are integrated onto the soft finger actuator, including a pair of TENG strips in contact-separation mode that can detect curvature of the finger robot, and tribo-skin patterned with micro-pyramid features that senses contact pressure in a single-electrode mode.

These flexible TENG sensors are self-powered and will not affect the mechanical behaviors of the finger actuator. Experiments have demonstrated that the smart gripper can perceive grasping stages, including approaching, contacting, gripping, and releasing, and predict shapes and relative weights of different objects. And finally in Chapter 4, multi-material and flexible hinge designs are adopted to improve the bidirectional finger actuator, including a stiffer robot framework and porous filling blocks for maintaining bending flexibility of the actuator and encapsulating exposed cable to avoid potential interferences with the environment (e.g., cable entanglements with branches during field harvesting).

On the other hand, a soft bellow-shaped robot arm is developed in Chapter 4 and integrated with the improved multi-material finger actuator/gripper to form an entirely soft manipulator. This soft arm can realize omnidirectional bending via a three-cable distribution inside the robotic body, and such bellow-profile can eliminate the potential buckling during large deformations. In addition, to make the arm robust and stable during operation (e.g., against gravity and external load). LMPA tubes are embedded inside the robotic body to adjust the overall stiffness of the structure via phase changes of the alloys under Joule heating. However, the slow response time during cooling process requires a swifter solution for adjusting the stiffness of the proposed soft arm, hence, a hybrid rod with soft and rigid segments alternatively stacking together (inspired by spine) is designed and put into the central hole of the robot arm (Chapter 5). Its stiffness is changed through compressions of the soft segments via cable actuation, leading to consistency in actuation mechanism for the entire soft robot system.

To enable the remote control of the soft manipulator for a variety of applications. A TENG-based wearable device serving as an HMI is developed in Chapter 4. In the form of the finger patch, the flexible and biocompatible TENG device can detect the motion of human finger. Flexion and

extension of the human finger will generate a voltage signal related to the bending degree of human finger. And threshold control strategy is adopted to screen out intentional finger motions to control the soft manipulator, providing a way to construct a straightforward wireless HMI for soft robotics.

To validate the soft robotic designs, nonlinear FEM is utilized to simulate the deformation and the corresponding strain & stress distributions for the soft bodies with the effects of cable. The setup for simulation has been proved to be an efficient and precise way to predict the behaviors of soft cable-driven robotics. And simulations for TENG devices are also performed to figure out the tendency for voltage generation, although their electrical behaviors are mainly revealed via testing. The dissertation is conducted to pave the way for making a comprehensive soft robotic manipulator featured with dexterous soft robot actuators for navigation, positioning, and grasping, intelligence in perceiving the environment and targeted objects, swift stiffness adjustment function, and remote controls through wearable HMI, contributing to a safer human-machine-environment interactions.

## **6.2 Future Research**

Great effort should be continuously put into the development of flexible sensors compatible with soft cable-driven robotic designs, as their sensing performances is highly related to the quality of operations for soft manipulators. For example, the soft tactile sensors can help soft gripper detect whether the grasping force is appropriate for fragile or rigid objects, and whether the gripper needs to expand its opening so as to fully cover large size subjects. In this dissertation, two typical types of sensors for soft robotics are developed, including a patterned tribo-skin as contact sensor and a pair of TENG strips as curvature sensor embedded in the chamber of soft finger actuator. However, it is observed that the sensing behaviors of tribo-skin is strongly influenced by some uncontrollable factors, such as contact materials, humidity, and temperature of the environment, which will cause difficulties in the calibration of the contact sensor based on triboelectric nanogenerator technology.

Hence, to attain a more reliable sensing performance, other factors should be kept constant during operations. One optimization method for tribo-skin is to make it work in a contact-separation mode, which could get it rid of the influences from materials and environmental factors. Also, the existing structure of tactile/pressure sensor does not consider the function of identifying contacting position. As the contact area of the tribo-skin may vary due to the shape variation of subject, which will also cause uncertainties for calibrations, a more sophisticated configuration and structure for the tactile sensor made of flexible materials should be studied. By incorporating these improvements into the soft pressure/tactile sensor based on TENG technology, the soft gripper is able to be more sensitive during contact process with objects and can be ready for machine learning applications, like object recognition and screening & classifying object. On the other hand, method of realizing the variable stiffness for soft manipulation system will be focused. The proposed stiffness adjustment structure is promising to be used and optimized for various cable-driven robotic applications. However, the actuation of such hybrid structure may cause potential buckling to the entire body due to its slender profile. Shell structure may be considered to encapsulate the hybrid design to enhance its resistance to buckling and instability. Also, different lengths and shapes of the soft segment should be studied in detail, so as to realize anisotropic variable stiffness property for the hybrid structure.

## BIBLIOGRAPHY

1. George Thuruthel, T., et al., *Control strategies for soft robotic manipulators: A survey*. Soft Robotics, 2018. **5**(2): 149-163.
2. Al-Ibadi, A., Nefti-Meziani, S., and Davis, S., *Active soft end effectors for efficient grasping and safe handling*. IEEE Access, 2018. **6**: 23591-23601.
3. Mosadegh, B., et al., *Pneumatic networks for soft robotics that actuate rapidly*. Advanced Functional Materials, 2014. **24**(15): 2163-2170.
4. Shepherd, R.F., et al., *Multigait soft robot*. Proceedings of the National Academy of Sciences, 2011. **108**(51): 20400-20403.
5. Branyan, C., et al., *Soft snake robots: Mechanical design and geometric gait implementation*. In 2017 IEEE International Conference on Robotics and Biomimetics (ROBIO). 2017.
6. Lissmann, H., *Rectilinear locomotion in a snake (Boa occidentalis)*. Journal of Experimental Biology, 1950. **26**(4): 368-379.
7. Marvi, H., et al., *Snakes move their scales to increase friction*. Biotribology, 2016. **5**: 52-60.
8. Hu, D.L., et al., *The mechanics of slithering locomotion*. Proceedings of the National Academy of Sciences, 2009. **106**(25): 10081-10085.
9. Cao, Y., et al., *A novel slithering locomotion mechanism for a snake-like soft robot*. Journal of the Mechanics and Physics of Solids, 2017. **99**: 304-320.
10. Abdel-Aal, H.A. and El Mansori, M., *Tribological analysis of the ventral scale structure in a Python regius in relation to laser textured surfaces*. Surface Topography: Metrology and Properties, 2013. **1**(1): 015001.
11. Marvi, H., Han, Y., and Sitti, M., *Actively controlled fibrillar friction surfaces*. Applied Physics Letters, 2015. **106**(5): 051602.
12. Das, S., et al., *Stick-slip friction of gecko-mimetic flaps on smooth and rough surfaces*. Journal of The Royal Society Interface, 2015. **12**(104): 20141346.
13. Yamaguchi, T., Sawae, Y., and Rubinstein, S.M., *Effects of loading angles on stick-slip dynamics of soft sliders*. Extreme Mechanics Letters, 2016. **9**: 331-335.
14. Rafsanjani, A., et al., *Kirigami skins make a simple soft actuator crawl*. Science Robotics, 2018. **3**(15): eaar7555.
15. Shyu, T.C., et al., *A kirigami approach to engineering elasticity in nanocomposites through patterned defects*. Nature Materials, 2015. **14**(8): 785.

16. Blees, M.K., et al., *Graphene kirigami*. Nature, 2015. **524**(7564): 204.
17. Rafsanjani, A. and Bertoldi, K., *Buckling-induced kirigami*. Physical Review Letters, 2017. **118**(8): 084301.
18. Tang, Y., et al., *Programmable Kiri-Kirigami Metamaterials*. Advanced Materials, 2017. **29**(10): 1604262.
19. Hao, Y., et al., *Universal soft pneumatic robotic gripper with variable effective length*. In 2016 35th Chinese Control Conference (CCC), IEEE, 2016. 6109-6114.
20. Robertson, M.A. and Paik, J., *New soft robots really suck: Vacuum-powered systems empower diverse capabilities*. Science Robotics, 2017. **2**: eaan6357.
21. Ham, K., et al., *Soft gripper using variable stiffness mechanism and its application*. International Journal of Precision Engineering and Manufacturing, 2018. **19**(4): 487-494.
22. Mutlu, R., et al., *3D printed flexure hinges for soft monolithic prosthetic fingers*. Soft Robotics, 2016. **3**(3): 120-133.
23. Ito, K., Homma, Y. and Rossiter, J., *The soft multi-legged robot inspired by octopus: climbing various columnar objects*. Advanced Robotics, 2020. **34**(17): 1096-1109.
24. Bern, J., et al. *Trajectory optimization for cable-driven soft robot locomotion*. Science and Systems, 2019, **1**(3).
25. Minaminosono, A., et al., *A Deformable Motor Driven by Dielectric Elastomer Actuators and Flexible Mechanisms*. Frontiers in Robotics and AI, 2019. **6**(1): 1-12.
26. Gu, G.-Y., et al., *A survey on dielectric elastomer actuators for soft robots*. Bioinspiration & Biomimetics, 2017. **12**(1): 011003.
27. Henke, E.F.M., Wilson, K.E., and Anderson, I.A., *Entirely soft dielectric elastomer robots*. SPIE, 2017. **10163**: 287-297.
28. Li, W.B., et al., *A fast rolling soft robot driven by dielectric elastomer*. IEEE/ASME Transactions on Mechatronics, 2018. **23**(4): 1630-1640.
29. Sastra, J., Chitta, S., and Yim, M., *Dynamic Rolling for a Modular Loop Robot*. The International Journal of Robotics Research, 2009. **28**(6): 758-773.
30. Artusi, M., et al., *Electroactive elastomeric actuators for the implementation of a deformable spherical rover*. IEEE/ASME Transactions on Mechatronics, 2011. **16**(1): 50-57.
31. Firouzeh, A., et al., *An IPMC-made deformable-ring-like robot*. Smart Materials and Structures, 2012. **21**(6): 65011.

32. Li, W.-B., et al., *Multisegment annular dielectric elastomer actuators for soft robots*. Smart Materials and Structures, 2018. **27**(11): 115024.
33. Pelrine, R., et al., *Dielectric elastomer artificial muscle actuators: toward biomimetic motion*. SPIE's 9th Annual International Symposium on Smart Structures and Materials, 2002. **4695**: 126-137.
34. Cao, J., et al., *Development of a soft untethered robot using artificial muscle actuators*. In Electroactive Polymer Actuators and Devices (EAPAD), SPIE, 2017. **10163**: 322-328.
35. Araromi, O.A., et al., *Rollable Multisegment Dielectric Elastomer Minimum Energy Structures for a Deployable Microsatellite Gripper*. IEEE/ASME Transactions on Mechatronics, 2015. **20**(1): 438-446.
36. Nguyen, C.T., et al., *A novel bioinspired hexapod robot developed by soft dielectric elastomer actuators*. In 2017 IEEE/RSJ International Conference on Intelligent Robots and Systems (IROS), 2017. 6233-6238.
37. Choi, H., et al., *Multiple degree-of-freedom digital soft actuator for robotic applications*. In Smart Structures and Materials 2003: Electroactive Polymer Actuators and Devices (EAPAD), 2003. **5051**: 262-271.
38. Choi, H., et al., *Digital polymer motor for robotic applications*. In 2003 IEEE International Conference on Robotics and Automation (Cat. No. 03CH37422), 2003. **2**: 1857-1862.
39. Ahmed, S., et al., *Electric field responsive origami structures using electrostriction-based active materials*. In Behavior and Mechanics of Multifunctional Materials and Composites 2015, SPIE, 2015. **9432**: 29-41.
40. Chen, Q., et al., *Piezoelectric polymers actuators for precise shape control of large scale space antennas*. In Electroactive Polymer Actuators and Devices (EAPAD) 2007, SPIE, 2007. **6524**: 491-501.
41. Wu, Y., et al., *PRE-curved PVDF/PI unimorph structures for biomimic soft crawling actuators*. In 2018 IEEE Micro Electro Mechanical Systems (MEMS), 2018. 581-584.
42. Chu, W.-S., et al., *Review of biomimetic underwater robots using smart actuators*. International Journal of Precision Engineering and Manufacturing, 2012. **13**: 1281-1292.
43. Umedachi, T., Vikas, V., and Trimmer, B.A., *Highly deformable 3-d printed soft robot generating inching and crawling locomotions with variable friction legs*. In 2013 IEEE/RSJ International Conference on Intelligent Robots and Systems, 2013. 4590-4595.
44. Lin, H.-T., Leisk, G.G., and Trimmer, B., *GoQBot: a caterpillar-inspired soft-bodied rolling robot*. Bioinspiration & Biomimetics, 2011. **6**(2): 026007.

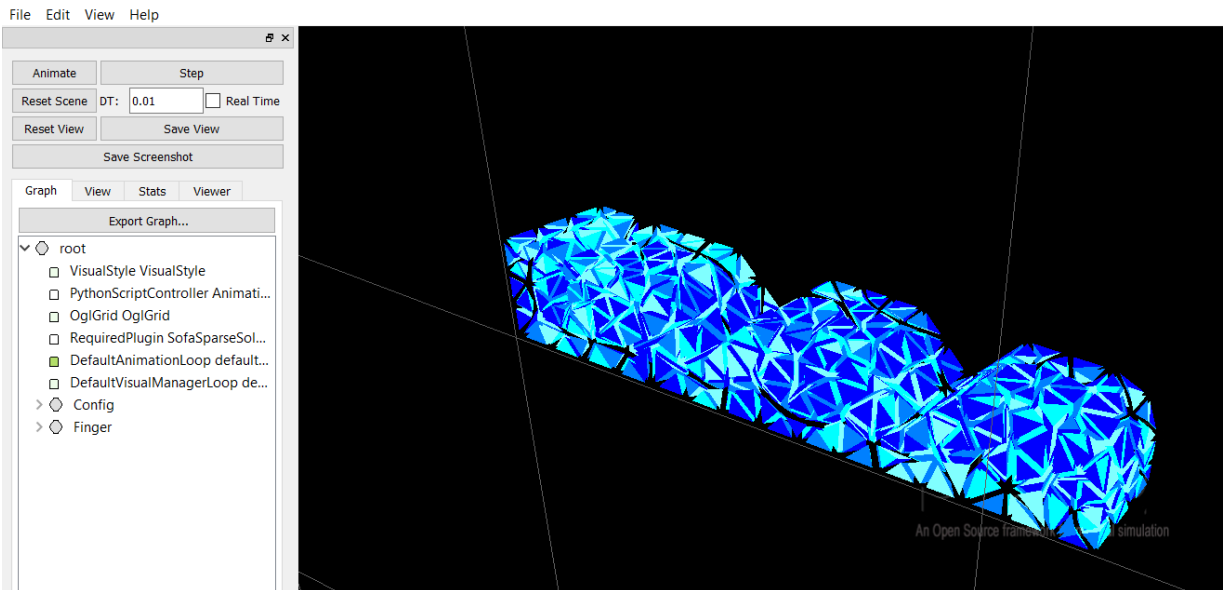
45. Mao, S., et al. *Design and development of starfish-like robot: Soft bionic platform with multi-motion using SMA actuators*. In 2013 IEEE International Conference on Robotics and Biomimetics (ROBIO), 2013.
46. Kim, H.-J., Song, S.-H., and Ahn, S.-H., *A turtle-like swimming robot using a smart soft composite (SSC) structure*. Smart Materials and Structures, 2012. **22**(1): 014007.
47. Koh, J.-S. and Cho, K.-J., *Omega-Shaped Inchworm-Inspired Crawling Robot With Large-Index-and-Pitch (LIP) SMA Spring Actuators*. IEEE/ASME Transactions on Mechatronics, 2013. **18**(2): 419-429.
48. Nelson, B.J., Kaliakatsos, I.K., and Abbott, J.J., *Microrobots for minimally invasive medicine*. Annual Review of Biomedical Engineering, 2010. **12**: 55-85.
49. Sitti, M., et al., *Biomedical applications of untethered mobile milli/microrobots*. Proc IEEE Inst Electr Electron Eng., 2015. **103**(2): 205-224.
50. Lum, G.Z., et al., *Shape-programmable magnetic soft matter*. Proceedings of the National Academy of Sciences, 2016. **113**(41): E6007-E6015.
51. Hines, L., et al., *Soft actuators for small-scale robotics*. Advanced Materials, 2017. **29**(13): 1603483.
52. Hu, W., et al., *Small-scale soft-bodied robot with multimodal locomotion*. Nature, 2018. **554**: 81.
53. Lu, H., et al., *A bioinspired multilegged soft millirobot that functions in both dry and wet conditions*. Nature Communications, 2018. **9**(1): 3944.
54. Timonen, J.V., et al., *A facile template-free approach to magnetodriven, multifunctional artificial cilia*. ACS Applied Materials & Interfaces, 2010. **2**(8): 2226-2230.
55. Erb, R.M., et al., *Actuating soft matter with magnetic torque*. Advanced Functional Materials, 2016. **26**(22): 3859-3880.
56. Lee, H., et al., *Programming magnetic anisotropy in polymeric microactuators*. Nature Materials, 2011. **10**(10): 747.
57. Kim, Y., et al., *Printing ferromagnetic domains for untethered fast-transforming soft materials*. Nature, 2018. **558**(7709): 274-279.
58. Ikeda, T., Mamiya, J.I., and Yu, Y., *Photomechanics of liquid-crystalline elastomers and other polymers*. Angewandte Chemie International Edition, 2007. **46**(4): 506-528.
59. Küpfer, J. and Finkelmann, H., *Nematic liquid single crystal elastomers*. Die Makromolekulare Chemie, Rapid Communications, 1991. **12**(12): 717-726.
60. Yamada, M., et al., *Photomobile polymer materials-various three-dimensional*

- movements*. Journal of Materials Chemistry, 2009. **19**(1): 60-62.
61. Roach, D.J., et al., *Novel ink for ambient condition printing of liquid crystal elastomers for 4D printing*. Smart Materials and Structures, 2018. **27**(12): 125011.
  62. Rogó , M., et al., *Light-Driven Soft Robot Mimics Caterpillar Locomotion in Natural Scale*. Advanced Optical Materials, 2016. **4**(11): 1689-1694.
  63. Wang, C., et al., *Soft Ultrathin Electronics Innervated Adaptive Fully Soft Robots*. Advanced Materials, 2018. **30**(13): 1706695.
  64. Shahinpoor, M. and Kim, K.J., *Ionic polymer-metal composites: I. Fundamentals*. Smart Materials and Structures, 2001. **10**(4): 819.
  65. Carrico, J.D., Kim, K.J., and Leang, K.K., *3D-printed ionic polymer-metal composite soft crawling robot*. In 2017 IEEE International Conference on Robotics and Automation (ICRA), 2017. 4313-4320.
  66. Abbas Kashmery, H., *Polyvinylidene fluoride/sulfonated graphene oxide blend membrane coated with polypyrrole/platinum electrode for ionic polymer metal composite actuator applications*. Scientific Reports, 2019. **9**(1): 1-11.
  67. Suzuki, M., and Kamamichi, N., *Displacement control of an antagonistic-type twisted and coiled polymer actuator*. Smart Materials and Structures, 2018. **27**(3): 035003.
  68. Zhao, J. and Abbas, A., *A low-cost soft coiled sensor for soft robots*. In *Dynamic Systems and Control Conference*, 2016. American Society of Mechanical Engineers.
  69. Pawlowski, B., et al, *Modeling of soft robots actuated by twisted-and-coiled actuators*. IEEE/ASME Transactions on Mechatronics. 2018, **24**(1): 5-15.
  70. Yang, Y., et al., *A Low-cost Inchworm-inspired Soft Robot Driven by Supercoiled Polymer Artificial Muscle*. In 2019 2nd IEEE International Conference on Soft Robotics (RoboSoft), 2019. 161-166.
  71. Wang, H., et al., *A cable-driven soft robot surgical system for cardiothoracic endoscopic surgery: preclinical tests in animals*. Surgical Endoscopy, 2017. **31**(8): 3152-3158.
  72. Lee, J.-Y., et al., *Development of a multi-functional soft robot (SNUMAX) and performance in RoboSoft Grand Challenge*. Frontiers in Robotics and AI, 2016. **3**:63.
  73. Inc., S.R., *Soft Pneumatic Gripper for Industrial Packaging Lines*. <https://www.softroboticsinc.com>.
  74. Hooker, L., (2018, May 25) *The strawberry-picking robots doing a job humans won't*. BBC. <https://www.bbc.com/news/business-43816207>.
  75. Galloway, K.C., et al., *Soft robotic grippers for biological sampling on deep reefs*. Soft

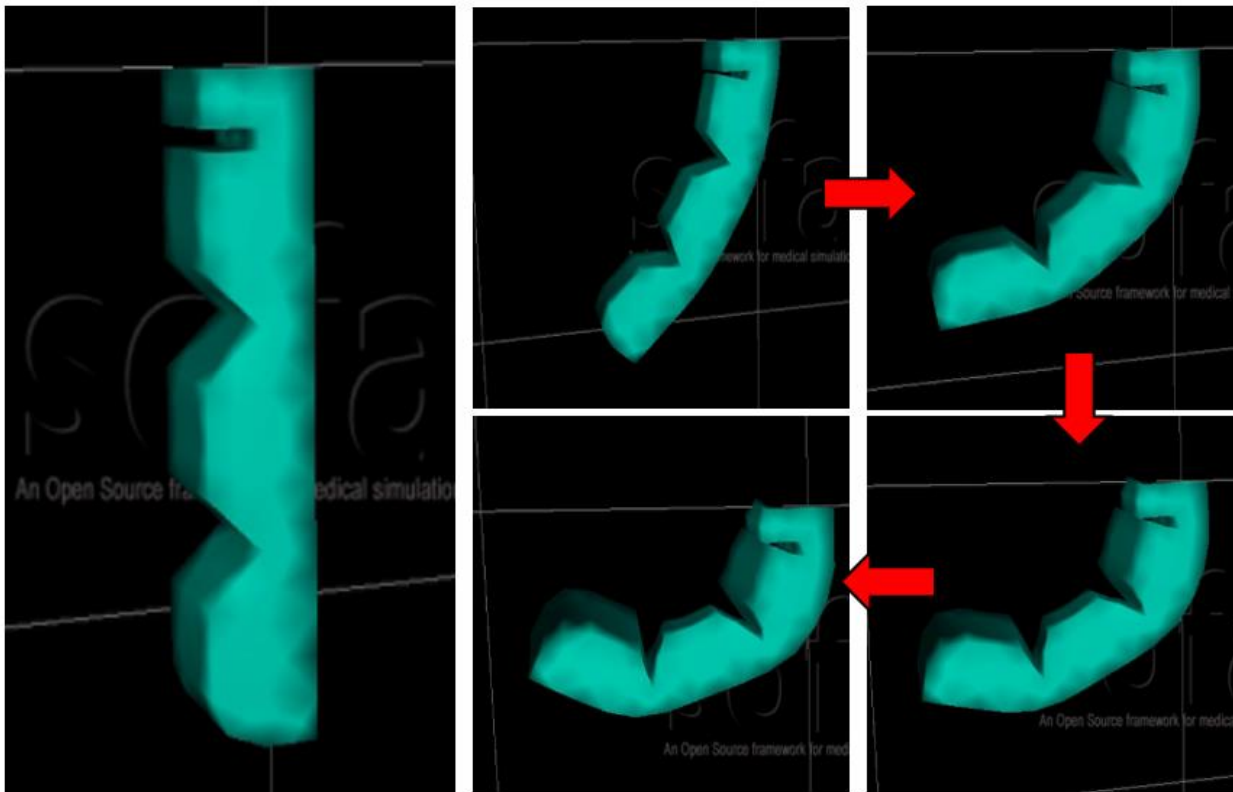
- Robotics, 2016. **3**(1): 23-33.
76. Shtarbanov, A., *FlowIO Development Platform—the Pneumatic “Raspberry Pi” for Soft Robotics*. In Extended Abstracts of the 2021 CHI Conference on Human Factors in Computing Systems, 2021.
  77. Cianchetti, M., et al., *Soft robotics technologies to address shortcomings in today's minimally invasive surgery: the STIFF-FLOP approach*. Soft Robotics, 2014. **1**(2): 122-131.
  78. Pettersson, A., et al., *Design of a magnetorheological robot gripper for handling of delicate food products with varying shapes*. Journal of Food Engineering, 2010. **98**(3): 332-338.
  79. Yang, Y., et al., *Hybrid jamming for bioinspired soft robotic fingers*. Soft Robotics, 2020. **7**(3): 292-308.
  80. Mao, Y., et al., *3D printed reversible shape changing components with stimuli responsive materials*. Scientific Reports, 2016. **6**(1): 24761.
  81. Shintake, J., et al., *Variable stiffness actuator for soft robotics using dielectric elastomer and low-melting-point alloy*. In 2015 IEEE/RSJ International Conference on Intelligent Robots and Systems (IROS), 2015. 1097-1102.
  82. Manti, M., et al., *Stiffening in soft robotics: A review of the state of the art*. IEEE Robotics & Automation Magazine, 2016. **23**(3): 93-106.
  83. Al-Rubaiai, M., et al., *Soft Actuators with Stiffness and Shape Modulation Using 3D-printed Conductive Polylactic Acid Material*. Soft Robotics, 2019. **6**(3): 318-332.
  84. Yufei, H., et al., *A variable stiffness soft robotic gripper with low-melting-point alloy*. In 2017 36th Chinese Control Conference (CCC), IEEE, 2017. 6781-6786.
  85. Zhang, Y.F., et al., *Fast-Response, Stiffness-Tunable Soft Actuator by Hybrid Multimaterial 3D Printing*. Advanced Functional Materials, 2019. **29**(15): 1806698.
  86. Fitzgerald, S.G., Delaney, G.W., and Howard, D., *A Review of Jamming Actuation in Soft Robotics*. In Actuators, 2020. **9**(4): 104.
  87. Jiang, P., et al., *A variable stiffness gripper based on differential drive particle jamming*. Bioinspiration & Biomimetics, 2019. **14**(3): 036009.
  88. Xie, M., et al., *Flexible self-powered multifunctional sensor for stiffness-tunable soft robotic gripper by multimaterial 3D printing*. Nano Energy, 2021. **79**: 105438.
  89. Jadhav, S., et al., *Variable Stiffness Devices Using Fiber Jamming for Application in Soft Robotics and Wearable Haptics*. Soft Robotics, 2022. **9**(1): 173-86.

90. Zhou, X. and Lee, P.S., *Three-dimensional printing of tactile sensors for soft robotics*. MRS Bulletin, 2021. **46**(4): 330-336.
91. Wang, Z.L., *Triboelectric nanogenerators as new energy technology for self-powered systems and as active mechanical and chemical sensors*. ACS Nano, 2013. **7**(11): 9533-9557.
92. Luo, J. and Wang, Z.L., *Recent progress of triboelectric nanogenerators: From fundamental theory to practical applications*. EcoMat, 2020. **2**(4): e12059.
93. Chen, J., et al., *Soft robots with self-powered configurational sensing*. Nano Energy, 2020. **77**: 105171.
94. Zhu, M., et al., *A soft robotic finger with self-powered triboelectric curvature sensor based on multi-material 3D printing*. Nano Energy, 2020. **73**: 104772.
95. Chen, J., et al., *A Triboelectric Nanogenerator as a Self-Powered Sensor for a Soft–Rigid Hybrid Actuator*. Advanced Materials Technologies, 2019. **4**(9): 1900337.
96. Sun, Z., Zhu, M., and Lee, C., *Progress in the Triboelectric Human–Machine Interfaces (HMIs)-Moving from Smart Gloves to AI/Haptic Enabled HMI in the 5G/IoT Era*. Nanoenergy Advances, 2021. **1**(1): 81-120.
97. He, Q., et al., *An all-textile triboelectric sensor for wearable teleoperated human–machine interaction*. Journal of Materials Chemistry A, 2019. **7**(47): 26804-26811.
98. Coevoet, E., et al., *Software toolkit for modeling, simulation, and control of soft robots*. Advanced Robotics, 2017. **31**(22): 1208-1224.
99. Fan, F.-R., et al., *Transparent triboelectric nanogenerators and self-powered pressure sensors based on micropatterned plastic films*. Nano Letters, 2012. **12**(6): 3109-3114.
100. Agarwal, G., et al., *Stretchable materials for robust soft actuators towards assistive wearable devices*. Scientific Reports, 2016. **6**: 34224.
101. Zhang, R. and Olin, H., *Material choices for triboelectric nanogenerators: a critical review*. EcoMat, 2020. **2**(4): e12062.
102. Nuthi, S.G., *Computational modeling and experimental characterization of pneumatically driven actuators for the development of a soft robotic arm*. 2018, Arizona State University.
103. Wang, S., et al., *Stretchable and Wearable Triboelectric Nanogenerator Based on Kinesio Tape for Self-Powered Human Motion Sensing*. Nanomaterials, 2018. **8**(9): 657.

## APPENDIX A: SIMULATION OF SOFT FINGER ACTUATOR WITH SOFA



(a)



(b)

Figure 64. Simulation of the soft finger actuator via SOFA Framework. (a) Meshed finger body utilizing Gmsh. (b) Deformation of the finger actuator after setting collision property for contact surfaces and defining cable positions.

The simulation program in SOFA environment was coded as follows:

```
# -*- coding: utf-8 -*-
import Sofa
from stlib.visuals import ShowGrid
from stlib.physics.deformable import ElasticMaterialObject
from stlib.physics.constraints import FixedBox
from stlib.scene import Node
from softrobots.actuators import PullingCable
from stlib.physics.collision import CollisionMesh
from splib.loaders import loadPointListFromFile

class FingerController(Sofa.PythonScriptController):
    def __init__(self, node, cable ):
        self.cableconstraintvalue = cable.getObject("CableConstraint").findData('value')
        self.name = "FingerController"

    def onKeyPressed(self,c):
        if (c == "+"):
            self.cableconstraintvalue.value = self.cableconstraintvalue.value[0][0] + 1.

        elif (c == "-"):
            displacement = self.cableconstraintvalue.value[0][0] - 1.
            if(displacement < 0):
                displacement = 0
            self.cableconstraintvalue.value = displacement

def Finger(parentNode=None, name="Finger",
           rotation=[0.0, 0.0, 0.0], translation=[0.0, 0.0, 0.0],
           fixingBox=[-5.0,0.0,0.0,10.0,15.0,20.0], pullPointLocation=[0.0,0.0,0.0]):

    finger = Node(parentNode, name)
    eobject = ElasticMaterialObject(finger,
                                   volumeMeshFileName="data/mesh/finger.vtk",
                                   poissonRatio=0.3,
                                   youngModulus=20000,
                                   totalMass=0.5,
                                   surfaceColor=[0.0, 0.8, 0.7],
                                   surfaceMeshFileName="data/mesh/finger.stl",
                                   rotation=rotation,
                                   translation=translation)

    FixedBox(eobject.node, atPositions=fixingBox, doVisualization=True)
    cable=PullingCable(eobject.node,
                       "PullingCable",
                       pullPointLocation=pullPointLocation,
```

```

        rotation=rotation,
        translation=translation,
        cableGeometry=loadPointListFromFile("data/mesh/cable.json"));

FingerController(eobject.node, cable)

CollisionMesh(eobject.node, name="CollisionMesh",
    surfaceMeshFileName="data/mesh/finger.stl",
    rotation=rotation, translation=translation,
    collisionGroup=[1, 2])

CollisionMesh(eobject.node, name="CollisionMeshAuto1",
    surfaceMeshFileName="data/mesh/fingerCollision_part1.stl",
    rotation=rotation, translation=translation,
    collisionGroup=[1])

CollisionMesh(eobject.node, name="CollisionMeshAuto2",
    surfaceMeshFileName="data/mesh/fingerCollision_part2.stl",
    rotation=rotation, translation=translation,
    collisionGroup=[2])

return finger

def createScene(rootNode):
    ShowGrid(rootNode)
    from stlib.scene import MainHeader, ContactHeader
    MainHeader(rootNode, gravity=[0.0, -981.0, 0.0], plugins=["SoftRobots"])
    ContactHeader(rootNode, alarmDistance=4, contactDistance=3, frictionCoef=0.08)

    Finger(rootNode, translation=[0.0,0.0,0.0])
    return rootNode

```

## APPENDIX B: PROGRAM FOR SOFT MANIPULATOR TELEOPERATION

```
#include <RF24Network.h>
#include <RF24.h>
#include <SPI.h>

#define pot1 A0
#define pot2 A1
#define pot3 A2
#define pot4 A3
#define pot5 A4

const int threshold = 1000;
int potValue1 = 0;
int potValue2 = 0;
int potValue3 = 0;
int potValue4 = 0;
int potValue5 = 0;
const char var1[32] = "FTENG1";
const char var2[32] = "FTENG2";
const char var3[32] = "FTENG3";
const char var4[32] = "FTENG4";
const char var5[32] = "FTENG5";

RF24 radio(10, 9); // for RF-Nano
RF24Network network(radio); // Include the radio in the network
const uint16_t this_node = 00; // Address of this node in Octal format ( 04,031, etc)
const uint16_t node01 = 011; // Address of the other node in Octal format
const uint16_t node02 = 021;
const uint16_t node03 = 031;

void setup()
{
  Serial.begin(9600);
  SPI.begin();
  radio.begin();
  network.begin(90, this_node); //(channel, node address)
  radio.setDataRate(RF24_2MBPS);
  radio.setPALevel(RF24_PA_MAX);
}

void loop()
{
  network.update();

  int potValue1= analogRead(pot1);
```

```

int potValue2= analogRead(pot2);
int potValue3= analogRead(pot3);
int potValue4= analogRead(pot4);
int potValue5= analogRead(pot5);

if (potValue1>threshold)
{
  RF24NetworkHeader header1(node01); // (Address where the data is going)
  bool ok1 = network.write(header1, &var1, sizeof(var1)); // Send the data
  delay(50);
}

if (potValue2>threshold)
{
  RF24NetworkHeader header2(node01); // (Address where the data is going)
  bool ok2 = network.write(header2, &var2, sizeof(var2)); // Send the data
  delay(50);
}

if (potValue3>threshold)
{
  RF24NetworkHeader header3(node02); // (Address where the data is going)
  bool ok3 = network.write(header3, &var3, sizeof(var3)); // Send the data
  delay(50);
}

if (potValue4>threshold)
{
  RF24NetworkHeader header4(node02); // (Address where the data is going)
  bool ok4 = network.write(header4, &var4, sizeof(var4)); // Send the data
  delay(50);
}

if (potValue5>threshold)
{
  RF24NetworkHeader header5(node03); // (Address where the data is going)
  bool ok5 = network.write(header5, &var5, sizeof(var5)); // Send the data
  delay(50);
}
}

#include <RF24Network.h>
#include <RF24.h>
#include <SPI.h>

RF24 radio(9, 10); // for UNO

```

```
RF24Network network(radio); // Include the radio in the network
const uint16_t this_node = 011; // Address of our node in Octal format ( 04,031, etc)
```

```
int input1 = 2;
int input2 = 4;
int input3 = 7;
int input4 = 8;
```

```
const char var1[32] = "FTENG1";
const char var2[32] = "BTENG1";
const char var3[32] = "FTENG2";
const char var4[32] = "BTENG2";
```

```
void setup()
{
  SPI.begin();
  radio.begin();
  network.begin(90, this_node); //(channel, node address)
  radio.setDataRate(RF24_2MBPS);
  radio.setPALevel(RF24_PA_MAX);
  pinMode(input1,OUTPUT);
  pinMode(input2,OUTPUT);
  pinMode(input3,OUTPUT);
  pinMode(input4,OUTPUT);
  Serial.begin(9600);
}
```

```
void loop()
{
  network.update();
  while ( network.available() )
  {
    RF24NetworkHeader header;
    char input[32] = "";
    network.read(header, &input, sizeof(input)); // Read the incoming data
```

```
if((strcmp(input,var1) == 0))
{
  digitalWrite(input1,HIGH);
  digitalWrite(input2,LOW);
  delay(50);
  digitalWrite(input1,LOW);
  digitalWrite(input2,LOW);
}
```

```
if((strcmp(input,var2) == 0))
```

```
{  
digitalWrite(input1,LOW);  
digitalWrite(input2,HIGH);  
delay(50);  
digitalWrite(input1,LOW);  
digitalWrite(input2,LOW);  
}
```

```
if((strcmp(input,var3) == 0))  
{  
digitalWrite(input3,HIGH);  
digitalWrite(input4,LOW);  
delay(50);  
digitalWrite(input3,LOW);  
digitalWrite(input4,LOW);  
}
```

```
if((strcmp(input,var4) == 0))  
{  
digitalWrite(input3,LOW);  
digitalWrite(input4,HIGH);  
delay(50);  
digitalWrite(input3,LOW);  
digitalWrite(input4,LOW);  
}
```